Radio Hybrid Reconstruction and Analysis of Inclined Air Showers with AERA of the Pierre Auger Observatory - Measuring the Hadronic Shower Development and Cosmic Ray Mass Composition

Dissertation
zur Erlangung des akademischen Grades eines
Doktors der Naturwissenschaften
der
Fakultät Mathematik und Naturwissenschaften
Fachbereich Physik
der Bergischen Universität Wuppertal

vorgelgt von
Marvin Gottowik
12.04.2021

BERGISCHE
UNIVERSITÄT
WUPPERTAL

The PhD thesis can be quoted as follows:

urn:nbn:de:hbz:468-20210825-115231-6
[http://nbn-resolving.de/urn/resolver.pl?urn=urn%3Anbn%3Ade%3Ahbz%3A468-20210825-115231-6

DOI: 10.25926/21hw-wq22
[https://doi.org/10.25926/21hw-wq22]

Kurzbeschreibung

Das Pierre-Auger-Observatorium ist derzeit der weltweit größte Detektor für kosmische Strahlung bei höchsten Energien. Mit dem Auger Engineering Radio Array (AERA) wird die von ausgedehnten Luftschauern emittierte Radioemission detektiert, wodurch Eigenschaften der Primärteilchen rekonstruiert werden können. Zwei neue Eigenschaften der Radioemission von geneigten Luftschauern werden mit Monte Carlo (MC) Simulationen analysiert. Dabei wird eine Verschiebung des Schwerpunkts der Radioemission um bis zu 1,5 km relativ zum MC-Auftreffpunkt festgestellt, welche auf die Brechung der Radiowellen in der Atmosphäre zurückzuführen ist. Die Form der Radiowellenfront wird am besten durch ein sphärisches Modell beschrieben, da die Quelle der Radioemission bis zu 150 km vom Detektor am Boden entfernt ist. Das sphärische Modell verbessert die Richtungsrekonstruktion und reduziert den Median des Öffnungswinkels mit der MC-Achse für AERA-Simulationen von 0,54° mit dem zuvor verwendeten planaren Modell auf 0,27°. Die verbesserte Richtungsrekonstruktion wird durch eine Teilmenge der gemessenen AERA-Daten bestätigt, der Median des Öffnungswinkels mit der Rekonstruktion des Oberflächendetektors (SD) verbessert sich von 0,84° auf 0,61°.

Mit dem vollständigen Datensatz von 6 Jahren wurden mehr als 2000 geneigte Luftschauer mit Zenitwinkeln zwischen 60° und 80° rekonstruiert. Der Fußabdruck der Radioemission nimmt mit dem Zenithwinkel zu, am Boden kann die Radioemission auf mehr als 100 km^2 nachgewiesen werden. Daher kann die Radioemission mit einem Radioarray mit einem Detektorabstand von 1,5 km, identisch mit dem Abstand der SD-Stationen zueinander, nachgewiesen werden. Dies wird durch die Auswahl von AERA-Antennen auf einem 1,5 km-Raster bei der Rekonstruktion demonstriert. 157 Ereignisse wurden mit dem ausgedünnten AERA rekonstruiert und die Rekonstruktion bestätigt die Leistungsfähigkeit der verwendeten Methoden.

Eine hybride Analyse der Messungen mit AERA und SD ermöglicht die Bestimmung des Myonendefizits in Simulationen und der Masse des Primärteilchens. Die Radioemission ist sensitiv für die Energie der elektromagnetischen Komponente des Luftschauers und daher unabhängig vom SD-Schätzer der Myonenzahl, R_μ. Ein Vergleich von 31 qualitativ hochwertigen Ereignissen mit der MC-Vorhersage zeigt ein Defizit an Myonen in den Simulationen. Für eine realistische chemische Zusammensetzung der kosmischen Strahlung, die mit der durchschnittlichen logarithmischen Atommassenzahl übereinstimmt, wie sie mit dem Fluoreszenzdetektor gemessen wurde, muss R_μ in MC um 25 % erhöht werden. Die Masse des Primärteilchens kann durch Kombination der korrigierten Strahlungsenergie, S_rad, und R_μ bestimmt werden. Vier ausgewählte Ereignisse mit einer Primärenergie über 10 EeV werden mehrfach mit CoREAS simuliert, wobei Protonen und Eisenkerne als Primärteilchen verwendet werden. Die Verteilung von $R_\mu/\sqrt{S_\text{rad}}$ unterscheidet sich für beide Primärteilchen und der gemessene Luftschauer wird jeweils zwischen den Vorhersagen für Protonen und Eisen rekonstruiert.

Diese Ergebnisse ebnen den Weg für den AugerPrime-Radiodetektor, bei dem jede SD-Station mit einer zusätzlichen Radioantenne ausgestattet wird. Dadurch wird die instrumentierte Fläche von 17 km^2 auf 3000 km^2 vergrößert, was eine genaue Bestimmung des Myonendefizits und der Massenzusammensetzung der kosmischen Strahlung bei den höchsten Energien mit großer Statistik ermöglichen wird.

Abstract

The Pierre Auger Observatory is currently the world's largest detector for cosmic rays at the highest energies. With the Auger Engineering Radio Array (AERA) the emitted radio signal of extensive air showers is detected, which allows reconstructing properties of the primary cosmic rays. Two new features of the radio emission of inclined air showers are analyzed with Monte Carlo (MC) simulations. First, a displacement up to 1.5 km of the radio core with respect to the MC impact point due to refraction of the radio waves in the atmosphere is found. Second, the shape of the radio wavefront is found to be described best by a spherical model as the source of the radio emission is up to 150 km away from the detector on ground. The spherical model improves the directional reconstruction and reduces the median opening angle with the MC axis for AERA simulations from $0.54°$ with the previously used planar model to $0.27°$. The improved directional reconstruction is confirmed by a subset of measured AERA data where the median opening angle with the Surface Detector (SD) reconstruction is reduced from $0.84°$ to $0.61°$.

With the full data sample of 6 years more than 2000 inclined air showers with zenith angles between $60°$ and $80°$ have been reconstructed. It is shown that the size of the radio footprint in the shower plane increases with the zenith angle. The footprint on ground can exceed more than $100\,\mathrm{km}^2$ and therefore allows detecting the radio emission with a sparse radio array with a detector spacing of 1.5 km, similar to the spacing of the SD. This is demonstrated by selecting AERA antennas on an approximate 1.5 km grid in the reconstruction. 157 events are reconstructed with sparse AERA and the reconstruction confirms the capability of the used methods.

A hybrid analysis of the measurements with AERA and the SD allows determining the muon deficit in simulations and the mass of the primary particle. The radio emission is sensitive to the energy of the electromagnetic component and is therefore independent of the muon number estimator, R_μ. A comparison of 31 high-quality events to MC prediction reveals a deficit of muons in simulations. For a realistic mixed composition that matches the average logarithmic atomic mass number as measured with the Fluorescence Detector the R_μ in MC has to be increased by 25 %. The mass of the cosmic ray can be estimated by combining the corrected radiation energy, S_rad, and R_μ. Four selected events above 10 EeV primary energy are simulated several times with CoREAS using protons and iron as primary particles. The distribution of $R_\mu/\sqrt{S_\mathrm{rad}}$ shows a separation of both primaries and the data events are reconstructed in between the prediction for protons and iron.

These results pave the way for the AugerPrime Radio Detector, where every SD station will be equipped with an additional radio antenna. This increases the instrumented area from $17\,\mathrm{km}^2$ to $3000\,\mathrm{km}^2$ which will allow for a precise determination of the muon deficit and the mass composition of cosmic rays at the highest energies with great statistics.

Contents

1 | Introduction

Cosmic rays have been discovered in 1912 by Victor Hess [1]. He had measured an increase of ionizing radiation with altitude and concluded that the Earth is bombarded by a constant flux of extraterrestrial radiation. Later measurements of Jacob Clay found evidence that a large fraction of the cosmic rays consist of charged particles [2]. Nowadays, it is known that these particles originate from the sun, from galactic sources outside of our solar system, and from unknown sources in distant galaxies. A single particle can have energies of more than $10^{20}\,\mathrm{eV}$ ($\approx 16\,\mathrm{J}$) which is seven orders of magnitude larger than the achievable energy in the largest particle accelerator on Earth, the Large Hadron Collider at CERN. Even though cosmic rays have been studied for more than a century, their sources, acceleration process, and exact mass composition are still largely unknown.

Cosmic rays with energies above $10^{15}\,\mathrm{eV}$ are detected via a cascade of secondary particles, the extensive air shower, that is induced in the Earth's atmosphere. At energies above $10^{18}\,\mathrm{eV}$, the flux is only in the order of one particle per square kilometer and year so that huge detection areas are needed to gather significant statistics. The world's largest detector, the Pierre Auger Observatory located in Argentina, covers an area of $3000\,\mathrm{km}^2$. It comprises various complementary detector systems such as a Surface Detector (SD), a Fluorescence Detector (FD), and the Auger Engineering Radio Array (AERA). The observatory is currently being upgraded to improve its mass sensitivity with the SD. With AugerPrime every Surface Detector station will be equipped with two new detector systems: a scintillator and a radio antenna.

This thesis is focused on the reconstruction of so-called inclined air showers with zenith angles above 60°. The radio emission of inclined air showers exhibits several interesting new features, two of which are analyzed in this thesis. A displacement of the radio emission footprint with respect to the Monte Carlo impact point is found in simulations with a realistic refractive index profile of the atmosphere. The displacement is explained by refraction of the radio waves in the atmosphere as described by Snell's law. For this study, a new method to reconstruct the radio core is developed that does not rely on a detailed understanding of the full lateral distribution of the radio emission but only utilizes the presence of the Cherenkov-like compression of the radio signal on a ring around the shower axis.

It has been shown that the wavefront of the radio emission has in general a hyperbolic shape. For inclined air showers, where the emission region is far away from the observer, the wavefront can be described with a spherical model. A new reconstruction module is developed that fits the measured signal arrival time for different antenna locations based on the prediction of a spherical wavefront. This improves the directional reconstruction and is now part of the standard radio reconstruction of inclined air showers in the analysis framework of the Pierre Auger Observatory, $\overline{\text{Off}}\underline{\text{line}}$.

More than 2000 events were reconstructed in 6 years of recorded AERA data. The long-standing prediction that the size of the radio footprint increases with zenith angle is confirmed by measured events. These large footprints can illuminate areas of several square kilometers on ground and therefore allow for a detection with sparse radio-antenna arrays with grid sizes of a kilometer or more. This is demonstrated by thinning out AERA to an approximate 1.5 km grid as used for the AugerPrime Radio Detector.

A hybrid reconstruction of particles and radio emission allows determining a muon deficit in data compared to predictions of all current-generation hadronic interaction models. Furthermore, the mass composition of inclined air showers can be estimated. Both analyses are important goals for the AugerPrime Radio Detector and their feasibility is demonstrated using measured AERA data. Due to the small size of AERA of only 17 km^2 the number of events at energies above 4 EeV, which is required for an accurate event reconstruction by the Surface Detector, is low. Nevertheless, the muon deficit is determined precisely and the results are in agreement with two independent Auger analyses. The composition analysis suffers from low statistics, however, with four measured high-quality events a proof-of-principle is given. These prototype analyses are paving the way for the AugerPrime Radio Detector which will detect thousands of such high-energy events during its envisaged lifetime.

The work is complemented by an extension of the standard event selection tool of Auger for radio. Effort is invested especially in the identification of thunderstorm periods as they deteriorate the radio reconstruction. The best out of three methods that have been used in the past is selected and a tool is developed that extracts the needed information from a database and marks the identified thunderstorm events. Another key ingredient is the unambiguous definition of events that have their shower core confined inside the area enclosing all radio signal stations or inside of the instrumented area of AERA. The event selection is completed by a variety of cuts based on the shower direction and reconstructed quantities.

This thesis is structured as follows: An introduction on cosmic rays and extensive air showers as well as their radio emission is given in chapter 2. The different instruments of the Pierre Auger Observatory are summarized in chapter 3. A description of the reconstruction of air showers from AERA data and the used reconstruction software is given in chapter 4. Further information on the extension of the event selection tool is given as well. Chapter 5 summarizes the special features in the radio emission of inclined air showers and shows their potential for further analyses such as the detection of neutrino-induced air showers. The results from a general analysis of inclined air showers with AERA and the prospects of a sparse radio grid are presented in chapter 6. With these reconstructed AERA events, the muon deficit in simulations and the composition of inclined air showers is analyzed in chapter 7. Finally, chapter 8 summarizes this thesis and presents its conclusions.

2 Cosmic Rays and Extensive Air Showers

Cosmic rays are high-energy particles that travel through space and some of them eventually reach the Earth. The energy of a single cosmic ray reaches energies of 10^{20} eV and beyond. With increasing energy the cosmic-ray flux drops rapidly, approximately by a factor of 1000 per decade in energy. At the highest energies of 10^{20} eV less than one cosmic ray per square kilometer and century hit the Earth.

Because of the large range in energy and flux different techniques are used to measure cosmic rays. For energies up to $\sim 10^{15}$ eV direct measurements with balloon experiments or spaceborne detectors are feasible. However, at higher energies the flux is too low to gather sufficient statistics with direct measurements. Therefore, indirect measurements are used. When a highly energetic cosmic ray hits the Earth's atmosphere a so-called *extensive air shower* (EAS), a shower of secondary particles, is produced. This air shower can be detected on ground and properties of the primary cosmic ray particle can be reconstructed with ground-based experiments.

Even though cosmic rays have been studied for more than 100 years by now, fundamental questions about their origin and their acceleration mechanism remain unanswered. In this chapter a summary of measurable quantities such as energy spectrum and mass composition of cosmic rays is given. Furthermore, extensive air showers, their radio emission, and two different simulation codes are described.

2.1 Extensive air showers

When an *ultra-high-energy cosmic ray* (UHECR) reaches the Earth it will interact with an atomic nucleus in the atmosphere. Highly energetic secondary particles are produced in this first interaction that themselves interact with further nuclei or decay and produce even more particles. This process continues until the particles' energies drop below certain threshold values or the particles reach the ground. That way a cascade of billions of secondary particles, an extensive air shower, develops along the direction of the incoming primary particle. In the beginning new particles will be created in every interaction and the total number of secondary particles will increase until it reaches a maximum value at some atmospheric depth called X_{max}. After that, the energies of the secondary particles are too low to produce new particles and the cascade stops. A schematic view of an EAS is shown in Fig. 2.1.

The particles in an air shower can be grouped into the electromagnetic ($e^{\pm}$, γ), muonic ($\mu^{\pm}$), and hadronic ($\pi^{\pm}$, π^{0}, $K^{\pm}$ etc.) components. The longitudinal profiles of these components are also shown in Fig. 2.1. Most interesting for this thesis are

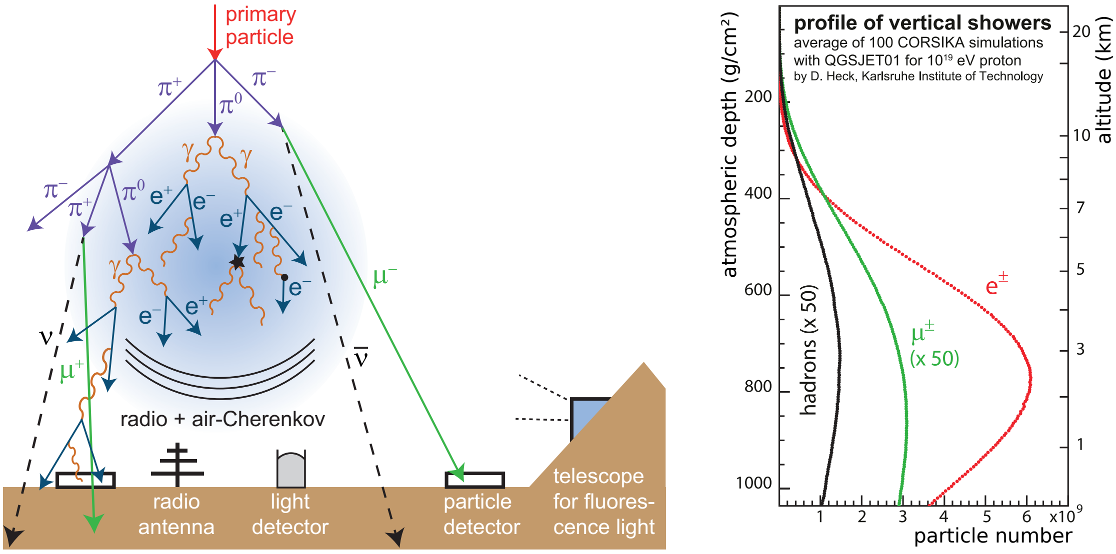

Figure 2.1: Simplified sketch of an air shower and different detection techniques (left) and typical longitudinal shower profiles for different particle types (right). In real air showers more particle types are present, but especially for the radio detection electrons and positrons are the most important ones. Figure adopted from [3].

the electromagnetic and muonic components. For inclined air showers only muons reach the ground, whereas the electromagnetic and hadronic components are absorbed in the atmosphere. The radio emission of an EAS is almost solely produced by the electromagnetic component during its propagation through the atmosphere and is also detectable on ground.

Qualitatively, the development of an air shower can be described by modeling the electromagnetic component with the *Heitler-model* [4] and the hadronic component using the *Heitler-Matthews model* [5]. The muonic component can then be derived from the number of charged pions. However, these models do not describe all details of the particle interactions and only the average development of an air shower is described correctly. In nature, the development of air showers induced by a given primary particle can vary significantly due to stochastic variations in the interactions. Full Monte Carlo (MC) simulations of EAS are performed to describe these variations as well.

Air showers can be measured with different detection techniques, also shown in Fig. 2.1. Well-established methods are the detection of secondary particles on ground with particle detectors and observation of the fluorescence or Cherenkov light produced by the air shower particles' interactions with atmospheric molecules with large-area imaging telescopes. A rather new method is the detection of the broadband megahertz radio emission predicted in [6] which has become an active field of research in recent years. By combining different detection techniques complementary information about the air shower is gained. This can reduce the impact of systematic uncertainties of the individual techniques and allows reconstructing quantities in a combined analysis that would not be available using only one detection technique. This is known as *hybrid observation*.

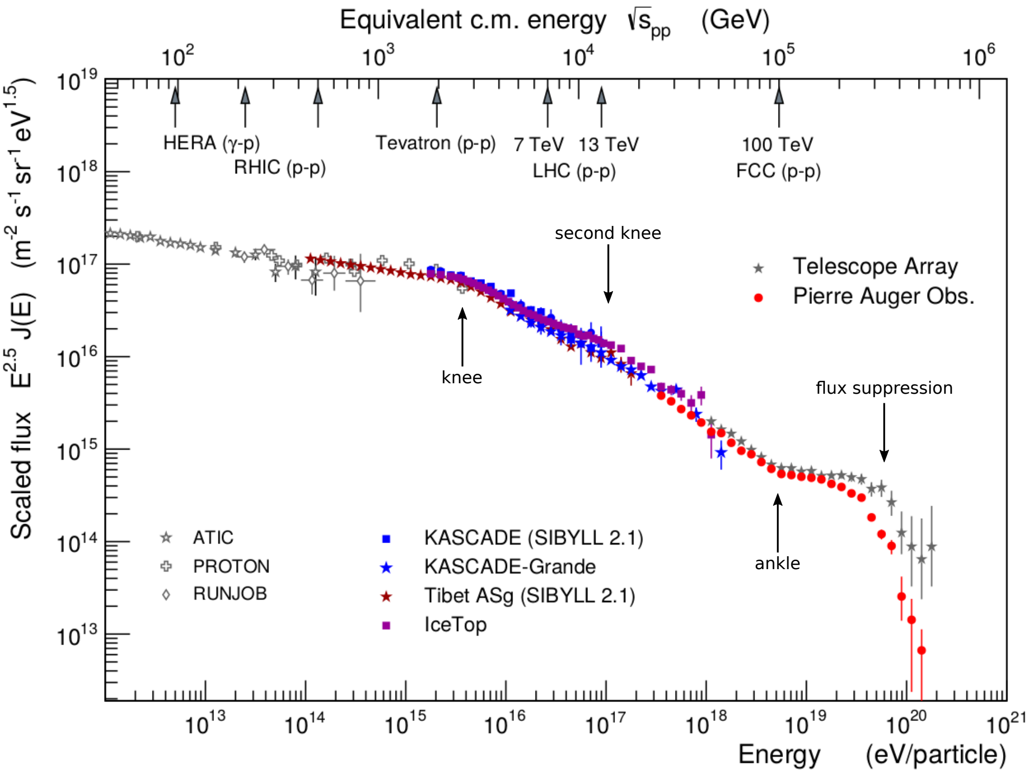

Figure 2.2: Differential energy spectrum of cosmic rays measured by several air shower experiments. The flux is scaled with $E^{2.5}$ to uncover the characteristic features of the spectrum. Figure adopted from [7], updated plot of [8].

2.2 Energy spectrum

Measurements of the particle flux from different experiments over a large energy range are summarized in Fig. 2.2. The differential flux of cosmic rays, J, is given by the number of particles, N, per energy, E, solid angle, Ω, area, A, and time, t. It approximately follows a power law with varying spectral index, γ:

$$J(E) = \frac{\mathrm{d}^4 N}{\mathrm{d}E\,\mathrm{d}\Omega\,\mathrm{d}A\,\mathrm{d}t} \propto E^{-\gamma}. \tag{2.1}$$

The flux shown in Fig. 2.2 is re-scaled with $E^{2.5}$ to display the features of the spectrum more clearly. The spectral index changes at certain energies. This is in general interpreted as a change in the origin, propagation, or mass composition of the cosmic rays.

The energy spectrum is generally interpreted by assuming that cosmic rays with energies below $\sim 10^{18}$ eV are dominated by cosmic rays of galactic origin. At the *knee* at $\sim 5 \cdot 10^{15}$ eV the spectrum steepens from a spectral index $\gamma = 2.7$ to $\gamma = 3.1$. Here, galactic accelerators have reached their maximum achievable energy for protons and the composition changes to heavier primary particles up to the *second knee* at $\sim 10^{17}$ eV, where the spectral index changes again to $\gamma = 3.2$. The *ankle* at $\sim 5 \cdot 10^{18}$ eV is thought to mark the transition from galactic to extragalactic origin of the cosmic rays and the spectrum flattens to $\gamma = 2.6$. At $\sim 5 \cdot 10^{19}$ eV a strong cutoff of the spectrum is found. The exact modeling and interpretation of the cutoff is still under debate, a recent analysis of the Pierre Auger Observatory revealed a sharp softening of the spectrum at energies beyond the cutoff where the spectral index increases up to $\gamma \approx 5$ [9].

Two dominating scenarios can be distinguished by the composition of cosmic rays at the highest energies. The first scenario, the so-called *GZK effect*, explains the cutoff by energy losses of cosmic ray interactions with photons from the *cosmic microwave background* (CMB) during the propagation through space. In this case, the highest energy cosmic rays should be proton dominated. In the second scenario the extragalactic accelerators have reached their maximum energy. As the maximum achievable energy of a source increases proportional to the charge Z of the nucleus, a heavier composition, e.g. iron primaries, is expected at the highest energies. It is therefore of crucial importance to study the composition of cosmic rays around the cutoff.

2.3 Mass composition

At lower energies the properties of cosmic rays, especially their energy and mass, can be measured directly, e.g. with the AMS detector on the International Space Station [10]. At higher energies the mass needs to be reconstructed indirectly from air shower observables and can only be estimated with larger uncertainties than in direct measurements [11]. Often, only an energy-dependent average mass estimation is feasible. An event-by-event estimation of the mass is still an active field of research and the primary goal of the AugerPrime upgrade of the Pierre Auger Observatory [12], cf. section 3.4.

A standard estimator of the mass of the primary particle is given by X_{max}. For the same energy, a heavier primary reaches its shower maximum higher in the atmosphere than a lighter primary. Another estimator is given by the spread of the X_{max} distribution, as fewer fluctuations are expected for heavier primaries. At the Pierre Auger Observatory X_{max} can be measured directly with the Fluorescence Detector, cf. chapter 3. The results are shown in Fig. 2.3 and compared to the prediction of air shower simulations with different hadronic interaction models. With both methods, the mean and spread of X_{max}, a transition towards heavier primaries above the ankle is observed.

The Auger data can be described by a simultaneous fit of the energy spectrum and the X_{max} distribution assuming certain scenarios on the injection of cosmic rays at the (unknown) sources. In a benchmark scenario, where the sources accelerate the primary up to a maximum energy that is proportional to their charge Z, the data is described best by a model with four different mass components as illustrated in Fig. 2.4, cf. [15] for details. A light composition is disfavored for the highest energies, however, a sub-dominant light component is not excluded. The Auger data is described best by including a heavier mass component up to iron primaries at the highest energies.

Due to the systematic uncertainties of the hadronic interaction models as well as the low number of events at the highest energy the results are not yet conclusive. With

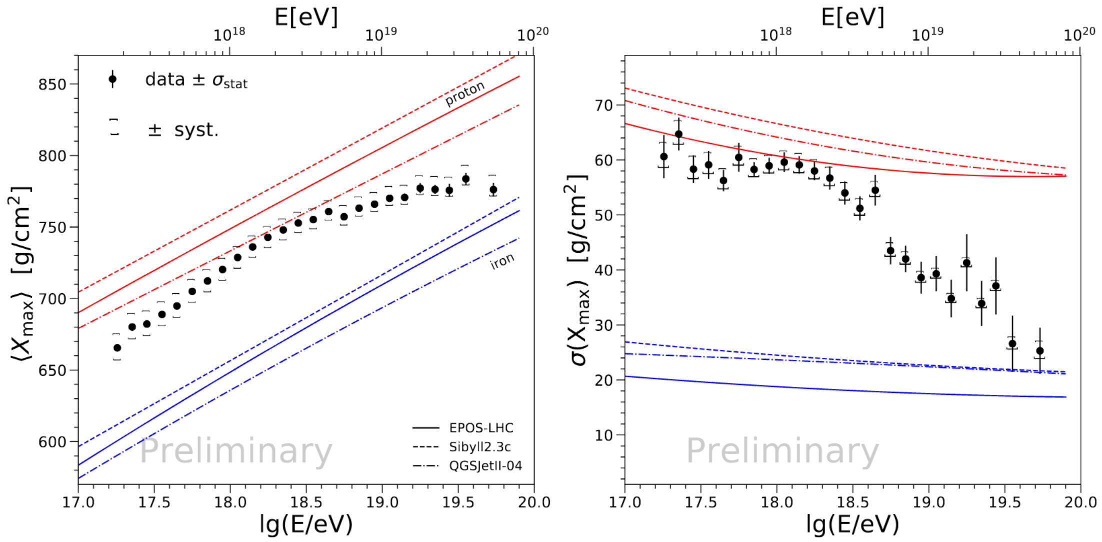

Figure 2.3: Recent results of the Pierre Auger Observatory for the mean $X_{\max}$ (left) and its spread (right) as a function of the primary energy. The predicted values for proton and iron primaries are obtained from simulations using different hadronic interaction models. Figure from [13].

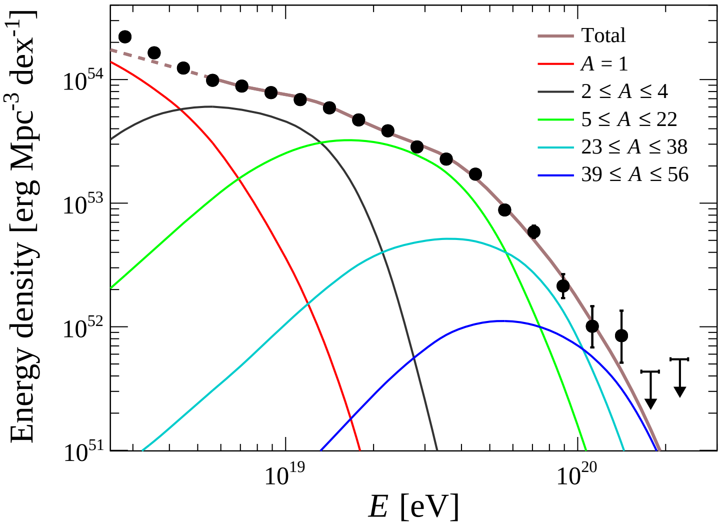

Figure 2.4: Illustration of the energy density obtained in a benchmark scenario with four different mass components. An additional component (e.g. a Galactic component) is needed for describing the spectrum in the energy range of the dashed curve. Figure from [14].

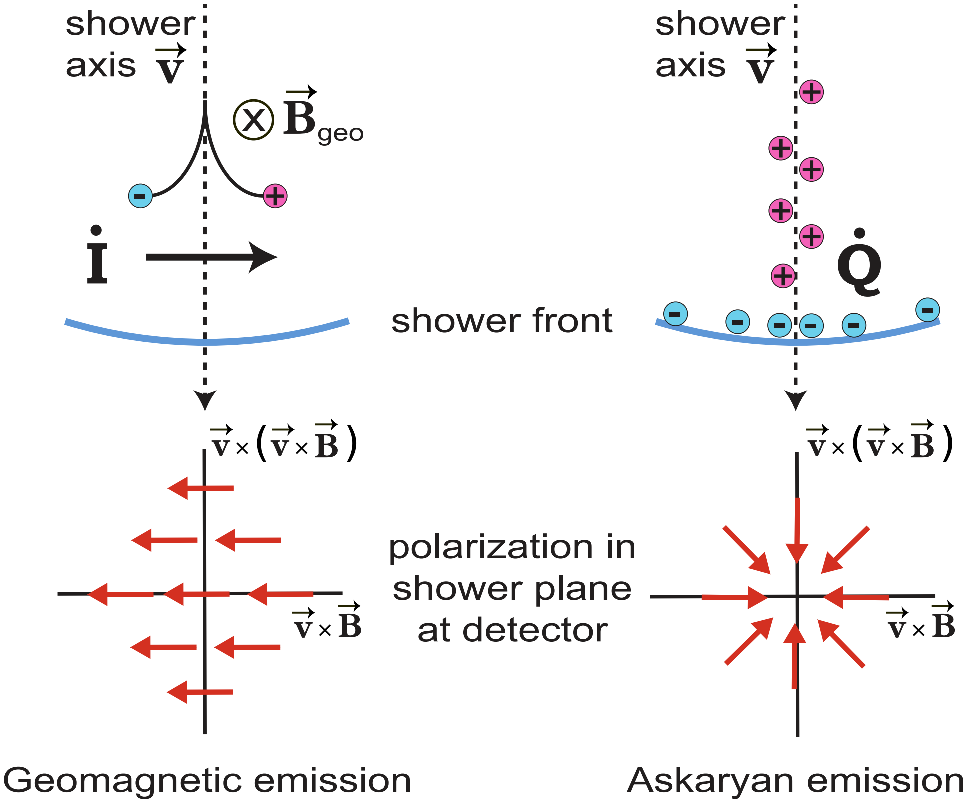

Figure 2.5: Schematic sketch of the two dominant radio emission mechanisms and their polarization pattern in the shower plane. Figure adopted from [3].

AugerPrime the uptime of the Fluorescence Detector will be increased to improve statistics at the highest energies. Moreover, new detector systems will be installed to reconstruct the mass using a hybrid reconstruction of the different detector systems independently of the Fluorescence Detector.

2.4 Radio emission from extensive air showers

The radio emission of an air shower originates from two different emission processes: the *geomagnetic emission* [16] and the *charge-excess*, also known as *Askaryan effect* [17]. The two emission mechanisms and their polarization pattern in the shower plane are depicted in Fig. 2.5. For air showers the geomagnetic emission is typically dominating.

The geomagnetic emission arises from the deflection of electrons and positrons in the air shower by the Earth's magnetic field. This induces a transverse drift current in the air that is varying in time as the number of electrons and positrons changes during the shower development. The resulting radio emission is linearly polarized along the direction of the Lorentz force, i.e. in $\vec{v} \times \vec{B}$ direction. Its amplitude is proportional to the strength of the geomagnetic field B and the sine of the angle between the shower direction and the geomagnetic field, α. Therefore, the detection threshold and reconstruction efficiency depend on the arrival direction of the air shower [18].

The charge excess emission arises from a time-varying negative charge-excess in the shower front. Atmospheric molecules get ionized by high-energy particles of the air shower. The knocked-out relativistic electrons propagate together with the shower front and partially annihilate with positrons in the shower. In total, the shower front accumulates a negative charge excess and a positively charged plasma is created behind the shower. Thus, a longitudinal current along the shower axis is induced whose strength varies with the shower development. This yields a radio emission that is polarized radially to the shower axis.

The measured radio emission on ground is given by the superposition of both emission mechanisms. The relative strength of the charge-excess emission, a, with respect to the geomagnetic emission, normalized to an air shower arriving perpendicularly to the geomagnetic field, is defined as

$$a = \sin\alpha \frac{|\vec{E}_{\mathrm{ce}}|}{|\vec{E}_{\mathrm{geo}}|}, \tag{2.2}$$

where $\vec{E}_{\mathrm{ce}}$ and $\vec{E}_{\mathrm{geo}}$ are the electric-field amplitudes of the charge-excess and geomagnetic emission, respectively. The *charge-excess fraction* varies e.g. with the incoming direction of the air shower and the absolute strength of the geomagnetic field. The geomagnetic field strength at the Pierre Auger Observatory is roughly two times weaker compared to other cosmic-ray radio experiments such as LOFAR [19]. Hence, the geomagnetic emission is expected to be two times weaker at Auger and therefore a is expected to be larger, making it easier to measure the effect of the charge-excess. At the Pierre Auger Observatory the average charge-excess fraction has been measured as 0.14 ± 0.02 [20].

More detailed measurements by LOFAR with many radio antennas have confirmed the predicted polarization patterns and the interplay of both emission mechanisms. Furthermore, a dependence of a on the zenith angle of the air shower was found [21]. In a pure MC study [22] this dependency was described with a correlation of a and the air density at the shower maximum. For vertical air showers with a high air density at the shower maximum the predicted a is $\sim 40\,\%$, for highly inclined air showers and a small density at the shower maximum a drops below $5\,\%$.

Due to the superposition of the radio emission of both mechanisms the lateral distribution of the radio signal is asymmetric and can not be described by a one-dimensional distribution function as used for the particle component of an EAS. Thus, it has to be described with a two-dimensional function depending not only on the radial distance but also on the polar angle. The shape is best understood in a coordinate system where the x-axis is aligned with the $\vec{v} \times \vec{B}$ direction and the y-axis with the $\vec{v} \times (\vec{v} \times \vec{B})$ direction. In this coordinate system, the two emission mechanisms interfere destructively on the negative $\vec{v} \times \vec{B}$ half-plane and constructively on the positive $\vec{v} \times \vec{B}$ half-plane.

In addition, the refractive index n of the atmosphere impacts the radio emission. It is larger than unity and changes with the atmospheric height. For an observer who sees the air shower at the so-called *Cherenkov angle*, $\theta_{\mathrm{Ch}} \approx \arccos(1/n)$, signals emitted at different stages of the shower development arrive at the same time. This leads to a

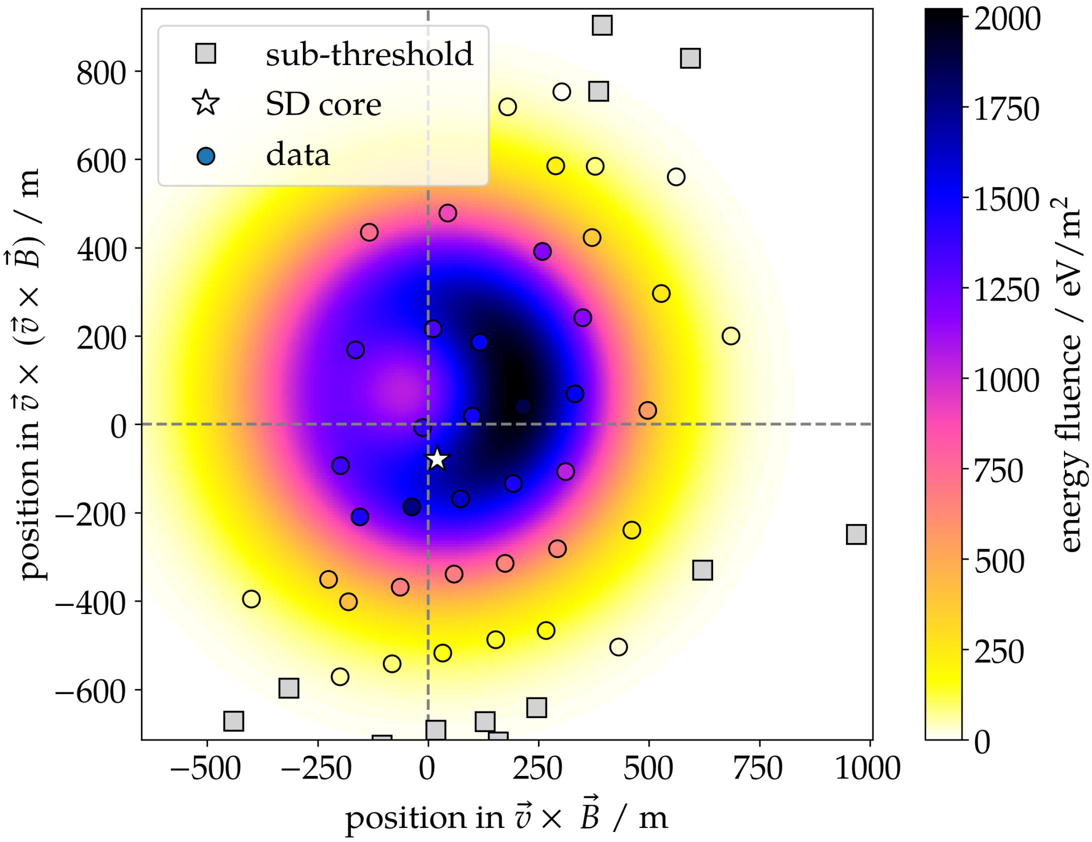

Figure 2.6: Example of the two-dimensional lateral distribution of the radio signal in the plane perpendicular to the shower axis for an event measured by the Auger Engineering Radio Array with the radio ID 101258.165673. The axes are aligned in $\vec{v} \times \vec{B}$ and $\vec{v} \times (\vec{v} \times \vec{B})$ direction. The event was reconstructed by the Surface Detector of the Pierre Auger Observatory with a zenith angle of $(67.7 \pm 0.2)°$, coming from North-West at $(138.5 \pm 0.2)°$ and an energy of (9.46 ± 0.92) EeV. The background shows a fit to the lateral distribution of the radio emission, the measurements are indicated as circles where the color indicates the reconstructed energy fluence. The reconstructed radio core is in the coordinate origin.

compression of the radio signal on a ring with an increased signal strength around the shower axis, the *Cherenkov ring* [23]. In air, the Cherenkov angle is ∼1° for vertical air showers and decreases to ∼0.4° for inclined air showers since the emission region is higher in the atmosphere with a smaller refractive index.

Both effects lead to a bean-like shape of the radio signal in the shower plane where the maximum of the radio signal is shifted away from the shower core [24]. An example of the lateral distribution of the radio emission is shown in Fig. 2.6 for an event with a zenith angle of ∼68° reconstructed with the Auger Engineering Radio Array (cf. chapter 3). For more inclined air showers the charge-excess fraction reduces further and the asymmetry due to the interference gets less prominent.

2.5 Simulation of air showers

To simulate an air shower, all shower particles, their interactions and decays need to be tracked through the atmosphere. Hence, the simulation requires a modeling of hadronic and electromagnetic interactions at energies much higher than accessible in accelerator experiments as well as a detailed description of the atmosphere itself. Different models for the high-energy hadronic interactions are available, typically they are tuned to data of the Large Hadron Collider (LHC) [25] and then extrapolated to higher energies. The most common models for air shower simulations are QGSJetII [26], EPOS-LHC [27] and SIBYLL [28]. Separate models are used for low-energy interactions, usually FLUKA [29] or UrQMD [30].

Two full Monte Carlo simulations codes exist for the simulation of air showers: CORSIKA (**CO**smic **R**ay **SI**mulation for **KA**SCADE) [31] and AIRES (**AIR** shower **E**xtended **S**imulations) [32]. In this thesis CORSIKA is used as it is better maintained and offers more features like parallel computing through MPI (Message Passing Interface) which will be important for energies above 10 EeV. The setup of a CORSIKA simulation is defined in an input card, cf. appendix A for an example, where physical parameters e.g. the type of the primary particle, the energy and direction, observation level, magnetic field, atmospheric model, and technical parameters for the simulation are specified. The primary is then injected at the top of the atmosphere at a height of 112.8 km above sea level.

The number of secondary particles scales with the primary energy, e.g. for a 10^{20} eV proton air shower more than 10^{11} particles have to be tracked by CORSIKA. This is computationally not feasible. Furthermore, many of these particles will have low energies and will not be relevant for the final outcome of the simulation. Therefore, a thinning technique can be applied that will keep the number of followed particles in the low-energy part of the shower reasonably low instead of exponentially increasing. If thinning is used, only a randomly selected fraction of particles below a configurable energy threshold will be followed. A weighting factor is applied to those particles to ensure energy conservation. There is an optimized weight limitation for CORSIKA that enhances the statistical precision for particle densities and minimizes the computation time [33].

For the simulation of the radio emission of an air shower CoREAS (**CO**RSIKA-based **R**adio **E**mission from **A**ir **S**howers) [34] is used. CoREAS is directly integrated into CORSIKA and calculates the radio emission of electrons and positrons using the *endpoint formalism* [35] which is based on classical electromagnetism. Each particle trajectory is described as a series of straight tracks. The radiation is then calculated from the instantaneous acceleration of a charged particle at the beginning and the endpoint of each track. The final radio pulse is given as the superposition of the radiation from all tracks. It is provided in the form of electric field traces of the East-West, North-South, and vertical components. The simulated time traces need to be bandpass filtered to the bandwidth of the individual experiment.

This approach is computationally expensive as the calculation needs to be performed separately for each observer position. Especially in the case of inclined air showers a precise integration of the refractive index between the observer position and the endpoints is necessary. These integrals can only be solved numerically as the curvature of the atmosphere has to be taken into account. In an optimized version of CoREAS these integrals are precalculated and lookup tables are generated to speed up simulations of inclined air showers.

The calculation of the radio emission does not involve any free parameter. Uncertainties only arise from approximations made in the simulation, like the thinning algorithm, the description of the atmosphere, and the development of the air shower itself, which is dominated by the uncertainties in the hadronic interaction models. It is thus a huge advantage that there are two completely independent Monte Carlo codes, CoREAS and ZHAireS [36], that can be compared directly. ZHAireS is a modified version of AIRES where the radio emission of the air shower is calculated using the *ZHS formalism* [37]. It has been shown that the ZHS and the endpoint formalism are mathematically equivalent [38, 39]. However, the numerical implementation of both formalisms could add additional uncertainties to the predicted radio emission.

In a dedicated study [40, 41] the predicated radio emission of CoREAS simulations was compared to simulations made by ZHAireS. It was found that the deviation of both codes amounts to 2.6 % for the absolute scale of the electromagnetic energy of the air shower. The result validates the consistent implementation of the radio emission in both codes. Other systematic uncertainties, such as the hadronic interaction model, approximations in the air shower simulation, and the state of the atmosphere have already been studied in [22]. Interpreting the deviation of both codes as a systematic uncertainty, it dominates the overall systematic uncertainty. The overall systematic uncertainty is small compared to other methods, hence, the radio emission of EAS has the potential to set an accurate absolute energy scale for cosmic-ray detectors.

3 | Pierre Auger Observatory

The *Pierre Auger Observatory* [42], covering an area of 3000 km^2, is the world's largest observatory for the detection of cosmic rays. It is located in the province of Mendoza in Argentina, next to the city of Malargüe at an average height of 1400 m above sea level. It is designed as a hybrid detector measuring cosmic-ray air showers from 10^{17} eV to beyond 10^{20} eV with complementary detection techniques.

The two baseline components are a large *Surface Detector* array (SD) [43] and a *Fluorescence Detector* (FD) [44]. The SD consists of 1660 stations and is overlooked by 24 FD telescopes located at four different sites around the SD array as shown in Fig. 3.1. In the western part of the array, the so-called enhancements area, several new technologies to detect ultra-high-energy cosmic rays are studied. Here, a *Muon Detector* (MD) [45] consisting of underground scintillators is installed to measure the muon content of an air shower independently of the electromagnetic particles. Three additional tilted FD telescopes [46] are installed to measure the early development of lower energetic air showers. Most important for this work is the *Auger Engineering Radio Array* (AERA) [47, 48] which measures the radio emission from air showers in the 30 to 80 MHz regime in coincidence with the other detectors.

The observatory has been collecting data since 2004 and the baseline components were completed in 2008. It is in permanent operation since then and has recorded data of UHECR with significant statistics. In this chapter an overview of the different components of the Observatory is given.

3.1 Surface Detector

The Surface Detector consists of 1660 water Cherenkov detector (WCD) stations distributed on a hexagonal grid with varying spacing. In the regular array the distance of neighboring stations is 1500 m. Within the enhancements area the spacing is reduced to 750 m or 433 m to detect cosmic rays of lower energy with high statistics. Each detector station consists of a water tank with a diameter of 3.5 m and a height of 1.2 m filled with 12 m^3 of ultra-pure water. Due to the height of 1.2 m the SD stations are also sensitive to inclined air showers, which is a significant advantage compared to flat scintillators as used e.g. by the *Telescope Array* (TA) [50]. A picture of an SD station is shown in Fig. 3.2.

With the SD a snapshot of the air shower at the time of arrival, i.e. the signal footprint on ground, is detected. The secondary electromagnetic and muonic particles of the air shower produce Cherenkov light inside the water as they propagate faster than the speed of light in water. The Cherenkov light is reflected diffusely from the border of the water

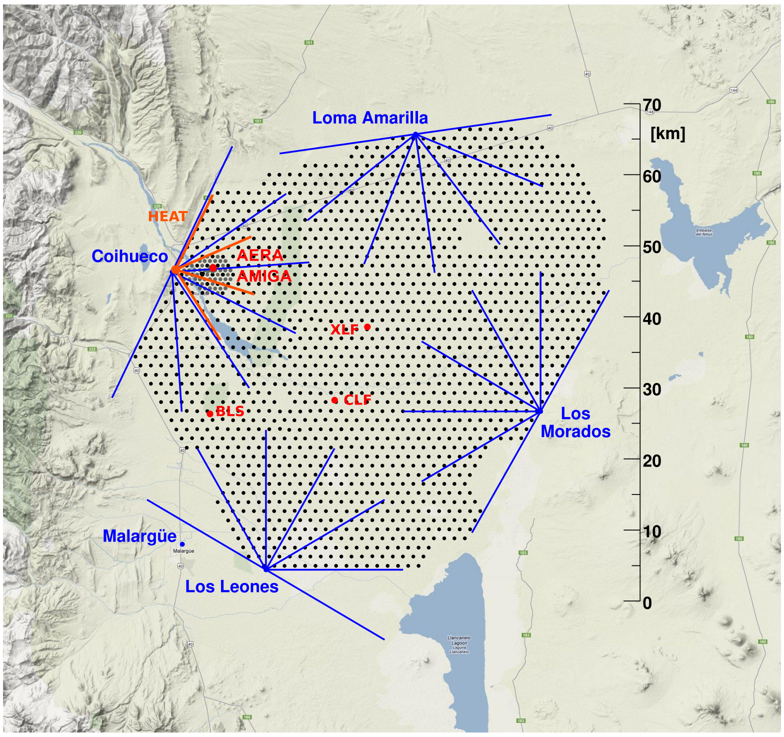

Figure 3.1: Map of the Pierre Auger Observatory. Each dot corresponds to an SD station. The field of view of the 24 FD telescopes (blue) and HEAT (red) is indicated by colored lines. HEAT is located next to the Coihueco telescope building. The location of AERA and AMIGA inside of the enhancements area are indicated by a red dot. Figure from [49].

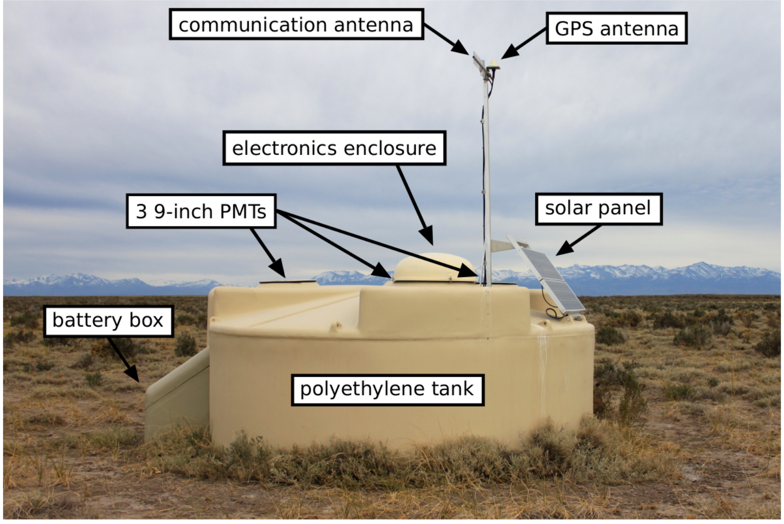

Figure 3.2: Image of a Surface Detector station in the field with labels for the main components. Figure from [51].

tank until it is eventually detected by one of the three 9-inch diameter *photomultiplier tubes* (PMTs) that are installed at the top of the tank facing downwards into the water.

Each station works autonomously and is powered by solar panels that are installed on top of the station. The PMT signal is digitized and converted into units of VEM, the signal equivalent to a vertical muon traversing the SD tank. If the signal passes the local trigger on station level the trigger information is sent to the *Central Data Acquisition System* (CDAS) [52]. There, the local station triggers are combined to an air shower trigger that will trigger the read-out of the measured signal traces of all participating stations.

3.2 Fluorescence Detector

The Fluorescence Detector consists of 4 buildings (called Los Leones, Los Morados, Loma Amarilla, and Coihueco) that are located at the periphery of the SD array. Each building contains 6 telescopes, each with a field of view of $30^\circ \times 30^\circ$ in azimuth and elevation. Combined, they have an azimuth coverage of 180° and are oriented towards the interior of the SD. A picture of an FD building is shown in Fig. 3.3 (left). Three additional telescopes (*High Elevation Auger Telescopes* - HEAT) are installed next to Coihueco. Their buildings can be tilted upwards to extend the field of view of the Coihueco telescopes by almost 30° in elevation. With the regular FD every air shower above 10^{19} eV that arrives within the SD is recorded by at least one telescope. With HEAT the minimal energy is extended down to 10^{17} eV. The FD can only be operated during dark and moonless nights with clear weather conditions. This reduces its duty cycle to $\sim$15 %. It is always operated in a hybrid mode such that the same air shower is measured simultaneously by the FD and the SD.

The FD detects the fluorescence light that is emitted by atmospheric nitrogen within the UV range after being excited by the particles of the air shower, providing a measurement of the whole longitudinal shower profile. In Fig. 3.3 (right) the telescope and its main components are sketched. The fluorescence light enters the room of the telescopes through an aperture system with a filter transparent to UV reducing the amount of background light. The fluorescence light is then reflected from a $13\,\mathrm{m}^2$ segmented spherical mirror onto the camera. The aperture is protected by a shutter and a curtain to protect the camera from unexpected direct light.

For a precise estimation of the cosmic-ray energy the amount of fluorescence light emitted by a certain amount of deposited energy, the *light yield*, needs to be measured in a laboratory. Calibrations of the telescopes' cameras, relative and end-to-end, are performed regularly. The fluorescence light is attenuated and scattered on the way from the shower to the telescopes. Therefore, the atmosphere can be seen as part of the detector and has to be monitored carefully. At every FD building the atmospheric conditions and cloud coverage are monitored with a lidar (light detection and ranging) station, a ground-based weather station, and a cloud camera. In addition, lasers are located at the *Central Laser Facility* (CLF) [53] and the *eXtreme Laser Facility* (XLF) [54], both located close to the center of the array (cf. Fig. 3.1). Collimated UV-laser pulses are

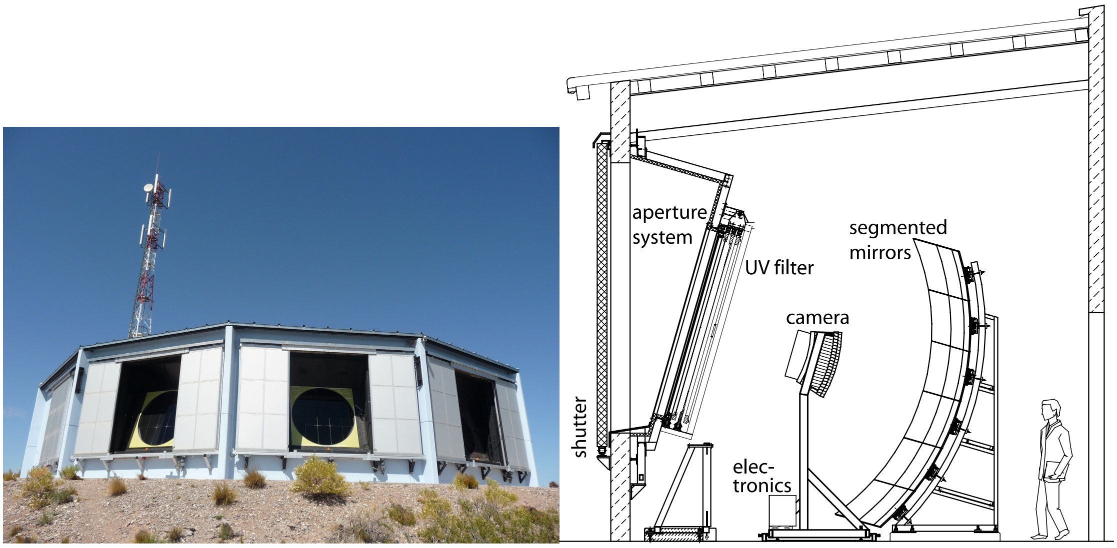

Figure 3.3: Image of an FD building (Los Leones) from outside (left). Schematic view of an FD telescope with a description of its main components (right). Figures from [42].

shot into the atmosphere and the scattered light is detected by the telescopes. As the source is well known, information about the aerosol properties in the line of sight can be derived, which is necessary for an accurate shower reconstruction.

3.3 Auger Engineering Radio Array

AERA is the radio extension of the Pierre Auger Observatory, located within the 750 m array of the SD and in the field of view of the Coihueco telescope and HEAT. It measures the radio emission of an air shower in the frequency range of 30 to 80 MHz. AERA detects air showers with energies above 10^{17} eV which coincides with the energy threshold of the 750 m SD array and HEAT, and thus allows for a coincident detection of air showers with all three detector systems. It is designed as an engineering array to prove the feasibility of the radio detection technique and make it applicable to future large-scale radio arrays. Different types of detector stations, using different antenna models, electronics, and trigger systems, have been designed and are still used for AERA. This imposes challenges on the used reconstruction software as it has to be able to deal with the different responses of individual detector stations as well as with a time-varying detector layout.

AERA was deployed in three phases. The first 24 stations (AERA24) were installed during the austral summer 2011 on a 144 m triangular grid covering a total area of 0.4 km^2. 100 additional stations (AERA124) have been deployed in May 2013 with a larger spacing of 250 m or 375 m covering a total area of 6 km^2. The deployment of additional 29 stations (AERA153) with a spacing of up to 750 m in March 2015 finalized the current layout of AERA with a total instrumented area of 17 km^2. A map of the individual deployment phases of AERA is presented in Fig. 3.4. The last deployment

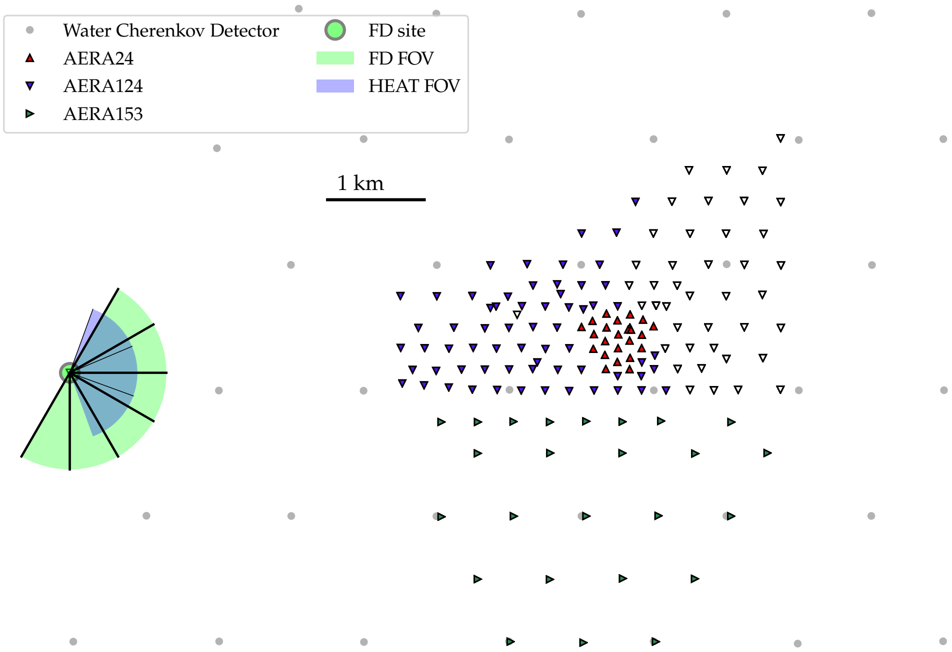

Figure 3.4: Schematic map of AERA. The orientation of the triangles indicate the three deployment phases, empty triangles denote stations that are operated in self-trigger mode. Only the water Cherenkov stations with a grid spacing of 1500 m are shown.

was especially designed to explore the potential of reconstructing inclined air showers with a sparse radio array.

Every radio station consists of two perpendicular antennas, one aligned into the magnetic North-South direction and the other into the East-West direction. The full electric field pulse can be reconstructed from these two polarizations if the direction of the pulse is known. For the first 24 radio stations a *logarithmic periodic dipole antenna* (LPDA) is used, the later phases use a *butterfly* antenna. A detailed description of both antenna types is given in [55]. Fig. 3.5 shows an image of radio stations with both antenna models. The stations work autonomously and are solar powered. The local electronics consist of a *low noise amplifier* (LNA) that amplifies the recorded signal. The amplified signal is then sent to a bandpass filter and a digitizer. For the 24 LPDA stations the measured data is sent to the *Central Radio Station* (CRS) via optical fibers [56]. From the CRS the data is sent to the central Data Acquisition (DAQ) of AERA located in the Coihueco building via a commercial wireless link. The butterfly stations are equipped with a communication antenna to directly send their data to the DAQ.

Two different air shower trigger systems, a self-trigger and an external trigger, are implemented to read out the radio data. Most of the radio stations receive an external

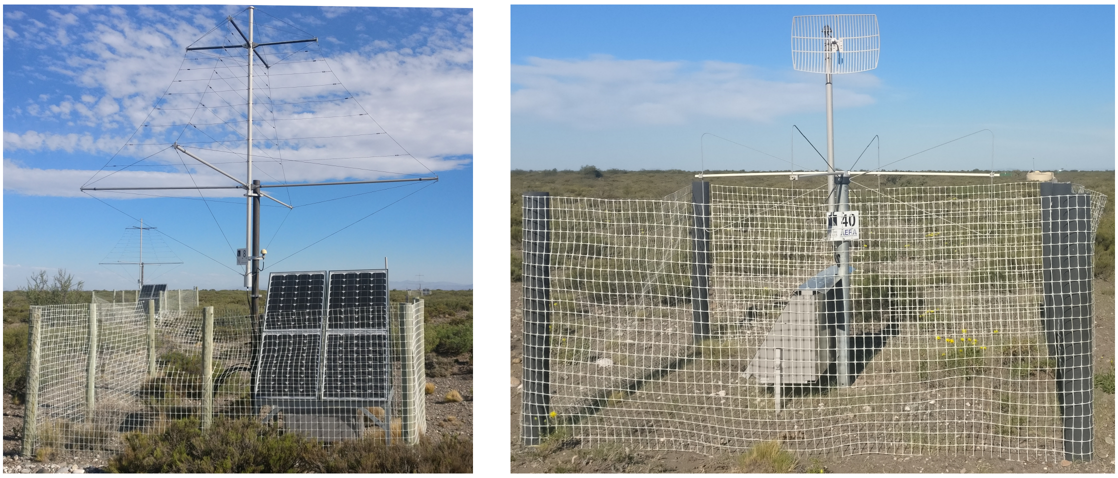

Figure 3.5: Image of the antenna types used in AERA: LPDA (left) and butterfly (right).

trigger from the SD or the FD. Initially, 6 stations of the first deployment phase were self-triggered, but their electronics were changed in January 2016 to receive external triggers instead. The 40 stations located in the Eastern part of AERA124 are still operated in self-trigger mode. The external trigger by the SD is discussed further in section 4.4.

The recorded radio signal is a convolution of the true radio signal and the response of the readout electronics. Hence, a detailed understanding of the antenna response pattern and the readout electronics is crucial to extract the physical radio signal of the air shower from the recorded trace. Several calibration campaigns were performed to obtain the absolute calibration of the antenna response to cosmic-ray radio signals, e.g. [57] for the calibration of the LPDA. Also the timing of the individual radio stations needs to be calibrated. The absolute timing is provided by the GPS receiver at each station, however, the GPS clocks of different radio stations have shown large offsets and their resolution is not precise enough to reconstruct the shape of the radio wavefront with high precision. Therefore, a relative timing calibration is performed with a reference transmitter, the *beacon*, that is installed at Coihueco [58]. With the beacon a time accuracy of $\sim 2\,\mathrm{ns}$ is achieved. The accuracy of this method was confirmed by fully independent measurements using radio waves transmitted by commercial airplanes. As the energy that is radiated in the form of radio signals is vastly independent of the atmospheric conditions and, unlike for the FD, there is neither significant absorption nor scattering of the radio emission, only very basic monitoring of the atmosphere is necessary.

3.4 AugerPrime

The Pierre Auger Observatory is currently being upgraded especially to improve the mass separation achieved with the SD, ideally up to an event-by-event basis. This is a key ingredient for the understanding of the flux suppression at the highest energies and

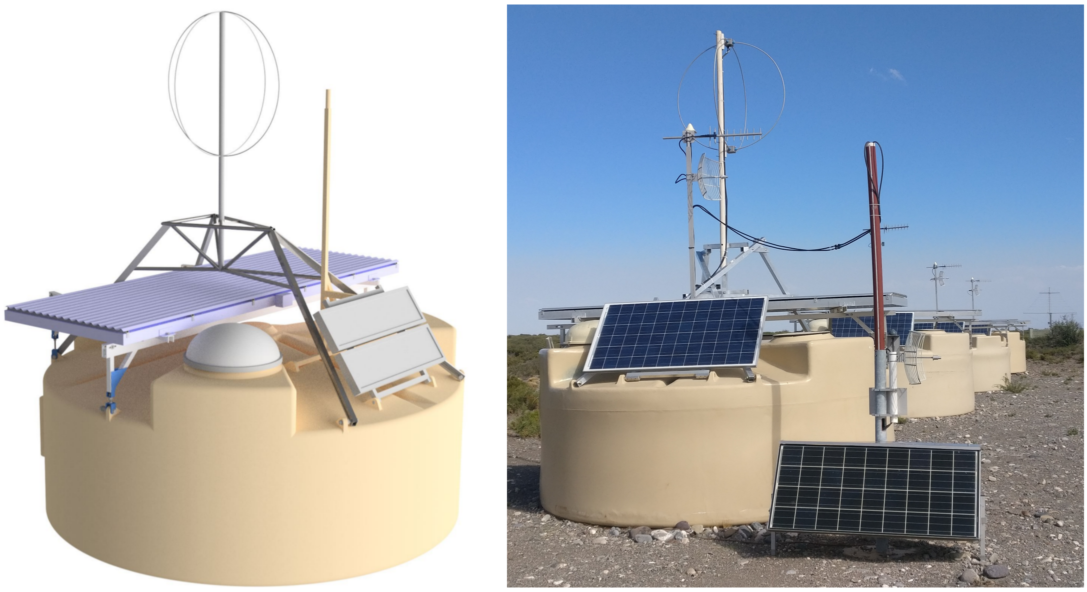

Figure 3.6: 3D model of an upgraded SD station comprised of the WCD, the SSD and a SALLA antenna on top (left). Figure from [59]. Image of the first prototype station in the field (right).

also relevant for the understanding of hadronic interactions at energies much higher than accessible by man-made accelerators.

With *AugerPrime* [12] the duty-cycle of the FD will be extended significantly by operating during higher night-sky brightness with a reduced PMT gain. In addition, all SD stations will be equipped with a plastic scintillator (*Surface Scintillator Detector* - SSD) on top of the existing water Cherenkov detector station. Both detector subsystems, the WCD and the SSD, have different responses to electromagnetic particles and muons such that the two components can be separated. This enables mass sensitivity for vertical air showers. However, a flat scintillator is insensitive to inclined air showers due to the small geometric cross-section. The SSD is currently being deployed and was not taking data during the time period that is analyzed in this thesis.

More recently, also a *Radio Detector* [60] became part of AugerPrime. Inclined air showers have a large radio footprint on the ground, cf. chapter 5 and chapter 6, and can therefore be detected with a sparse antenna array with a spacing of 1.5 km. Every SD station will be equipped with a *short aperiodic loaded loop antenna* (SALLA) on top of the WCD and SSD as shown in Fig. 3.6. For inclined air showers the electromagnetic and hadronic components are absorbed in the atmosphere and only the muonic component can be measured by a particle detector on the ground. In contrast to that, the radio emission of an air shower originates almost solely from its electromagnetic component. Hence, the Radio Detector increases the zenith angle range, and therefore also the sky coverage, for separate measurement of the electromagnetic and muonic component of the air shower.

With the AugerPrime Radio Detector the Pierre Auger Observatory will comprise the world's largest radio detector for cosmic rays with an area of 3000 km^2. This will allow for the study of a variety of science cases, such as the muon content in air showers and the mass composition of cosmic rays. The potential of both as well as a proof-of-principle of the methods based on measured AERA data is presented in chapter 7.

Note that throughout this thesis the term „RD“ will be used for AERA. In cases where the AugerPrime Radio Detector is meant (which is nowadays called RD, analogous to SD and FD) it will be stated explicitly. Furthermore, „SD“ refers to the WCD only.

4 | Data Processing and Reconstruction

For the analysis of the measured data and simulated air showers the analysis software of the Pierre Auger Observatory, Offline [61], is used. In this chapter the general design of Offline is described and an overview of the relevant steps to reconstruct an air shower is given. Furthermore, the used set of simulated events and the event selection tool are described.

4.1 The Offline Framework

Offline is a C++ framework originally developed to reconstruct air showers from measured SD and FD data. It can read in several data formats used in the Auger collaboration as well as the output of various air shower simulation codes such as CORSIKA/CoREAS and Aires/ZHAireS. Offline was later extended for additional detector components such as the radio detector [62]. This was possible due to the modular design of the software. Offline is structured in three principal parts as shown in Fig. 4.1: the detector description, the event data, and the data processing chain.

The detector description contains information about the individual detector components stored in XML files and MySQL databases. Static information such as the position of the detector stations are stored in XML, time-dependent information, e.g. the hardware description that can change, bad periods with hardware and/or software failures, or atmospheric conditions, is stored in databases.

The event class stores the event data of the individual detector components. This includes raw data, such as measured traces, and reconstructed quantities, e.g. the shower

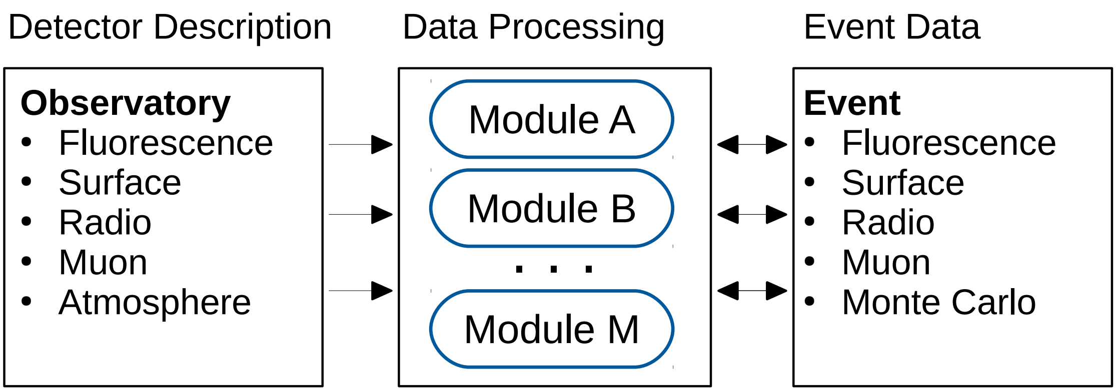

Figure 4.1: The three fundamental parts of the Offline framework. Figure adapted from [61].

direction. If a simulation is processed with Offline the true MC values are stored in the event data as well.

The data processing is divided into individual modules that are executed sequentially. Each module contains the algorithm for a specific analysis step and can read the detector description if needed. The modules have no direct interface to each other, all information is read and stored in the event class.

An additional collection of utility classes complements the main structure of Offline. A default system of physical units is defined and units are automatically handled correctly within Offline, only for input and output the user has to specify units. Since the observatory consists of different instruments spread over a large area with relevant Earth curvature there is no preferred coordinate system in Auger. Different coordinate systems are used in Offline, the necessary coordinate transformations are handled automatically by a geometry package. Another feature, that was developed for the analysis of radio data, is a class to store time series of the electric field trace. The radio reconstruction works on both the time trace and the frequency spectrum. A corresponding Fourier transformation is performed automatically if necessary.

This design enforces a clear separation of algorithms and data. As all reconstruction steps are modularized, an existing pipeline can be extended easily by adding additional modules while different reconstruction approaches can be tested by exchanging the corresponding modules. The final reconstruction is defined by the sequence of used modules, the so-called `ModuleSequence.xml`, and the setting of configurable parameters for each module that are defined in the `bootstrap.xml`. Baseline reconstructions are stored in Offline that can be used as a reference and adjusted for the desired analysis. In this work two standard reconstructions, `RdHASObserver` and `RdHASSimulationObserver`, were developed for the analysis of inclined air showers[1]. They are based on the results of [63] which proved the feasibility of the radio detection for inclined air showers.

The results of the reconstruction are written into a so-called ADST (Advanced Data Summary Tree) file based on ROOT [64]. The ADST file contains the detector description, the event data, and the configuration of Offline. Further analyses of the data can be performed on ADST files only. Furthermore, ADST files can be opened in an `EventBrowser` that visualizes the reconstructed events and raw event information of the different detectors.

4.2 SD reconstruction

Important features of the lateral particle profile of an air shower depend on the zenith angle. Hence, the SD reconstruction differs for vertical and inclined air showers as the recorded signals change drastically. For vertical air showers the measured signals of the SD are dominated by electromagnetic particles. The typical path lengths are small, thus the geomagnetic field does not impact the lateral profile significantly. The signal as a function of distance to the shower axis is fitted with a modified Nishimura-Kamata-

---

[1] Inclined air showers were called horizontal air showers (HAS) in the past. The abbreviation HAS is still used.

Greisen (NKG) function [65]. To estimate the energy the signal at an axis distance of 1000 m, $S(1000)$ [66], corrected for a well-understood zenith angle dependence [67, 68], is used. It is calibrated using hybrid events that include an FD event with an accurate energy reconstruction.

The SD signal of an inclined air shower is dominated by muons. Here, the magnetic field yields a separation of positively and negatively charged muons due to the longer propagation through the atmosphere. This results in complicated muon density patterns ρ_μ in the ground plane. The shape of the muon distribution was shown to be almost universal and depends only weakly on the primary particle, its energy, and the used hadronic interaction model. The muon number density scales nearly linearly with the primary energy, hence the expected muon number density at the ground can be written as:

$$\rho_\mu(\vec{r}; \theta, \phi, E) = N_{19} \cdot \rho_{\mu,19}(\vec{r}; \theta, \phi). \tag{4.1}$$

Here, N_{19} is a scaling parameter relative to the average muon distribution $\rho_{\mu,19}(\vec{r}; \theta, \phi)$ of 10^{19} eV proton primaries simulated with the hadronic interaction model QGSJetII-03 [69]. The dependence of these reference distributions on the shower direction (θ, ϕ) is indicated explicitly. Further details of the SD reconstruction for inclined air showers can be found in [70]. So far, inclined events are only reconstructed with the 1500 m array, an adaption of this reconstruction technique for the 750 m array has not yet been performed.

The 1500 m array was found to be fully efficient for the detection of inclined air showers with energies above 4 EeV. By construction, N_{19} is independent of the zenith angle and can directly be used as an energy estimator of the cosmic ray. It is cross-calibrated using the energy measurement of the FD. The systematic uncertainty of the reconstructed energy ranges between 14 % at 10^{19} eV and 17 % at 10^{20} eV. The cross-calibration revealed that simulations have a deficit of muons at ground compared to the measured data with a similar FD energy [71]. This muon deficit is analyzed further in chapter 7 using hybrid AERA-SD events.

N_{19} can be interpreted as a relative measure of the produced number of muons, N_μ, with respect to the reference simulation. To compare the reconstructed N_{19} to MC prediction Eq. (4.1) is integrated and N_{19} is expressed as a ratio of the total muon number R_μ. For three different sets of MC simulations, each using a different hadronic interaction model, R_μ^{MC} is calculated with respect to the reference N_μ obtained for a 10^{19} eV proton primary with QGSjetII-03, i.e.

$$R_\mu^{\mathrm{MC}} = N_\mu(\mathrm{model}, E, \theta)/N_\mu(\mathrm{QGSjetII\text{-}03}, 10^{19}\,\mathrm{eV}, \theta). \tag{4.2}$$

A comparison of the reconstructed N_{19} and R_μ^{MC} revealed a relative deviation which is within 5 % for events with $R_\mu^{\mathrm{MC}} > 0.6$. The average bias is described with a second order polynomial in R_μ^{MC} [71]. To obtain an unbiased estimator of the muon number, the reconstructed N_{19} is corrected by solving $N_{19}(R_\mu^{\mathrm{MC}}) - N_{19} = 0$ numerically for R_μ^{MC}. The corrected estimator of the muon number is called R_μ in the following.

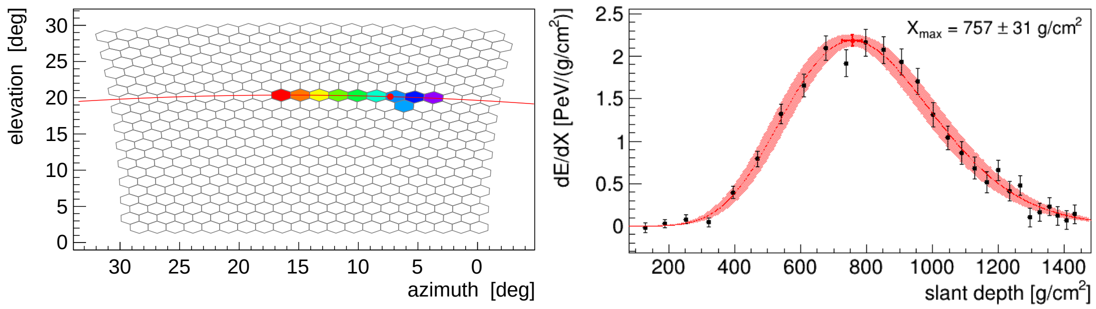

Figure 4.2: Example plots from the event reconstruction of the Fluorescence Detector (Coihueco) extracted from the `EventBrowser` with the SD event ID 32 940 256. The shower direction is reconstructed to a zenith angle of $(70.8 \pm 0.1)^\circ$ and an azimuth of $(238.5 \pm 0.3)^\circ$ with an FD energy of $(1.47 \pm 0.07 \pm 0.08)$ EeV. Light trace measured in the pixel camera of one of the telescopes (left). The color denotes the arrival time of the light in the pixels, from early in violet to late in red. Reconstructed longitudinal shower profile of the energy deposited in the atmosphere (right). X_max is reconstructed by the maximum of the profile.

4.3 FD reconstruction

A complete description of the FD reconstruction can be found in [72] and will briefly be summarized in the following. In this thesis, the FD reconstruction is only performed for measured events that include a reconstructed FD event in addition to the SD and RD events.

The emitted fluorescence light is detected as tracks in the camera pixels of the FD, cf. example event in Fig. 4.2. The geometry of the air shower is reconstructed from the arrival time distribution of the light in the pixels. If the event also contains SD stations, they can be included in the time fit and constrain the geometry reconstruction by a lot due to the large distance between the station and the FD building. The distribution of the light intensity arriving from the different slant depth X of the air shower is fitted with a Gaisser-Hillas function

$$f_\text{GH}(X) = \left(\frac{dE}{dX}\right)_\text{max} \cdot \left(\frac{X - X_0}{X_\text{max} - X_0}\right)^{\frac{X_\text{max}-X_0}{\lambda}} \cdot e^{\frac{X_\text{max}-X_0}{\lambda}} \tag{4.3}$$

to reconstruct the longitudinal shower profile. The shape parameters X_0 and λ can be fixed or fitted depending on the quality of the measured profile. The atmospheric depth of X_max corresponds to the maximum of the longitudinal profile and is a direct fit parameter. The intensity of the light is correlated to the energy deposited in the atmosphere. The integrated shower profile yields an estimation of the *calorimetric shower energy*, i.e. the energy of all particles in the air shower except neutrinos and high-energy muons. The missing *invisible energy* has been derived experimentally [73] such that the calorimetric energy can be converted to the energy of the primary cosmic ray.

4.4 RD reconstruction

The reconstruction of the radio event is discussed in more detail. The trigger to read out AERA data as well as important steps in the reconstruction pipeline, starting with an incoming radio pulse at an antenna position and ending with the reconstruction of high-level air shower observables such as direction and energy, are summarized in the following. In this section the general method is presented for the case of vertical and inclined air showers. Features that are analyzed specifically for inclined air showers within the context of this thesis are discussed in the following chapter.

4.4.1 Radio trigger

Different trigger settings have been implemented for AERA. The performance of a self-trigger [74] depends strongly on the noise conditions at the site of the experiment. Nowadays, most analyses use radio data that is read out by an external trigger of the SD or FD. In the case of an external SD trigger the radio data is only read out if the closest ground distance between an AERA station and an SD station with a local (particle) trigger is smaller than 5 km.

For vertical air showers this distance is likely too big which leads to a low purity of the recorded data. Only ∼10 out of ∼8000 triggered events per day are air shower events that have a radio signal reconstructed with $\overline{\text{Off}}\underline{\text{line}}$. At the same time the distance is likely too small for inclined air showers. Especially at a high inclination and low energy, the area that is illuminated by the radio emission can be significantly larger than the size of the particle footprint on ground [75]. A measured example event for this is shown in Fig. 4.3. The SD reconstruction yields an energy estimation of 2.9 EeV and an inclination of more than 82°. The radio event matches the expectation of a typical radio event, such as the shape and amplitude of the detected pulses, the distance from the shower axis, and the orientation of the radio signal stations approximately in line with the shower axis. The radio data was only read out due to the two isolated stations at a distance of ∼4.5 km to the closest AERA station.

These findings motivated a study on the potential of optimizing the trigger logic to improve the purity and efficiency of the recorded events [76]. A fast and robust reconstruction model was developed that uses only the position of the triggered SD stations as well as their trigger time. In CDAS, the trigger time is only known with a μs time resolution. To reduce the impact of randomly triggered SD stations the core is determined as the component-wise median of all triggered station positions (the signal strength at each station is not available at this level). The shower direction is estimated from the trigger times of 3 SD stations assuming a plane wavefront model. A shower direction is estimated for every combination of 3 SD stations, the final shower direction is then given by the component-wise median of all shower axes in Cartesian coordinates. The performance of this reconstruction method is evaluated based on the data reconstruction of inclined air showers performed in this thesis, cf. chapter 6, and vertical air showers as analyzed in [77]. A median opening angle of 5° between this „online“ reconstruction and the SD axis as reconstructed by $\overline{\text{Off}}\underline{\text{line}}$ is found.

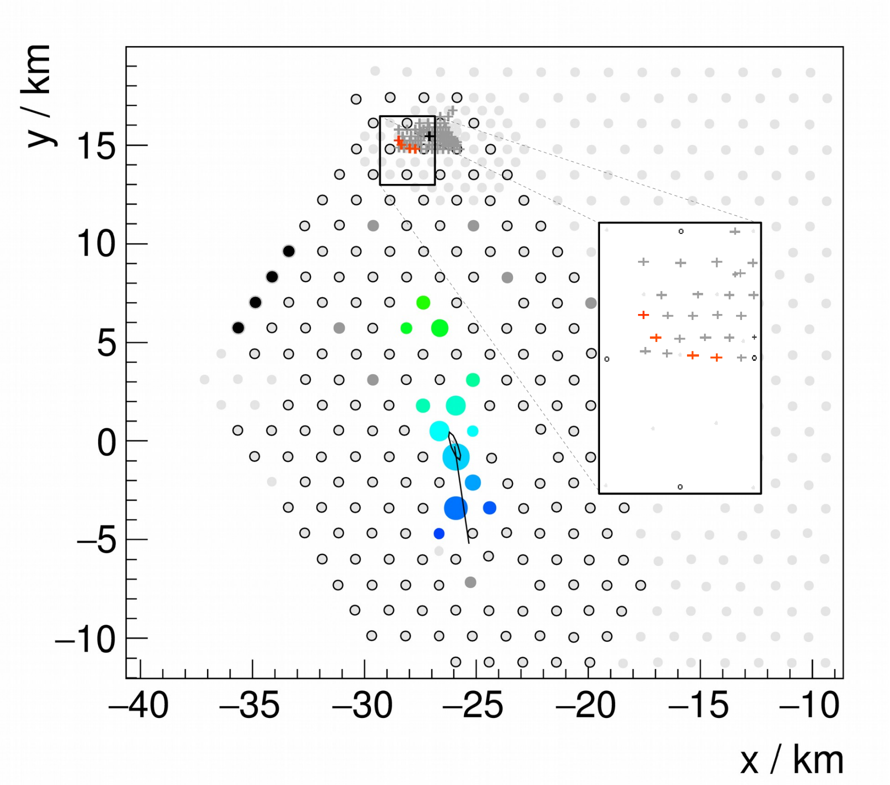

Figure 4.3: Example event where the radio signal extends over an area that is significantly larger than the extension of the particle distribution. The colored circles indicate the measurement of the SD station, where size denotes the deposited energy and color the signal time (blue: early, green: late). Black circles denote stations that had a temporary malfunction. The dark-gray circles denote isolated SD stations that are rejected in the particle reconstruction, light-gray circles indicate sub-threshold stations. The plus markers denote the position of the AERA stations, the inset figure shows a zoom in on the signal stations shown in red color. Figure also published in [75].

The online reconstruction is used to calculate the distance of the AERA stations from the shower axis. The trigger condition of a constant ground distance of less than 5 km is replaced by a zenith-angle dependent distance from the shower axis in the shower plane. Here, the Cherenkov radius is used as an estimator of the typical size of the radio footprint. A rough parametrization of the Cherenkov radius is obtained from simulations of inclined air showers (cf. section 4.5), i.e.

$$r_{\mathrm{Ch}}(\theta) = a \exp{(b\theta)} + c \tag{4.4}$$

with $a = (0.08 \pm 0.05)\,\mathrm{m}$, $b = 6.1 \pm 0.7$ and $c = (110 \pm 40)\,\mathrm{m}$. Strictly speaking, this parametrization was only obtained for inclined air showers and is extrapolated to vertical air showers. With the new trigger condition the AERA data will be read out only if the closest radio station has an axis distance smaller than $5r_{\mathrm{Ch}}$. This evaluated to an axis distance of ~550 m for vertical air showers and up to 3.5 km at an inclination of 80° corresponding to an ellipsis with a semi-major axes of 20.1 km on ground.

This approach triggers on all but 3 of the reconstructed events that were used in the validation. The 3 non-triggered events have been identified as false events where random stations picked up *radio-frequency interference* (RFI) that could be reconstructed. Hence, the method is fully efficient on the validation data sample and reduces the read out of AERA data by ~50 %. In principle the method would also allow triggering only individual stations that are expected to have a radio signal. This could further reduce the amount of data. Extensive validation of the method and its results is needed before the trigger logic can be modified.

4.4.2 Signal reconstruction

The electric-field pulse of an air shower induces a voltage in the antenna which is then amplified and filtered by the analog signal chain and digitized afterwards. The characteristics of the used electronics are stored in a time-dependent detector database. Thus, changes in the hardware are automatically taken into account in the reconstruction. To extract the electric field pulse from the measured voltage trace one has to unfold the antenna response which is described via the *vector effective length* (VEL), $\mathcal{H}$, that depends on the frequency, ν, and the shower direction. In the Fourier space the relation is given by

$$\mathcal{V}(\nu) = \vec{\mathcal{H}}(\nu, \theta, \phi) \cdot \vec{\mathcal{E}}(\nu), \tag{4.5}$$

where $\mathcal{V}$ and $\vec{\mathcal{E}}$ are the Fourier transforms of the voltage and electric field trace, respectively. For a given shower direction the equation can be solved in spherical coordinates with two orthogonal polarized antennas as the electric field has no component in the direction of propagation. This imposes a fundamental challenge as the shower direction already needs to be known for the unfolding of the antenna response. In practice, the SD reconstruction is usually used here. Alternatively, an independent radio reconstruction can be performed with an iterative procedure of antenna unfolding and direction reconstruction until the direction converges.

As an example, the three components of the reconstructed electric-field trace of a cosmic-ray event are shown in Fig. 4.4. The position, i.e. the *signal time*, and amplitude of the pulse are determined by the Hilbert envelope of the electric field trace as the bandpass filtered trace itself can have a zero-crossing at the position of the pulse maximum.

Another important quantity is the *energy fluence* f, i.e. the energy deposit per unit area given in units of $\mathrm{eV/m^2}$, of the incoming radio pulse at each detector station. It is given by the time integral of the absolute value of the Poynting vector over the time window of 200 ns around the signal time subtracted by a noise contribution that is determined in a time window where no signal contribution is expected.

For very strong pulses the station can get saturated, cf. appendix B. This is identified by $\overline{\text{Off}}\underline{\text{line}}$ and the station is rejected in the reconstruction. However, there is potential to optimize the treatment of saturated stations. The signal of a saturated station could be used as a lower limit in the fit of the lateral signal distribution. As the energy fluence is

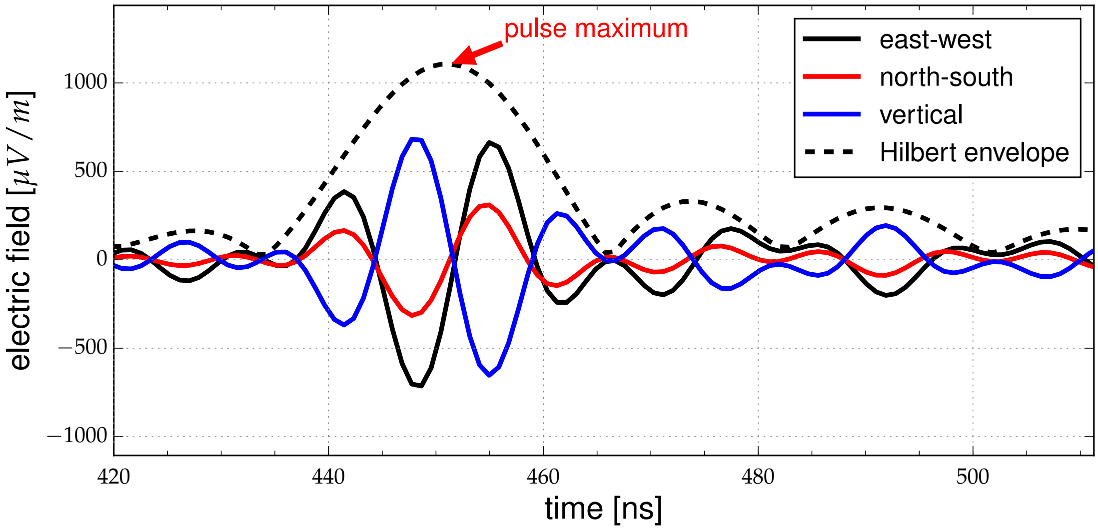

Figure 4.4: Reconstructed electric-field trace of a measured cosmic-ray radio event. An upsampling by a factor of five was applied. The shown Hilbert envelope (dashed line) is the square root of the quadratic sum of the Hilbert envelopes of the three polarization components. Figure from [78].

maximal at the Cherenkov radius and reduces again for smaller axis distances, a saturated station close to the shower axis yields valuable information.

4.4.3 Noise rejection

Although AERA is situated in a rural area, a strong background of pulsed RFI is present. Instead of searching for radio pulses in the whole recorded radio trace with a length of 10 µs, the reconstructed SD geometry is used to define a *signal-search window* around the expected arrival time of each radio station for the identification of the radio signal pulse to mitigate the adverse effects of pulsed RFI. Uncertainties of the reconstructed SD geometry are propagated to the width of the signal-search window, its typical size amounts to ∼1000 ns. For this window size the probability to pick up an RFI pulse is determined as ∼1.5 % which means that typically one or two noise stations are included in the radio reconstruction if all 154 AERA stations are read out.

Several methods have been developed to identify and remove noise stations during the event reconstruction [79, 80]. In the following, I will briefly summarize the methods especially in the context of inclined air showers.

(i) **Pulse shape** Radio pulses from air showers have a characteristic shape and width that can be utilized to distinguish a noise pulse and a signal pulse.

(ii) **Signal polarization** Due to the superposition of geomagnetic and charge-excess emission the polarization of signal pulses has a characteristic pattern in the shower plane when rotated to an $\vec{v} \times \vec{B}$ - $\vec{v} \times (\vec{v} \times \vec{B})$ coordinate system. By using the geometry of the reconstructed SD event, an expected polarization can be calculated for each station. If the measured pulse polarization deviates too much from the expected polarization the pulse is considered as noise. As the false rejection rate increases with zenith angle [80] the polarization rejection is not used for inclined air showers.

(iii) **Station clustering** The radio emission of an air shower illuminates a circular area around the shower axis in the shower plane. Isolated stations far away from the other radio stations are therefore likely to be noise stations. This method looks at two quantities: First, *lonely signal stations*, i.e. stations which have no other signal stations within a distance of 400 m and not more than one signal station within 800 m, are rejected. These numbers have been optimized for AERA24 and AERA124. For AERA153 the stations are deployed on a grid with a spacing of 750 m. By definition these stations will always be lonely, hence this rejection of lonely stations is not usable for analyses of AERA153 data, i.e. analyses of inclined air showers.

The lonely station rejection would not reject a separated cluster of noise stations far away from the signal stations. Therefore, in a second step the distance of the radio stations from the reconstructed SD axis is calculated. In case a jump of more than 500 m in axis distance is found all stations beyond this jump are rejected.

(iv) **Signal time** A noise station will likely have a signal arrival time that is incompatible with the expectation of a signal pulse. In an iterative procedure, starting with the stations closest to the SD core, an additional station is added to the fit of the shower direction until all signal stations are taken into account. If the newly added pulse time does not match the arrival time of the other stations, i.e. it decreases the χ^2 probability of the fit below 5 %, the station is rejected as noise. This selection is sensitive to the wavefront of the radio emission. In [80] an additional time uncertainty was introduced to compensate the wrong assumption of a plane wave (cf. section 4.4.4). The performance of this selection for inclined air showers is analyzed further in section 5.5.4.

By combining all methods, a true rejection rate of 92 % is found for vertical and inclined air showers. The false rejection rate increases from 1.5 % for vertical air showers to 2.6 % in case of inclined air showers [80]. However, these numbers do not include the discussed changes such as the deactivation of the polarization rejection and the lonely station rejection. The presented noise rejection methods show no significant difference for proton and iron primaries, i.e. no composition-dependent selection bias is introduced. Applied to measured AERA data the methods increase the purity of the data set and e.g. improve the fit quality of the lateral signal distribution.

4.4.4 Directional reconstruction

The incoming direction of the air shower can be reconstructed from the arrival time of the radio pulse measured by individual radio stations using an assumption on the shape

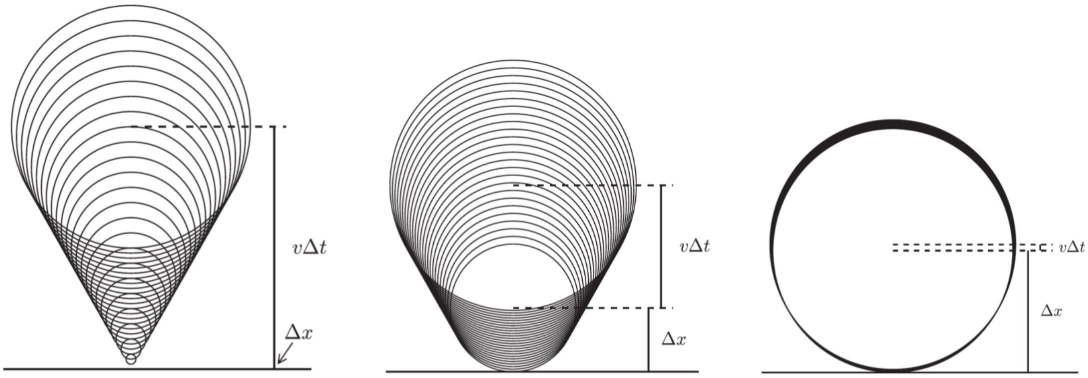

Figure 4.5: Toy model of the radio-wavefront shape. Depending on the sizes of the emission region, $\Delta l = v\Delta t$, and the distance to the observer, Δx, the elementary waves generate a conical wavefront (left), a hyperbolic wavefront (center) or a spherical wavefront (right). Figure from [81].

of the radio wavefront. The true shape of the wavefront depends on the extension of the emission region $\Delta l = v\Delta t$ and its distance Δx from the observer as shown in Fig. 4.5. For vertical air showers with $\Delta x \ll \Delta l$ the wavefront is described best by a conical model. In the case of an emission region far away from the observer, i.e. $\Delta x \gg \Delta l$, the emission region can be seen as a point source which then leads to a spherical wavefront. For an observer at an intermediate distance from the emission region the wavefront is described best by a hyperbola. Indeed, measurements of LOFAR [81] and LOPES [82] have confirmed the hyperbolic shape of the radio wavefront for air showers with zenith angles smaller than 60°[2] and 45°, respectively.

In AERA, only a simple plane wavefront is used for the reconstruction of vertical and inclined air showers so far. For vertical air showers the radio footprint is small such that the difference between the predicted arrival times of the wavefront models is typically negligible given the time uncertainty of AERA stations. Also the station multiplicity might not allow fitting the additional parameters of more complex wavefront models than a plane wave. Furthermore, more complex wavefront models depend on the shower core position, which is e.g. estimated by the SD, but contains relatively large uncertainties. For practical applications the plane wave often yields a sufficient reconstruction of the arrival direction as it is mostly used as a consistency check of the measured radio pulses and the SD reconstruction.

However, the size of the radio footprint, as well as the station multiplicity, increases vastly for inclined air showers. Especially at larger axis distances the predicted arrival times differ significantly for different wavefront models. A more complex wavefront model can therefore improve the accuracy of the directional reconstruction significantly. In section 5.5 the different wavefront models will be compared for inclined air showers with a zenith angle above 60°.

---

[2] Except for one event with a zenith angle of almost 70°.

4.4.5 Energy reconstruction

The energy reconstruction of AERA uses a different approach compared to the SD. Due to the strong asymmetries in the radio signal distribution it is not feasible to use the signal at some reference distance to the shower axis as an energy estimator, cf. $S(1000)$ in section 4.2. Instead, the integrated *radiation energy* E_{rad}, the energy radiated in the form of radio signals, is used as an estimator of the cosmic-ray energy [78, 83]. In general, a two-dimensional model of the lateral signal distribution is fitted to the measured energy fluence of each antenna and then integrated over the whole footprint. Different *lateral distribution functions* (LDF) are already used in AERA for the reconstruction of vertical air showers. The models and their possible application to inclined air showers are discussed in the following.

In a first approach an empirical LDF was developed that is purely based on shape considerations [84]. This *double Gaussian LDF* consists of two two-dimensional Gaussian functions that have a shifted center with respect to each other. In $\overline{\text{Off}}\underline{\text{line}}$, it is implemented in the module `Rd2dLDFFitter`. One Gaussian describes the general shape of the radio footprint at larger distances from the shower core. Closer to the shower core a second Gaussian is subtracted to model the interference of geomagnetic and charge-excess emission. Using CoREAS simulations the LDF can be parameterized in the shower plane as

$$f(\vec{r}) = A\left[\exp\left(\frac{-(\vec{r}+C_1\vec{e}_{\vec{v}\times\vec{B}}-\vec{r}_{\mathrm{core}})^2}{\sigma^2}\right) - C_0\exp\left(\frac{-(\vec{r}+C_2\vec{e}_{\vec{v}\times\vec{B}}-\vec{r}_{\mathrm{core}})^2}{(C_3 e^{C_4\sigma})^2}\right)\right]. \quad (4.6)$$

Here, $f(\vec{r})$ denotes the energy fluence for an antenna at a position $\vec{r}$ and C_0 to C_4 are constants that are derived from CoREAS simulations. The amplitude A, the slope parameter σ, and the core position $\vec{r}_{\mathrm{core}}$ are fit parameters.

With this LDF the energy of cosmic rays was successfully estimated in the case of vertical air showers, cf. [78, 83]. However, the constants C_0 to C_4 were only derived up to a 60° zenith angle. To apply this LDF also to inclined air showers, a study is performed to derive new values for the constants beyond 60° by taking the early-late asymmetry (cf. section 5.2) into account. For this purpose, Eq. (4.6) is extended with an additional shift in the $\vec{v}\times(\vec{v}\times\vec{B})$ direction, similar to C_1 and C_2, and the amplitudes and sigmas of both Gaussian distributions are fitted independently. A direct fit of this model results in huge amplitudes and uncertainties of each Gaussian function, where only the difference of both matches the absolute scale of the energy fluences. Therefore, the fit procedure is adjusted. In a first step, only the energy fluence of stations beyond the Cherenkov ring is used to fit the overall shape of the LDF ignoring interference effects. Then, inside of the Cherenkov ring, the „missing energy fluence“ due to the interference is fitted with an additional Gaussian function.

An example fit for an air shower with a zenith angle of 70° is shown in Fig. 4.6. The simulated energy fluences are described only poorly with the updated LDF model and the fit quality is getting worse for even more inclined air showers. A small offset of the symmetry center in the $\vec{v}\times(\vec{v}\times\vec{B})$ direction is found. This effect is related to a displacement of the radio symmetry center and the MC impact point, cf. section 5.4. Also the correlation of the sigma-parameters for both Gaussians changes from an exponential

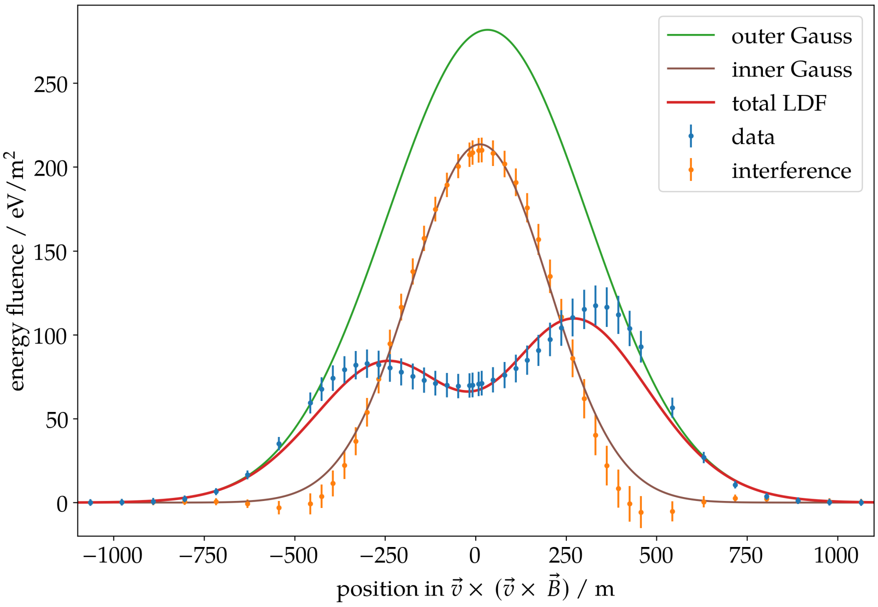

Figure 4.6: Sketch of the fitting procedure of the double Gaussian LDF. Only observers on the $\vec{v} \times (\vec{v} \times \vec{B})$ axis are shown, for the fit the full star-shaped pattern is used. A 10 % relative uncertainty plus an absolute uncertainty of $2\,\mathrm{eV/m^2}$ is shown.

as shown in Eq. (4.6) to a logarithmic function. A strong zenith-angle dependent bias of more than 20 % is found for the reconstructed radiation energy. The model is therefore unsuited for inclined air showers.

In a second approach knowledge about the radio emission and their polarization is used directly to model the geomagnetic and charge-excess emission separately and correctly add the energy fluence values by taking the polarization into account. With this approach the interference is automatically included in the model. This so-called *GeoCe LDF* [85], implemented in the $\overline{\text{Off}}\underline{\text{line}}$ module `RdGeoCeLDFFitter`, is nowadays the default for AERA and used e.g. in the energy scale analysis for vertical air showers [86]. The model was successfully extended for inclined air showers [87], a thorough analysis of the reconstruction performance and efficiency still needs to be performed.

The third LDF aims at extracting the radially symmetric geomagnetic emission from the measured energy fluence which can then be fitted with a one-dimensional function [88, 89]. For a known observer position in the shower plane this can be achieved by utilizing the polarization information. This LDF was especially designed for inclined air showers as the charge-excess is weaker than in vertical air showers. All results obtained in this thesis are derived with a preliminary implementation of this new *HAS LDF* model in the $\overline{\text{Off}}\underline{\text{line}}$ module `RdHASLDFFitter`. At the time of writing this thesis, the version is not finalized yet but it has reached a stable state and shown good performance on simulations made for the AugerPrime Radio Detector.

To obtain a precise energy estimation E_{rad} is corrected for geometry effects [22] as the geomagnetic contribution depends on the geomagnetic angle α and increases with $\sin^2 \alpha$.

For this purpose, the charge excess fraction $a = a(\widetilde{\rho})$ is parameterized as a function of the air density at the shower maximum $\widetilde{\rho}$ and only the geomagnetic part of the radio emission is corrected. In addition, the geomagnetic contribution needs to be corrected for the strength of the local magnetic field. This is ignored here as the magnetic field of the Pierre Auger Observatory is used as the reference magnetic field strength in [22].

A second-order correction of E_rad arises from X_max. The air shower develops according to the slant depth, whereas E_rad increases with the geometric path length of the shower development. For a lower atmospheric density the ratio between the geometric path length and the propagation length measured in atmospheric depth is larger than for higher densities. Hence, an air shower that develops early in the atmosphere has a slightly larger radiation energy than an air shower with the same energy that develops deeper in the atmosphere.

The final form of the *corrected radiation energy* S_rad is then given by

$$S_\text{rad} = \frac{E_\text{rad}}{a(\widetilde{\rho})^2 + (1 - a(\widetilde{\rho})^2)\sin^2\alpha} \cdot \frac{1}{(1 - p_0 + p_0 \exp\left[p_1(\widetilde{\rho} - \langle\widetilde{\rho}\rangle)\right])^2}, \tag{4.7}$$

where $\langle\widetilde{\rho}\rangle$ is the atmospheric density at the shower maximum for an average zenith of 45° and an average $X_\text{max} = 669\,\text{g/cm}^2$. The values of the parameters p_0 and p_1 are given in [22]. For measurements, where X_max is not known or has large uncertainties, the parametrization of a and the second order dependence can be performed using only the reconstructed zenith angle and assuming an average value for X_max. A similar procedure is used for the newly developed LDF model of inclined air showers, cf. [88] for details. It simplifies partially as, by construction, only the geomagnetic radiation energy is estimated. The corrected radiation energy is then used as an estimator for the *electromagnetic energy*, E_EM, of the air shower following a power law:

$$S_\text{rad} = A \cdot \left(\frac{E_\text{EM}}{10\,\text{EeV}}\right)^B \tag{4.8}$$

with $A = 1.408\,\text{GeV}$ and $B = 1.995$ as determined in [88] for the LDF model of inclined air showers[3].

4.5 Simulation dataset

In simulations, the radio emission needs to be calculated for predefined observer locations. Due to interference effects it is not possible to obtain the radio pulse for an arbitrary position, unlike e.g. for particles where the final particle distribution on ground can be sampled for arbitrary station positions. Hence, a simulated radio shower can not be reused by simply throwing it at a different position in the array, as it is done for particle simulations. Simulations can be performed for the real AERA antenna positions and observers on a so-called star-shaped pattern in the ground or shower plane. For real event simulations the shower core has to be known as it is important for the calculation of the antenna positions in CoREAS.

---

[3] No uncertainties of A and B are given in [88].

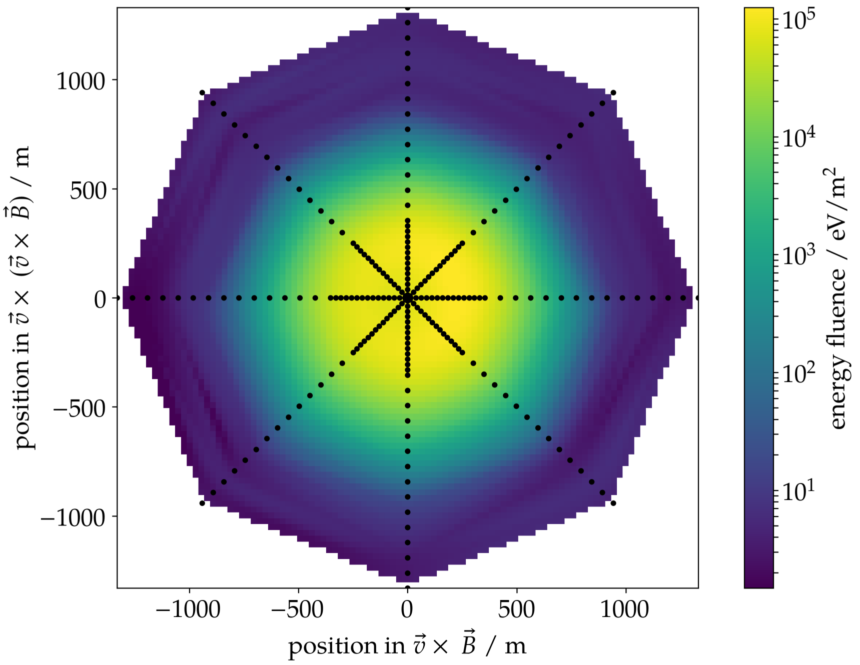

Figure 4.7: Sketch of the simulated observer positions in the shower plane. Each dot indicates the position of a simulated antenna, the spacing is denser near the shower axis up to the Cherenkov radius. In the background an interpolation of the radio footprint of the same simulation is shown. The logarithmic scale of the colorbar suppresses the Cherenkov compression of the radio signal.

For the *star-shaped pattern* the observers are placed on an 8-armed star in the shower plane. Four arms are aligned with the positive and negative $\vec{v} \times \vec{B}$ and $\vec{v} \times (\vec{v} \times \vec{B})$ axis respectively and the other four with their bisections [90]. A parametrization of the expected Cherenkov radius, cf. section 4.4.1, is used and the observers are placed denser nearby the shower axis up to the parameterized Cherenkov radius with an added safety margin[4] and less dense up to a maximum radius [22]. This pattern is sketched in Fig. 4.7. The distances are chosen such that the two-dimensional numerical integration of the radiation energy yields a precise and stable result. For a star-shaped pattern in the ground plane the observer positions are then projected onto the ground. With such a star-shaped pattern on ground the simulated energy fluence values can be used to interpolate the energy fluence at positions where no observer was located [91]. This technique allows reusing radio simulations similarly as it is done for particles by varying the shower core and interpolating the simulated energy fluence for the antenna positions of AERA or the AugerPrime Radio Detector. However, details of this approach are still under investigation.

Simulating the radio emission of inclined air showers is very time consuming as a precise integration of the effective refractive index in the atmosphere becomes crucial. A

---

[4] A combination of an absolute and relative margin was chosen, precisely $1.2 r_{\mathrm{Ch}} + 80\,\mathrm{m}$.

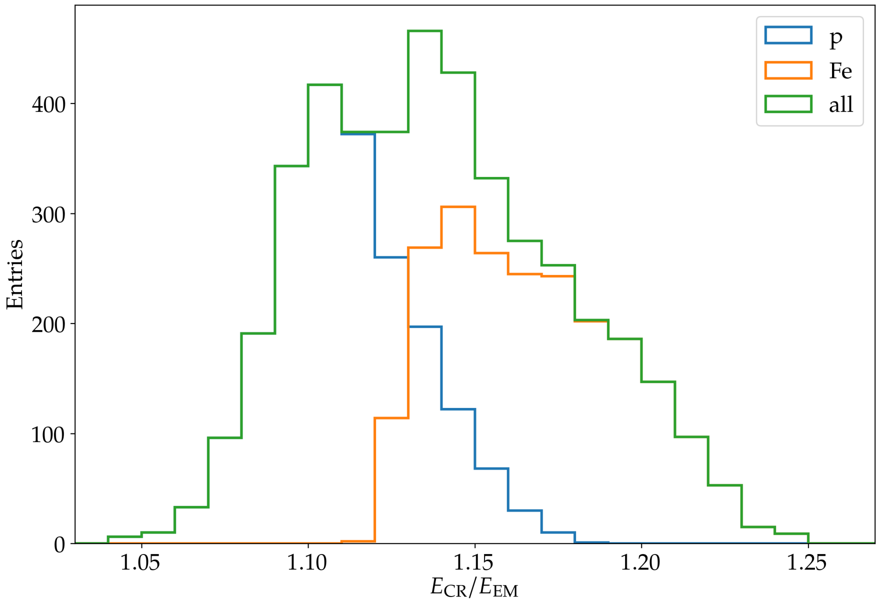

Figure 4.8: Ratio of the primary cosmic-ray energy and the electromagnetic energy obtained with the *RdHasLib*. A histogram is shown for each primary particle individually and for all simulated events.

single simulation of an air shower with an energy of 1 EeV and $\mathcal{O}(100)$ antenna positions can already take up to 2 weeks of CPU time, even if the thinning algorithm of CORSIKA is used. Therefore, one big set of air showers, the so-called *RdHasLib*, is simulated with CoREAS using QGSJetII-04 as hadronic interaction model and observers on a star-shaped pattern on ground. The simulations are uploaded to the iRODS server in Lyon and are available for the collaboration [92]. They will be used throughout this thesis for several different analyses. An example of the used MC input for one simulated air shower is shown in appendix A.

Discrete values are used for energy, zenith, and azimuth angle. The logarithms of the energies are in the range from 18.4 to 20.2 with a stepsize of $\log_{10}(E/\mathrm{eV}) = 0.2$, the zenith angles range from 65° to 85° with a step size of 2.5° and 8 equidistant azimuth angles, i.e. coming from North, North-East, East etc. For each combination 3 proton and 3 iron air showers were simulated to cover shower-to-shower fluctuations. Hence, the total number of simulated showers amounts to 4320. The total computing time exceeds 0.5 Mh, for air showers with a primary energy above 10^{19} eV the MPI parallelization of CORSIKA was used.

With the *RdHasLib* the difference between the energy of the primary particle, E_{CR}, and the energy of the electromagnetic cascade, E_{EM}, is evaluated. For both quantities, the MC truth is used and their typical ratio is shown in Fig. 4.8. For a proton primary the mean(standard deviation) are estimated as 1.11(0.02), for an iron primary as 1.17(0.03), and 1.14(0.04) for the combined data of both primaries. These values will be used later in this thesis to convert between the primary and the electromagnetic energy of an air shower.

4.6 ADST event selection

Parts of this chapter have been published in:

M. Gottowik,
„Extension of the ADST event selection tool for radio“, Internal note of the Pierre Auger Collaboration (2020), GAP 2020-033

The standard ADST event selection tool, `selectADSTEvents` [93], is extended for radio events within the scope of this thesis, cf. [94] for more details. Selection criteria are specified in a text file based on a set of predefined cuts, examples for the event selection are shown in appendix C. The tool has already been used for a long time for a selection of SD or FD events, however, it was limited in functionality for AERA events [95] and therefore hardly used in radio analyses. The list of available cuts, as well as their complexity, has now increased also for radio. Therefore, `selectADSTEvents` should now be the standard for any kind of event selection including radio. Nowadays, its usage is also encouraged by the *Auger analysis archiving policy* [96].

The tool provides cuts to select events based on their reconstructed shower direction as well as the angle to the Earth's magnetic field. Reconstructed radio quantities are usually stored inside of a parameter-storage object on shower and station level. Radio events can be selected based on the values or the uncertainties (relative or absolute) of shower parameters defined in `ShowerRRecDataQuantities`. A similar set of cuts on station level is not yet implemented.

Previously, consistency checks of the radio and particle reconstruction were performed in the `RdEventPostSelector` but have now moved into `selectADSTEvents`. Events can be selected based on the opening angle of the radio and particle shower axis and the axis distance of the radio core from the SD axis. The previous default values of 20° and 2 km have been rather loose. A maximal opening angle of ∼2° and a maximal axis distance of the RD core of ∼750 m are determined in chapter 6 for inclined air showers.

To ensure a proper reconstruction of the radio LDF the reconstructed shower core should be surrounded by signal stations. In SD, a full hexagon around the hottest station is required, which is not feasible for AERA due to the inhomogeneous array layout. Instead, an event is considered *contained* if the reconstructed SD core position, or a part of its uncertainty ellipse, is inside of the convex hull [97] of all externally triggered and non-rejected radio signal stations. Stations that were e.g. not in operation (i.e. due to a temporary malfunctioning or low batteries) or in a bad period [98] are therefore not included in the calculation of the convex hull.

An example event selected by this cut is shown in Fig. 4.9. The reconstructed SD core is shortly outside of the convex hull, but the event is still considered as contained because the SD core uncertainty ellipse is partially inside the convex hull. The core uncertainty for this event is so large as the SD event has only 4 triggered stations. There are further cuts to select events with an SD core inside the area of the individual AERA

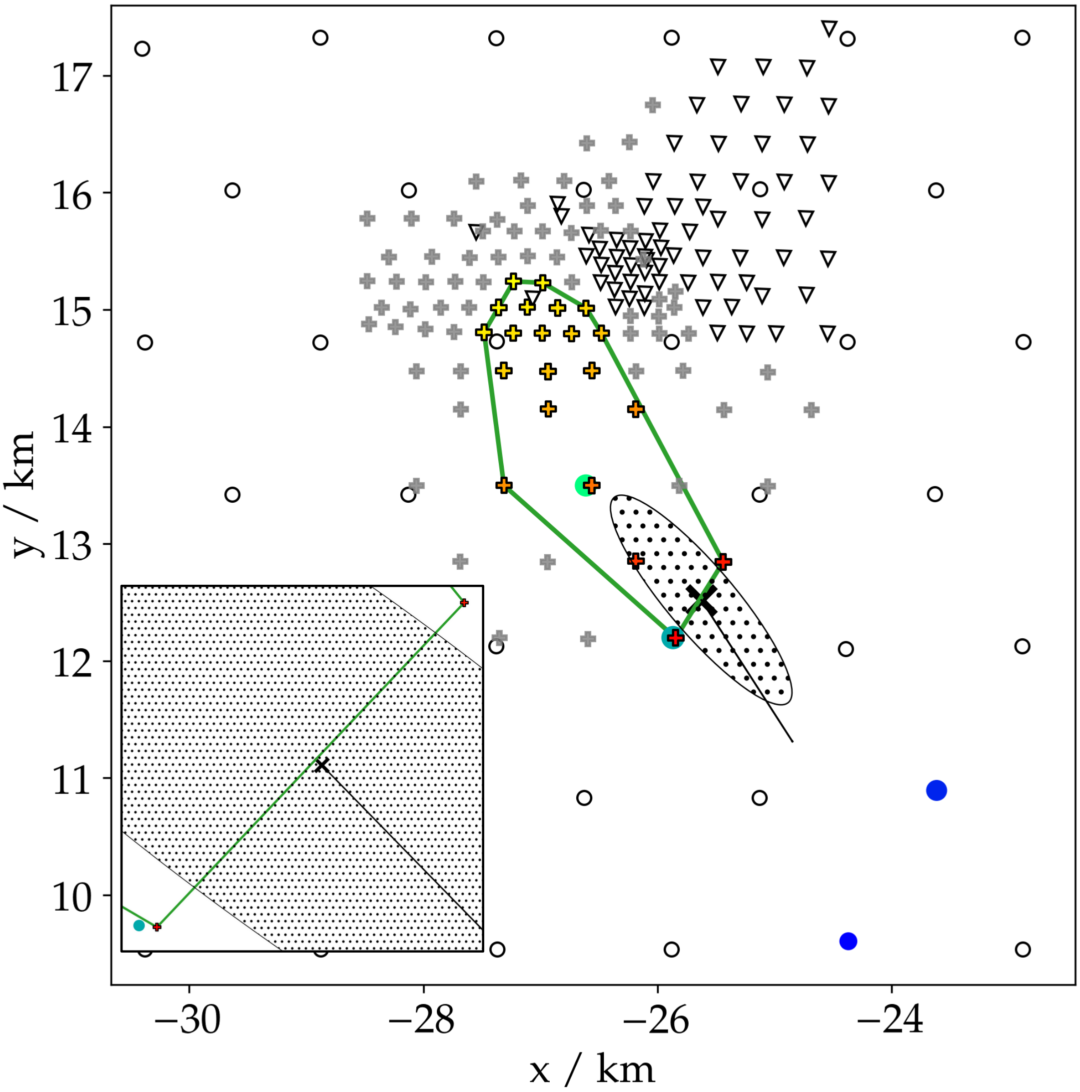

Figure 4.9: Example of a contained event. The colored circles indicate the position of the SD stations, where size denotes the deposited energy and color denotes the signal time (blue: early, green: late). Empty circles indicate non-signal stations. The reconstructed SD core position is indicated by the black cross, its uncertainty ellipse on ground by the hatched area. The plus markers denote the position of the AERA stations, color indicates the signal time (red: early, yellow: late). Sub-threshold radio stations are denoted by gray plus markers. Stations that were not in operation and self-triggered stations which are not used in this analysis are indicated by empty triangles. The green line shows the convex hull of all non-rejected radio signal stations. The inset figure shows a zoom onto the core position.

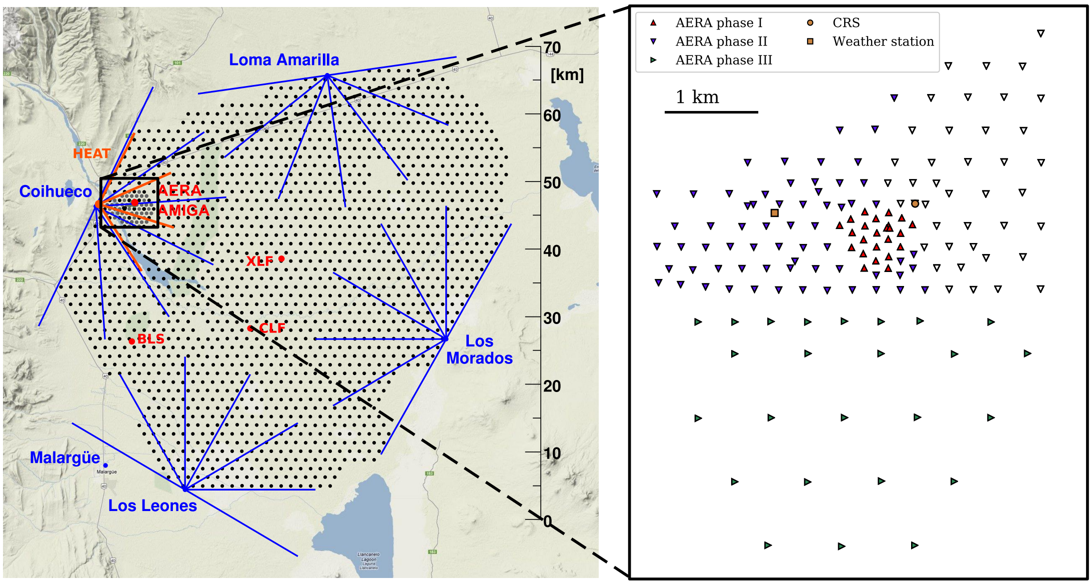

Figure 4.10: Position of the electric field mills. One is located at the CRS (red dot in the left figure), another one was first installed at the BLS and later moved to the weather station inside AERA.

deployment phases. Their boundary polygons are optimized by eye to match the shape of each deployment phase. These cuts can be useful for a cosmic-ray flux estimation as the detection area is constant. In all cuts, the convex hull is calculated using the *Graham scan* algorithm [99]. To test whether the SD core is inside the boundary polygon a ray casting algorithm [100] is used. If the SD core is outside of the boundary polygon the intersection of its uncertainty ellipse with each edge of the polygon is calculated analytically.

Another way of selecting events with a proper reconstruction of the radio LDF is given by the sampling of the LDF. An event that contains signal stations inside and outside of the Cherenkov ring should result in a well-reconstructed radio event as the LDF fit is well constrained by the signal stations. Right now, this cut is tailored to be used only in combination with the `RdHASLDFFitter` module as the Cherenkov radius is calculated analytically using the fitted LDF. A generalization to a model-independent version is straightforward to implement by using a parameterized description of the Cherenkov radius.

Strong atmospheric electric-fields, e.g. due to a thunderstorm (TS), can have a measurable impact on the emitted radiation. It has been shown that the reconstructed RD energy can be amplified by a factor of up to 100 during thunderstorm conditions compared to the SD energy [101]. Therefore, events during thunderstorm periods need to be rejected for standard analyses. Two field mills have been installed inside the SD array to monitor the electric fields in the atmosphere. One is located at the CRS, the other one has been located at the *Balloon Launching Site* (BLS) but was re-deployed as the *AERA weather station* in August 2014. The positions of the field mills are shown in Fig. 4.10. For the identification of thunderstorm conditions BLS data is not used as it is not available for most of the data period and the BLS is 21 km away from the CRS such that found thunderstorm conditions will probably not affect AERA events.

A thunderstorm cloud can induce additional radio emission that does not match the expected polarization of an air shower. In the past, mainly the total energy fluence and not the polarization information was used by the LDF models, e.g. `Rd2dLDFFitter`. Therefore, the reconstructed energies were too high. The current LDF models, i.e. the `RdGeoCeLDFFitter` and the `RdHASLDFFitter`, utilize the polarization information as described in section 4.4.5. A thunderstorm event is therefore less likely to have a good LDF fit in general. However, this does not diminish the need for a detection method of thunderstorm conditions.

Three different methods for the identification of periods with strong atmospheric electric-fields were studied for AERA. The first thunderstorm cut (method $\mathcal{C}$) is based on criteria found in [102] and available as private code [103]. It only uses the field mill at the CRS and evaluates the TS conditions from the time of the event up to 15 min afterwards. A stricter selection was used in a second analysis [104] which was more focused on the detection of lightning (method $\mathcal{L}$). If strong atmospheric electric-fields are found at a time t_0 an interval of $\pm 10\,\mathrm{min}$ around t_0 is flagged as `IsTS` in a database[5]. Finally, a third set of criteria was used in a dedicated analysis of thunderstorm events [101] (method $\mathcal{J}$). The main feature of this selection is an optimized choice of the time interval for the identification of thunderstorm conditions.

As a thunderstorm cloud influences the emission of the radiation it is important to know if the shower propagated through it. There can be a time shift between the detection of the thunderstorm cloud at the field mills and them impacting the radio emission of an air shower. This introduces a potential shift, τ_shift, in the arrival time of the cloud above the field mills of

$$\tau_\mathrm{shift} = \frac{h_\mathrm{cloud}}{v_\mathrm{cloud}} \tan\theta \tag{4.9}$$

with respect to the event time. As neither the height nor the velocity of clouds are measured at the AERA site average values of $h_\mathrm{cloud} = 5\,\mathrm{km}$ and $v_\mathrm{cloud} = 50\,\mathrm{km/h}$ are used in the calculation. The electric-field measurements inside an interval of $\Delta t = 30\,\mathrm{s}$ around $\pm\tau_\mathrm{shift}$ are used for the identification of thunderstorm conditions. This check is only sensitive to thunderstorm clouds in a ring of a certain width, centered at the field mill and a radius that increases with the zenith angle of the air shower. For a more precise estimation the position of the thunderstorm cloud on ground needs to be measured. For each field mill it is checked individually if the measured electric field ε indicates strong atmospheric electric-field conditions, i.e.

$$|\varepsilon| \geq 100\,\mathrm{V/m} \quad \text{or} \quad \sigma_\varepsilon \geq 20\,\mathrm{V/m}. \tag{4.10}$$

All three methods are based on the assumption that a thunderstorm cloud will propagate over the field mills. This may be true for vertical air showers as they develop close to AERA. For inclined air showers the distance to X_max can increase up to 150 km for

---

[5] Accessible via `paomondb.physik.uni-wuppertal.de`, the values are stored in the `IsTS` fields of `AERA.Field` (CRS) and `AERA.FieldAERAWS` (AERA weather station).

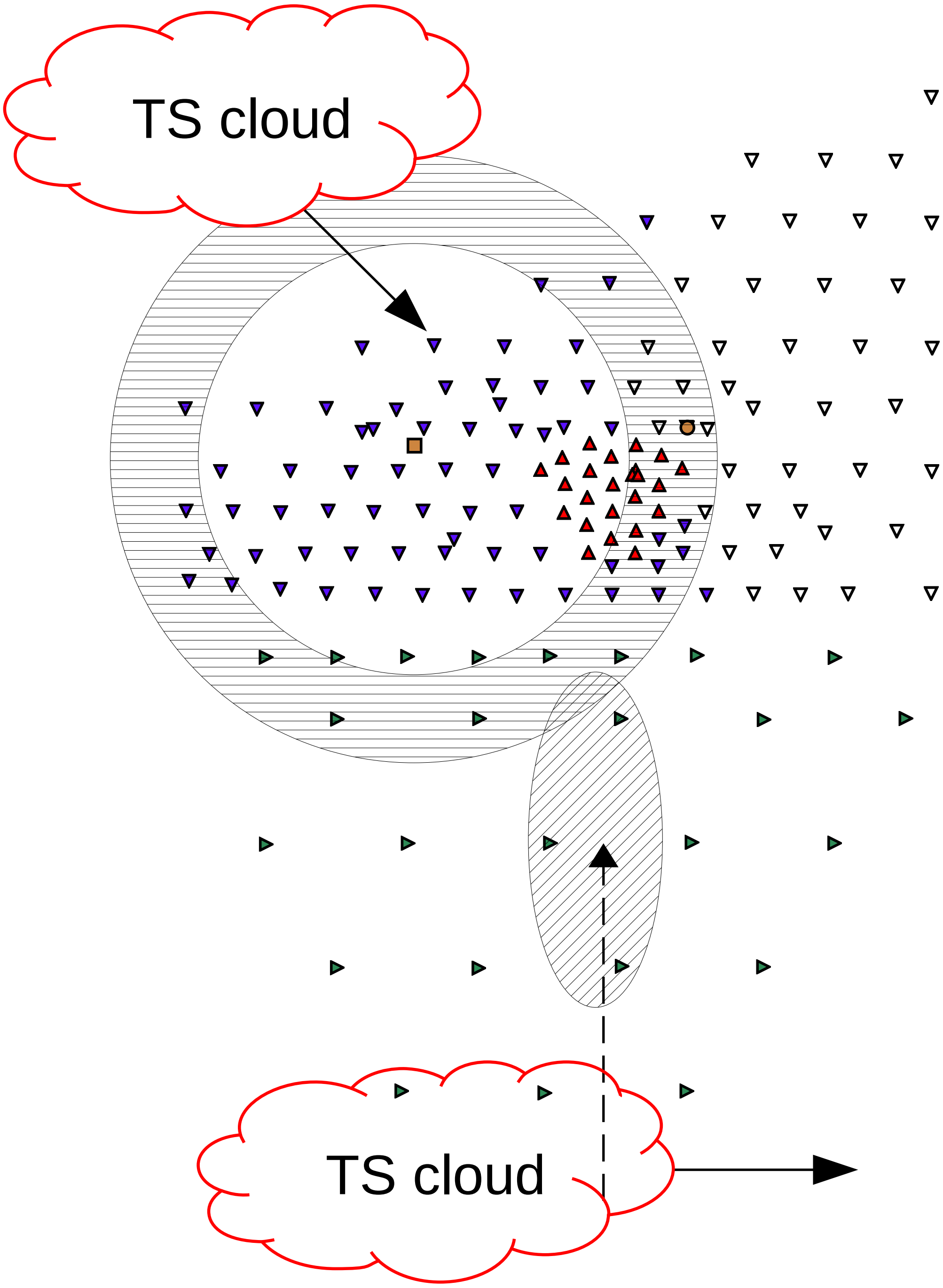

Figure 4.11: Sketch of the used method to identify events during thunderstorm conditions. The ring centered at the AERA weather station indicates the region where thunderstorm clouds are identified. An air shower is coming from South (dashed arrow), the radio footprint on ground is indicated by the hatched ellipse. Two independent thunderstorm clouds are shown, their direction of propagation is indicated by the arrows. Dimensions not to scale.

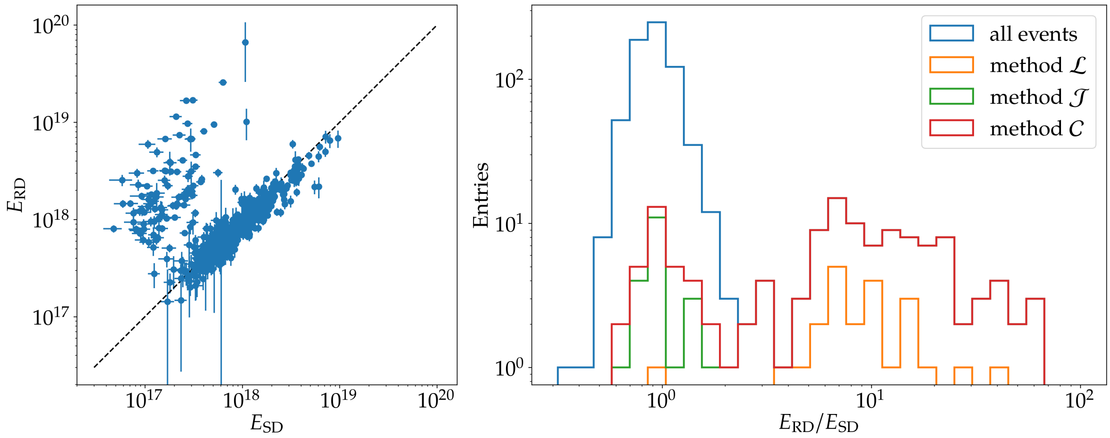

Figure 4.12: Distribution of reconstructed energies with SD and RD (left). The dashed line indicates identity. Events with a much larger RD energy are assumed to be within thunderstorm periods. Histogram of the ratio of RD and SD energy (right). Shown is the distribution of all events as well as the events that are identified as thunderstorm events by the three different methods. The blue, red and green histograms are identical for $E_{\mathrm{RD}}/E_{\mathrm{SD}} > 2.5$.

an inclination of 85°. Hence, there is an inevitable amount of false identification as the position and direction of thunderstorm clouds are not known. The limitations are visualized in Fig. 4.11 especially for method $\mathcal{J}$, but the principle still holds for the other two methods. The cloud in the North will reject the measured event as a thunderstorm event even though it could not have impacted the radio event that is coming from the South. However, the thunderstorm cloud in the South may have an impact on the air shower but does not move towards AERA and is therefore not detected.

In the following, the three methods are compared based on the data reconstruction of [77]. The data set contains 768 vertical air showers up to a zenith angle of 55° with an opening angle between the SD and RD axis below 10° where the RD energy is estimated by the `Rd2dLDFFitter`. In Fig. 4.12 the correlation of SD and RD energy as well as their ratio is shown. The ratio distribution shows a strong peak centered at unity and a second distribution of events where the RD energy is up to 100 times bigger than the SD energy. This is the typical distribution that is expected from thunderstorm events [101].

The distribution of the ratio of both energies that are inside the found thunderstorm conditions of the three methods is shown for comparison. Events without data from the field mills are not shown here. Method $\mathcal{L}$ rejects the lowest number of events but does also not detect most of the events that are in the thunderstorm region of the distribution. With the methods $\mathcal{C}$ and $\mathcal{J}$ all events in the thunderstorm region are identified as events during thunderstorm conditions, but method $\mathcal{C}$ rejects ten good events more than method $\mathcal{J}$. The smallest ratio of good events being rejected as inside thunderstorm conditions is obtained by method $\mathcal{J}$ with only $\sim$3.5 %. For a fair comparison with method $\mathcal{C}$ only the CRS data was used in method $\mathcal{J}$. By including the AERA weather station the number of events without measurements of the atmospheric electric-field reduces from 216 to

Table 4.1: Summary of the definition of the individual bits of the rejection status flag of the `REvent` and where the bits are set inside of Offline.

Bitflag	reason	filled by
0	`eEventManuallyRejected`	unused
1	`e2DLDFsigmaatlimit`	`Rd2dLDFFitter`
2	`e2DLDFvariationfails`	
3	`e2DLDFmeanAdistoutside`	
4	`e2DLDFmeanSigmadistoutside`	
5	`e2DLDFasymmetryAdist`	
6	`e2DLDFasymmetrySigmadist`	
7	`e2DLDFFitfailed`	
8	`eCRSNoData`	`getRadioTsFlag.py`
9	`eCRSTsConditions`	
10	`eAERAWSNoData`	
11	`eAERAWSTsConditions`	

122. In case that both field mills were taking data the results can be combined with a logical AND or a logical OR. Using the logical AND method $\mathcal{J}$ still rejects four events less than method $\mathcal{C}$, with the logical OR five events more than with method $\mathcal{C}$ are identified as thunderstorm events. Method $\mathcal{C}$ can be adapted to also include the AERA weather station, however, this results in a bigger number of falsely identified thunderstorm events. Therefore, method $\mathcal{J}$ was chosen as the standard thunderstorm identification method for the whole AERA group.

By design, ADST is not allowed to have a dependency on MySQL or SQLite, hence, it is not allowed to directly query the database inside ADST. The information can be obtained during the Offline reconstruction and exported into the ADST file. This approach has two disadvantages: first, if Offline is run in an isolated cluster environment it may not have access to the database server or the database queries create CPU-downtime that is not desired on a cluster; second, this can only be used with a new data reconstruction, even though the information is available independently of the Offline revision. Therefore, an alternative solution is used where the information about thunderstorm conditions is written into an existing ADST file, similar to the procedure for the SD weather correction [105], which can also be applied to old ADST files. With the script `getRadioTsFlag.py` located in the `Tools/RadioTsFlag` directory of Offline the raw information which field mill was taking data and if thunderstorm conditions are identified is extracted from the AERA database and written into the rejection status of the `REvent`.

The different reasons to reject an event are encoded in the bit pattern of an integer variable, the meaning of the individual bits is shown in Tab. 4.1. The bits 1 to 7 are used by the `Rd2dLDFFitter` to indicate a bad LDF fit. This is vastly deprecated as the `Rd2dLDFFitter` is hardly used anymore. The bits are kept for backward-compatibility. The thunderstorm information is filled into the bits 8 to 11.

The individual rejection reasons are combined into a thunderstorm decision with a cut implemented in `selectADSTEvents`. The strictness of the cut is specified by two arguments:

1. The number of data-taking field mills that are needed to identify thunderstorm conditions. The number can be within 0 and 2. If it is set to 0, events where both mills were not in operation will be flagged as thunderstorm events, otherwise 1 (or 2) field mills with data are required to determine thunderstorm conditions.
2. In case that both field mills were taking data their individual result of found thunderstorm conditions are combined with a logical AND (1) or a logical OR (0).

The anti-cut "`!thunderstorm 0 0`" provides the purest thunderstorm-free dataset. Events without field mill data are treated as potential thunderstorm events. If both field mills have taken data an event is rejected as a thunderstorm event if at least one field mill identified thunderstorm conditions. A very clean selection of thunderstorm events is obtained by "`thunderstorm 2 1`". Both field mills need to have taken data and both have to identify thunderstorm conditions to treat the event as a thunderstorm event.

This new implementation of the thunderstorm cut is a significant improvement compared to the previous situation for two reasons. First, the code to identify thunderstorm conditions is now an integral part of $\overline{\text{Off}}\underline{\text{line}}$ and under version control. Second, the information is written into the ADST file. Therefore, the flags are displayed in the `EventBrowser` and standardized ADST cuts are available. This simplifies the usability of the rejection of thunderstorm events enormously.

5 Relevance and Special Challenges of Inclined Air Showers

Air showers with zenith angles larger than 60° are called *inclined air showers* or *horizontal air showers* (HAS). They propagate up to 36 times longer in the atmosphere compared to a vertical air shower which leads to some specific features in the radio emission. In this chapter an early-late asymmetry in the radio footprint, a displacement of the radio core, and the shape of the radio wavefront will be discussed. The impact of these features is analyzed on a small subset of the recorded AERA data where needed. A full analysis of inclined air showers measured with AERA is presented in the following chapter. Further, the scientific relevance of inclined air showers is demonstrated in two examples: a search for air showers induced by a neutrino and a composition estimation of the air shower.

5.1 Size of the radio footprint

In general, the radio emission is strongly forward-beamed into a cone of a few degrees opening angle [23]. For vertical air showers it only illuminates areas on ground with a diameter of ~100 m. The size of the radio footprint increases for inclined air showers for two reasons. First, the air shower develops geometrically more distant to the ground which increases the size of the radio cone in the shower plane. Second, the projection of

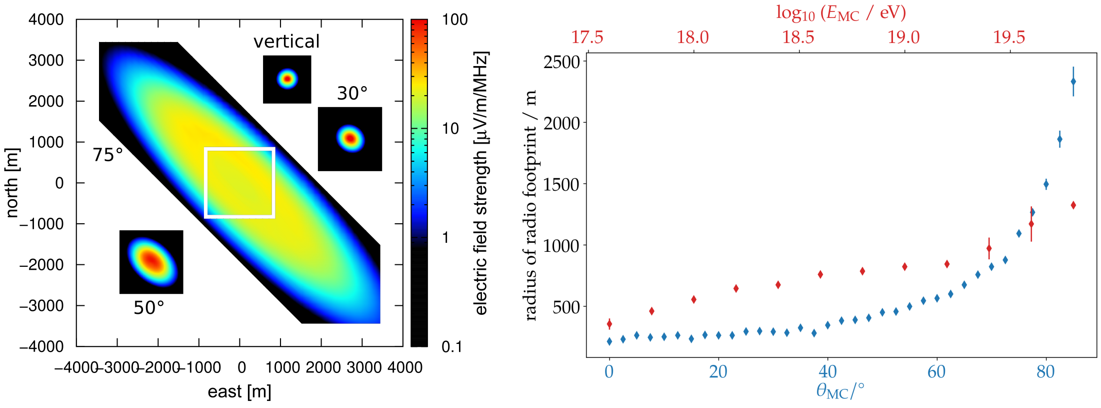

Figure 5.1: Size of the radio footprint of EAS simulated with CoREAS for a fixed primary energy of 5 EeV and four different zenith angles (left). The white rectangle denotes the size of the inset figures. Figure from [23]. Radius of the radio footprint in the shower plane as a function of energy (upper x-axis) for a fixed zenith angle of 65° and as a function of zenith angle (lower x-axis) for a fixed energy of $10^{18.4}$ eV (right).

the circular footprint in the shower plane onto the ground results in an elliptic footprint with an area of dozens of square kilometers. The predicted footprint of four CoREAS simulations with different zenith angles is shown in Fig. 5.1 (left).

For a more quantitative estimation of the footprint size the simulations of the *RdHasLib*, as well as an extension for lower energies and zenith angles, are analyzed. The early-late corrections (cf. section 5.2) are applied for the projection of the simulated antenna positions from the ground plane into the shower plane. The axis distance where the interpolated energy fluence drops below a threshold of $2\,\mathrm{eV/m^2}$ is calculated for each arm of the star-shaped grid, the mean is used as the radius and the spread as an estimator of its uncertainty. In Fig. 5.1 (right) the radii are shown for two different setups. First, for air showers with a fixed energy of $10^{18.4}\,\mathrm{eV}$ coming from South at varying zenith angles (blue points); and in addition for air showers with a fixed zenith angle of 65° coming from South and varying energies (red points). The radius increases significantly from 200 m to more than 2200 m for more inclined air showers with the same energy. This is much stronger than the increase with energy. For a 65° zenith angle the radius increases only from 350 m to 1300 m for more than two decades in energy.

The default star-shape pattern is optimized for a stable integral but here a constant minimum signal has to be reached. For the highest energies the simulated energy fluence values do not drop below the threshold for some or all arms anymore and therefore the radius cannot be estimated by that approach or only with large uncertainties. For this study, the MC core and axis were used. For the most inclined air showers the radio LDF is shifted with respect to the MC core (cf. section 5.4) which causes larger uncertainties on the radius.

5.2 Early-late asymmetry

The two-dimensional distribution of the radio emission of an air shower is affected by a strong asymmetry arising from the superposition of geomagnetic and charge-excess emission. For inclined air showers an additional *early-late asymmetry* disturbs the signal distribution further [106]. The propagation length of the emission above the shower axis can be much bigger compared to an emission below the shower axis. Even for simulations in the shower plane, where the geometrical distance is symmetric, the effect is still visible as the emission below the shower axis propagates through a denser atmosphere than the emission above the shower axis, which corresponds to a longer slant depth.

This effect is purely coming from geometric considerations and can be corrected to first order by assuming a point source of the radio emission at X_{max} with a geometric distance R_0 from the shower core. When projecting an antenna into the shower plane it needs to be shifted along the line of sight from its position in the ground plane to the hypothetical point source as shown in Fig. 5.2. This results in a modified radial axis distance r in the shower plane compared to the lateral distance r_{raw} in the ground plane. This projection is equivalent to describing the lateral distribution pattern in terms of off-axis angles instead of axis distances. Furthermore, the measured energy fluence needs to be adapted to the changing distance between antenna position and source location.

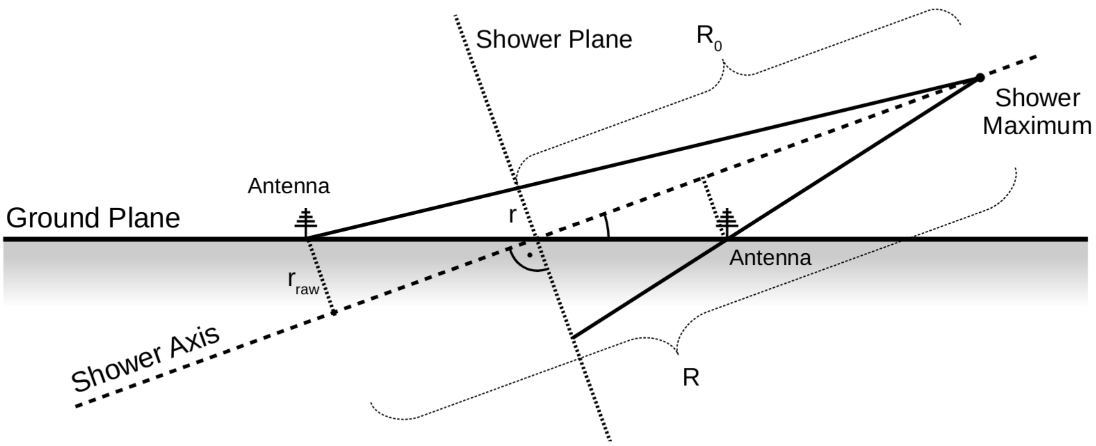

Figure 5.2: Sketch of the early-late correction assuming a point source at $X_{\max}$ as the origin of the radio emission. Figure from [106].

The corrections can be written as:

$$f = f_{\text{raw}} \cdot \left(\frac{R}{R_0}\right)^2, \qquad r = r_{\text{raw}} \cdot \frac{R_0}{R}, \tag{5.1}$$

where R is the geometrical distance from the source to the plane orthogonal to the shower axis and containing the antenna position on ground.

In a dedicated study observers on the ground as well as their corresponding position in the shower plane after applying the early-late correction using the true MC $X_{\max}$ were simulated. A comparison showed that the corrected energy fluence of the ground observers reproduces the corresponding ones in the shower plane within 2 % for most axis distances. Only for small signals at large axis distances a bigger deviation was found [88].

In measurements $X_{\max}$ is unknown. However, a correction of the early-late asymmetry can be included in the LDF fit without further requirements on the event as all current LDF models depend on the distance to $X_{\max}$. In the fit of the LDF of inclined air showers, cf. `RdHASLDFFitter` in section 4.4.5, that is used in this thesis a correction of the early-late asymmetry is automatically taken into account.

5.3 Scientific potential

Measurements of inclined air showers using radio arrays have great scientific potential, cf. [59, 60]. The electromagnetic and hadronic component of the air shower are absorbed in the atmosphere and only the muonic component reaches the ground (cf. Fig. 5.3). However, a radio detector can perform a direct measurement of the electromagnetic energy of the air shower. Thus, by a hybrid detection of the radio emission and the particles on ground the mass of the primary particle can potentially be derived on an event level. This approach will be followed in chapter 7.

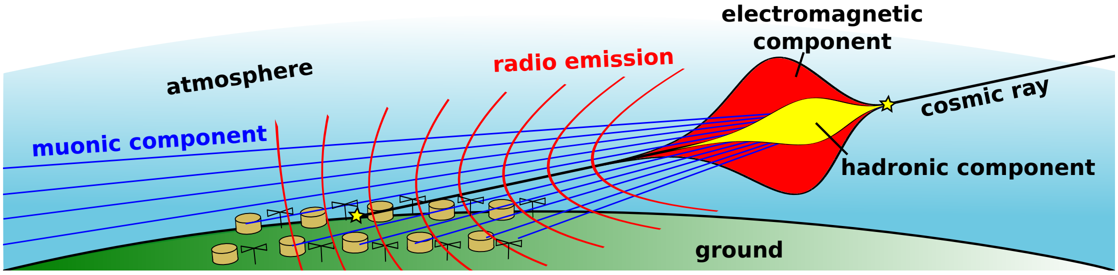

Figure 5.3: Sketch of an inclined air shower. For the radio emission the typical shape of the wavefront is shown, starting with an hyperbola close to the emission region and evolving to a spherical wave front at larger distances. Figure from [7].

Another interesting science case is the search for neutrino-induced air showers with inclined air showers. An unambiguous classification of air showers into so-called *old* (hadronic) and *young* (neutrino) ones is needed. Hadronic primaries will interact shortly after entering the Earth's atmosphere and the air shower can develop completely. The electromagnetic and hadronic component will be absorbed in the atmosphere and the showerfront of the particles at ground will be muon dominated. A neutrino can initiate an air shower quite deep in the atmosphere and the shower will still have a strong electromagnetic component at the ground. Both types of air showers produce different types of signals in the SD stations that can be used to identify events induced by a neutrino primary. So far, no neutrino-induced air shower has been observed with the Pierre Auger Observatory [107].

The radio detection can provide valuable information for the search of neutrino-induced air showers as the shape of the wavefront (cf. Fig. 5.3) as well as the LDF depends on the distance to the emission region as shown in Fig. 5.4. As an example, an electron-neutrino primary with an energy of $10^{18.8}$ eV and a zenith angle of 85° coming from South is simulated several times. Due to the small interaction cross-section of neutrinos the desired vertical height above sea level of the first interaction has to be set as a parameter. Showers with a first interaction at a height from 2 km to 75 km were simulated, the observation height is set to 1.4 km above sea level. The energy fluence on the positive $\vec{v} \times (\vec{v} \times \vec{B})$ axis is shown as a function of the MC axis distance. No early-late correction was applied as the underlying assumption of a point source being far away from the observer is not fulfilled for all first interaction heights. The data points are interpolated to highlight the change in the shape of the LDF, the oscillation for low axis distance in the case of a first interaction of 2 km is an artifact of the used interpolation.

For nearby air showers the radio footprint will be small and a radio detection is unlikely. With an increasing distance to the point of first interaction the air shower can develop over a longer distance before it reaches the detector and hence has a broader footprint. According to the idea of shower universality the LDF becomes indistinguishable for hadronic and neutrino primaries if the point of first interaction is close. For $10^{18.8}$ eV the LDF of a proton or an iron primary looks almost similar to the LDF of a neutrino primary with a height of first interaction of 25 km. Combining the particle and radio

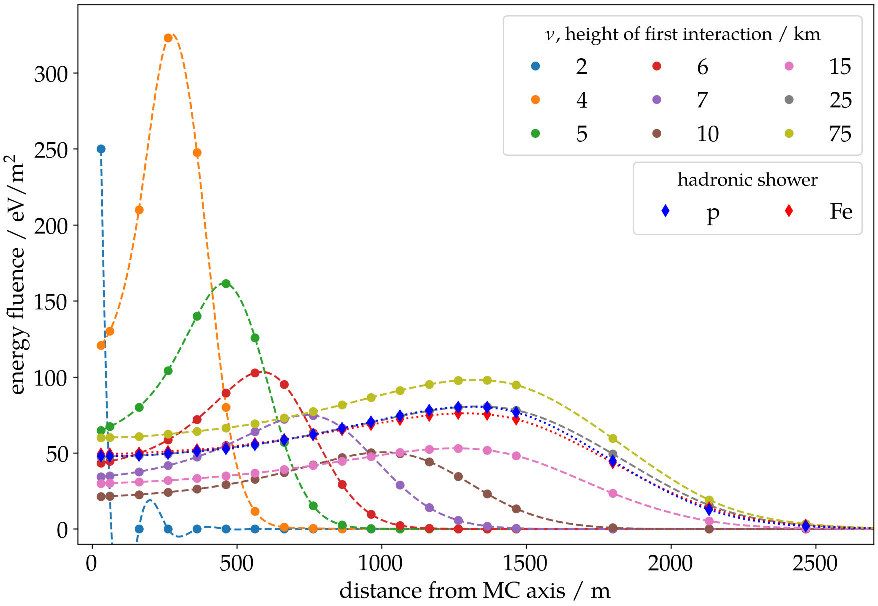

Figure 5.4: Lateral distribution of the radio signal on the positive $\vec{v} \times (\vec{v} \times \vec{B})$ axis for simulated neutrino showers with different heights of the first interaction. The LDF of a proton and an iron simulation is added for comparison. The simulated energy fluence is interpolated for convenience. The oscillating behavior in the LDF of the 2 km height of first interaction neutrino simulation is an artifact of the cubic interpolation.

measurements can significantly improve the search for neutrino-induced air showers. An air shower with a strong signal of the electromagnetic component in the SD and a small radio footprint, or no detected radio signal at all, would indicate a neutrino primary. If the radio event shows a big footprint a neutrino primary is disfavored.

5.4 Refractive displacement of the radio-emission footprint

Parts of this chapter have been published in:

F. Schlüter, M. Gottowik, T. Huege and J. Rautenberg,
„Refractive displacement of the radio-emission footprint of inclined air showers simulated with CoREAS“, Eur. Phys. J. C 80.7 (2020)

Correcting the early-late asymmetry in CoREAS simulations of very inclined air showers revealed an additional apparent asymmetry in the lateral distribution of the radio signal [108]. The energy fluence along the positive and negative $\vec{v} \times (\vec{v} \times \vec{B})$ axes was

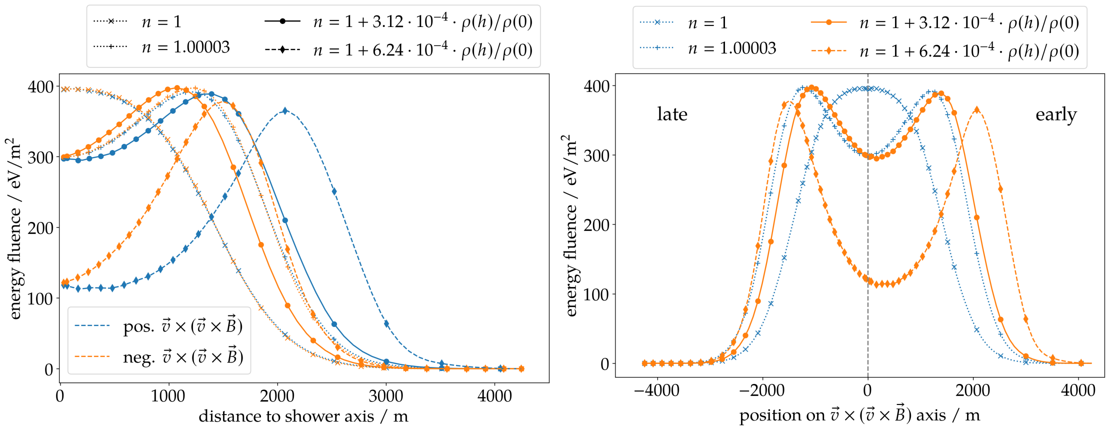

Figure 5.5: Lateral distribution of the radio emission of a 85° air shower along the positive and negative $\vec{v} \times (\vec{v} \times \vec{B})$ axes with respect to the MC impact point for four different atmospheric refractivity profiles. Visualization of the apparent asymmetry of the energy fluence on the $\vec{v} \times (\vec{v} \times \vec{B})$ axis, positive and negative direction denoted by color (left). Observed offset of the symmetry center (right). Blue lines show constant values of the refractive index without an offset of the symmetry center. For a changing refractive index (orange lines) the symmetry center is displaced in the direction of the positive $\vec{v} \times (\vec{v} \times \vec{B})$ axis.

expected to be symmetric, however, an asymmetry of both axes can be seen in Fig. 5.5 (left). This apparent asymmetry could be explained by an offset of the symmetry axis from the MC shower axis, cf. Fig. 5.5 (right). For a constant refractive index of 1 and 1.000 03 (approximately the value of $n(h_{\mathrm{max}})$ at X_{max}) no offset and therefore also no asymmetry is found. However, with a changing refractive index that follows the density gradient in the atmosphere the symmetry center shows an offset in the direction of the positive $\vec{v} \times (\vec{v} \times \vec{B})$ axis which increases when e.g. doubling the reactivity throughout the atmosphere.

In the following, a new method for estimating the symmetry center is explained that only utilizes the presence of the Cherenkov ring. Then, it is applied to the simulations of the *RdHasLib*, and the displacement of the radio symmetry center and the MC impact point is analyzed and compared to a model describing the propagation of an electromagnetic wave through the Earth's atmosphere including refraction according to Snell's law.

5.4.1 Fitting the Cherenkov ring

To estimate the symmetry center of the radio footprint a purely geometrical method is used that does not rely on a detailed understanding of the lateral distribution of the radio emission and is therefore model independent. As explained in section 2.4, the radio signal is enhanced on a ring around the shower axis due to a Cherenkov-like compression of the radio emission. This feature is fitted by a ring that yields the symmetry center and the radius of the ring. The radio-emission footprint is described in terms of the *geomagnetic*

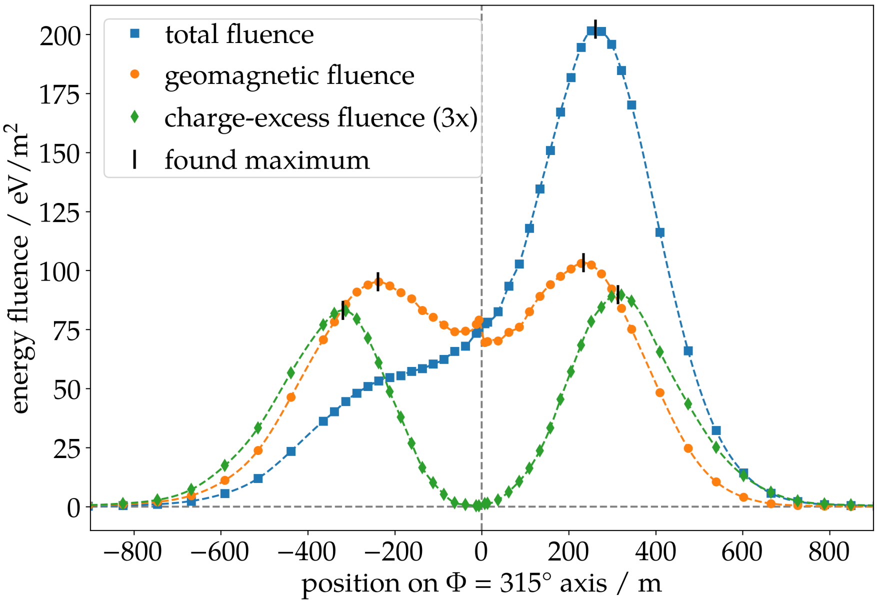

Figure 5.6: Comparison of the geomagnetic, charge-excess, and total energy fluence for an air shower coming from North with a zenith angle of 65°. The charge-excess contribution is multiplied by a factor of 3. Observers are shown on an axis with $\Phi = 315°$, negative values correspond to the $\Phi = 135°$ axis. The found maxima are marked by black vertical lines on the LDF. For the geomagnetic energy fluence, a non-physical behavior can be seen close to the shower axis. This is an artifact of using the MC impact point as the radio symmetry center in the calculation.

energy fluence, f_{geo}, and *charge-excess energy fluence*, f_{ce}, which can be calculated from the energy fluence in the $\vec{v} \times \vec{B}$ and $\vec{v} \times (\vec{v} \times \vec{B})$ polarization via [85, derived equation]:

$$f_{\mathrm{geo}} = \left(\sqrt{f_{\vec{v}\times\vec{B}}} - \frac{\cos\Phi}{|\sin\Phi|} \sqrt{f_{\vec{v}\times(\vec{v}\times\vec{B})}} \right)^2 \tag{5.2}$$

$$f_{\mathrm{ce}} = \frac{1}{\sin^2\Phi} f_{\vec{v}\times(\vec{v}\times\vec{B})} \tag{5.3}$$

Here, Φ denotes the polar angle in counterclockwise direction of the pulse position in the shower plane with respect to the positive $\vec{v} \times \vec{B}$ axis going through the symmetry center of the radio emission.

For air showers with a small geomagnetic angle α the geomagnetic emission is weak and the interference of both emission mechanisms has a strong impact on the position of the maximal energy fluence and can even completely suppress the Cherenkov ring in the negative $\vec{v} \times \vec{B}$ half-plane. An example shower coming from North with a zenith angle of 65°, corresponding to $\sin\alpha \approx 0.19$, is shown in Fig. 5.6. For the total energy fluence no ring can be estimated for signals with $\Phi = 135°$. However, the geomagnetic and charge-excess energy fluences individually exhibit a clear maximum. Note that the MC impact point was used for the calculation of f_{geo} which does not describe the true radio symmetry center. Even though the displacement between the true symmetry center and the MC impact point is small at this zenith angle it still introduces a non-physical artifact in f_{geo} close to the shower axis. It can be seen that f_{ce} exhibits a broader Cherenkov ring than f_{geo}. Thus, the contributions will be fitted independently.

The calculation of f_{geo} and f_{ce} depends on the location of the radio symmetry center via the polar angle Φ. Therefore, an iterative process is used that first calculates f_{geo} and f_{ce} using the current symmetry center and then fits the Cherenkov ring to obtain a new symmetry center. In each iteration, the maximum energy fluence is calculated for every arm of the star-shaped grid using a cubic spline interpolation. The impact of the underlying interpolation function and the spacing of the interpolated points used to find the maxima on each arm is found to be negligible for the obtained results. For the minimization process a least-squares method with equal weights for each ring position is used. As the calculation of f_{geo} and f_{ce} becomes nonphysical for small values of $\sin\Phi$ the $\vec{v} \times \vec{B}$ axis is excluded from the fit. Note that pulses along this axis will not remain at $\Phi = 0°$ and $\Phi = 180°$ respectively and the equations above could provide reasonable energy fluences using the true radio symmetry center. However, a varying number of data points during the fit could result in a bias.

An example fit of the geomagnetic emission for an event with a zenith angle of 85° coming from North-West is shown in Fig. 5.7. The displacement between the radio symmetry center and the MC impact point in the shower plane is estimated as $(125 \pm 21)\,\mathrm{m}$. This is a small effect compared to the fitted Cherenkov radius of $(1198 \pm 10)\,\mathrm{m}$. However, due to the high inclination this corresponds to a displacement of $(1428 \pm 240)\,\mathrm{m}$ on ground. Using the Monte Carlo impact point the maximal difference between the individual Cherenkov radii found on the individual arms is estimated as 268 m. This difference reduces to 40 m by using the radio symmetry center.

The presence of two different Cherenkov rings with a similar strength encoded into the total energy fluence makes it challenging to disentangle both in the fit. Therefore, only air showers with a geomagnetic angle that fulfills $\sin\alpha > 0.25$ will be used in the fit of the Cherenkov ring to the dominant geomagnetic emission. For air showers with a smaller geomagnetic angle the obtained Cherenkov radii of the geomagnetic and charge-excess emission will be compared and a potential asymmetry in the charge-excess contribution is analyzed.

5.4.2 Displacement of the radio symmetry center

The ring fits yield accurate results for the 4185 simulated air showers of the *RdHasLib* that fulfill $\sin\alpha > 0.25$. The resulting displacements are interpreted as a function of the geometric distance d_{max} from the MC impact point to X_{max}. In first order, d_{max} scales with the zenith angle and only in second order with X_{max}. It can be calculated by

$$X_{\mathrm{ground}} - X_{\mathrm{max}} = \int_0^{d_{\mathrm{max}}} \rho(\ell)\,\mathrm{d}\ell. \tag{5.4}$$

Here, the atmospheric slant depth of the ground plane measured along the shower axis is denoted by X_{ground}, $\rho(\ell)$ denotes the atmospheric density at the distance ℓ along the MC

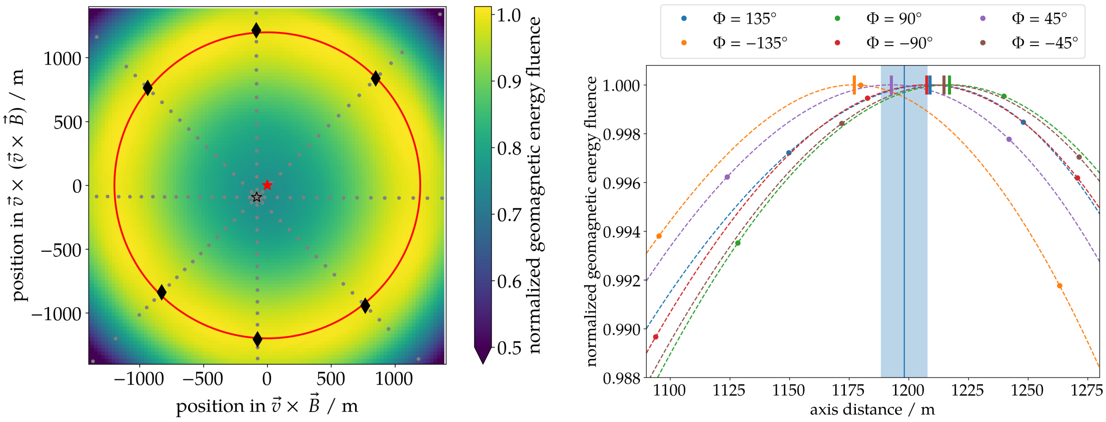

Figure 5.7: Result of the iterative fit procedure to estimate the radio symmetry center. The geomagnetic energy fluence is normalized to the maximum along each arm as only the position of the Cherenkov ring, but not its signal strength, is used in the fit. 2D visualization of the fitted Cherenkov ring (left). For illustration purposes the background constitutes the cubic interpolation of the geomagnetic energy fluence from signals around the Cherenkov ring. Signals on or close to the $\vec{v}\times\vec{B}$-axis are recovered using the found radio symmetry center (cf. [109]). The fitted Cherenkov ring and the estimated radio symmetry center are shown in red. The black star marks the position of the MC impact point, gray dots show the positions of the simulated pulses. The positions of maximal geomagnetic energy fluence found for each arm of the star-shaped grid are denoted by the black diamonds. 1D lateral distribution of the geomagnetic energy fluence for each polar angle of the star-shaped grid except for the $\vec{v}\times\vec{B}$ axis (right). Colored points denote the calculated geomagnetic energy fluence for the simulated pulses. Their interpolation is shown by the dashed lines for each arm, the position of the maximum geomagnetic energy fluence is marked by the colored vertical line. The blue line and box denote the fitted radius of the Cherenkov ring and its uncertainty. The axis distances displayed on the x-axis are calculated using the fitted radio symmetry center.

shower axis in the direction of X_max. For inclined air showers the integral can only be solved numerically as the atmospheric curvature needs to be taken into account. Due to the displacement of the radio symmetry center in the incoming direction of the air shower (shown in the following) the actual geometrical distance to X_max is smaller. However, the deviation is of the order of $\lesssim$1 % and therefore negligible.

The obtained displacements between MC impact point and radio symmetry center are summarized in Fig. 5.8. At the highest inclination the displacement in the shower plane increases up to 15 % of the Cherenkov radius. The displacement exhibits a pronounced scatter that is related to the arrival direction of the air shower. The displacement is strongest for air showers coming from West and weakest for air showers coming from East. In the ground plane the displacements exceed 1500 m which is of the same order as the spacing of the stations for the AugerPrime Radio Detector.

The displacement on ground is compared to the prediction of a model that describes the propagation of an electromagnetic wave through the Earth's atmosphere including

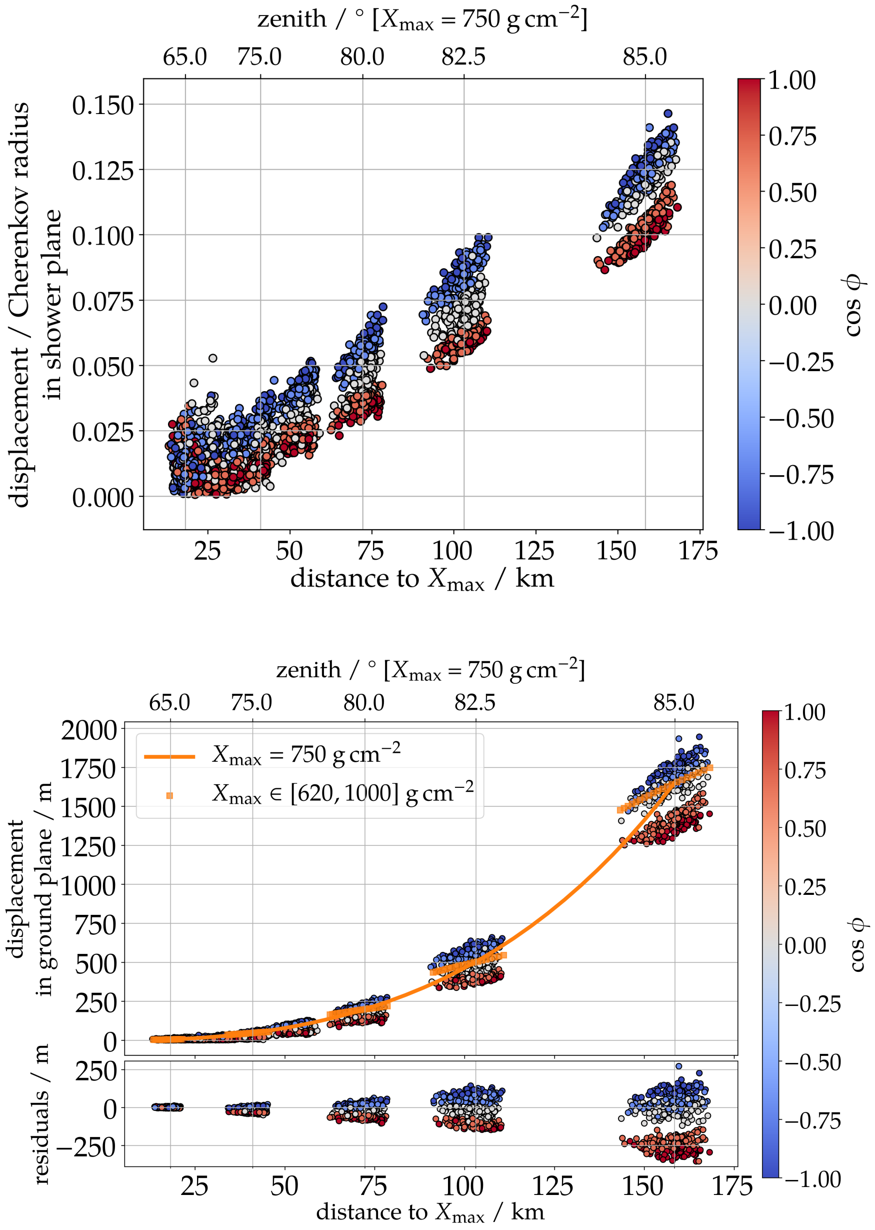

Figure 5.8: Displacement of the radio symmetry center with respect to the MC impact point in the shower plane normalized to the fitted radius of the Cherenkov ring as a function of the distance to the shower maximum (bottom x-axis) as well as the zenith angle (top x-axis) (top). The color-coded cosine of the azimuth arrival direction illustrates an East ($\cos\phi = 1$) West ($\cos\phi = -1$) asymmetry. Comparison between model-predicted and CoREAS-derived displacement of the radio symmetry center in the ground plane (bottom). The orange line shows the model prediction for a source at a fixed slant depth of $X_{\mathrm{max}} = 750\,\mathrm{g/cm^2}$. The orange squares show the displacement as a function of the source slant depth (e.g. X_{max}). The residuals are shown in the bottom frame.

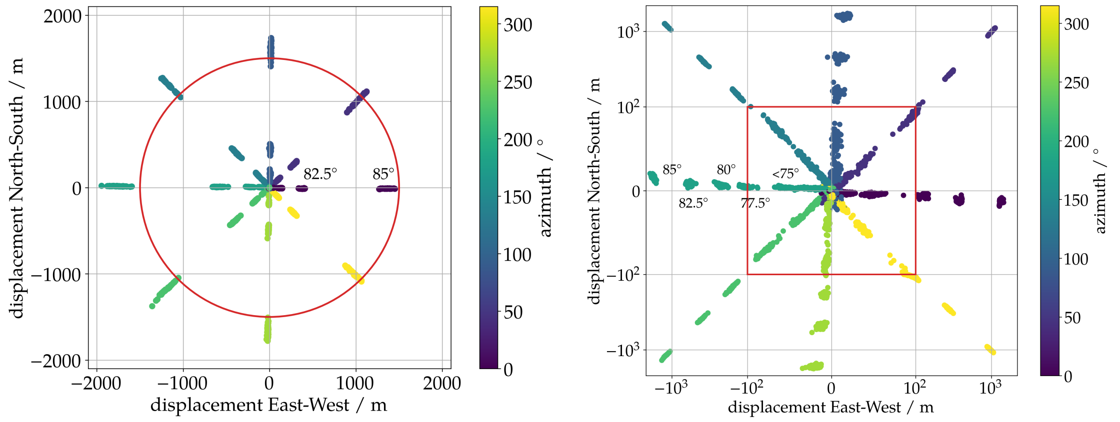

Figure 5.9: Displacement of the radio symmetry center in the ground plane relative to the MC impact point in the coordinate origin. The clustering of points originates from the binned MC arrival direction of the *RdHasLib*. Distinguishable zenith angle bins are annotated in the plots. The displacement is shown once with a normal axis scale (left) and one with a logarithmic axis scale that switches back to a linear one inside of the red square (right). The red circle denotes a constant displacement of 1500 m.

refraction according to Snell's law, cf. [110] for further details. The overall magnitude of the displacement is reasonably described by the model. For five different zenith angles ($\theta = 65°$, $75°$, $80°$, $82.5°$, $85°$) the displacement is calculated for slant depths between $620\,\mathrm{g/cm^2}$ and $1000\,\mathrm{g/cm^2}$ which corresponds to the typical X_max range in the *RdHasLib*. For a fixed zenith angle the slope of the obtained displacements matches with the model prediction. The bottom frame shows the absolute residuals between the displacement obtained from CoREAS simulations and the prediction of the refractive model. For their calculation the model prediction is interpolated to match the d_max of the simulated air showers. The residuals show no strong correlation with depth of shower maximum and increase up to ∼250 m for the most inclined air shower.

In Fig. 5.9 the position of the fitted radio symmetry center on ground with respect to the MC impact point in the origin is shown. The displacement of the radio symmetry center is always in the incoming direction of the air shower, i.e. a displacement from the MC impact point along the shower axis projected onto the ground into the direction of X_max. An East-West asymmetry is found that corresponds to the previously described scatter. The atmosphere in CoREAS is rotationally symmetric and can therefore not cause such an asymmetry. A possible explanation could be a displacement already in the particle cascade due to deflection in the Earth's magnetic field. Also an additional small rotation of the displacement pattern is found. The East-West asymmetry as well as the rotation need further investigations that are beyond the scope of this thesis.

5.4.3 Additional checks for air showers with a small geomagnetic angle

Further studies are performed on 120 air showers coming from North with zenith angles below 70°, which corresponds to $\sin\alpha < 0.25$. Due to the relatively strong charge-excess

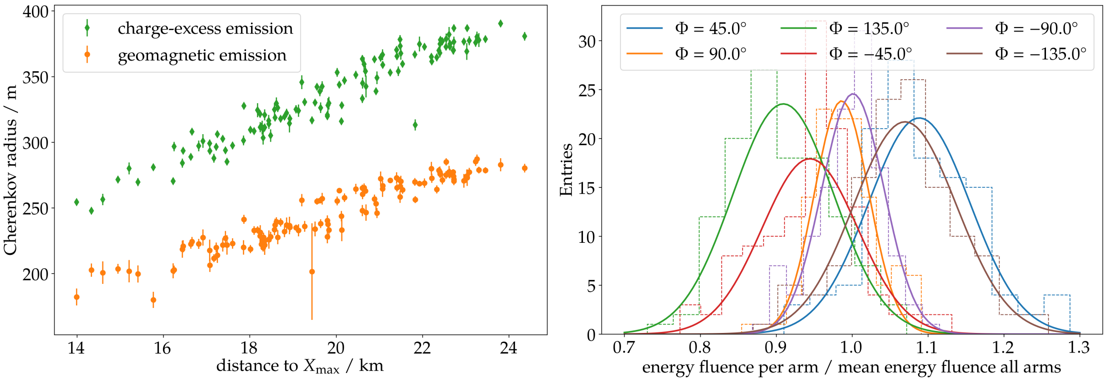

Figure 5.10: Fitted Cherenkov radius of the geomagnetic and charge-excess emission contributions individually as a function of the distance to the shower maximum (left). Ratio of the charge-excess energy fluence at the Cherenkov ring of one arm and the mean energy fluence of all arms (right).

contribution it is not possible to determine the symmetry center accurately. However, for those zenith angles the displacement is still small enough such that the MC impact point serves as a good approximation.

The Cherenkov radii of charge-excess and geomagnetic emission are analyzed independently and shown in Fig. 5.10 (left). The estimated radius of the Cherenkov ring is systematically larger for the charge-excess contribution than for the geomagnetic emission, as already shown in Fig. 5.6. The height h of the emission region can be estimated from the Cherenkov radius using the definition of the Cherenkov angle $\theta_{\mathrm{Ch}} = \arccos(1/n(h))$. The larger radius of the Cherenkov ring indicates that the charge-excess emission originates from higher up in the atmosphere than the geomagnetic emission. This is in agreement with [22] but contradicts [111] where it was found that the charge-excess induced current peaks deeper in the atmosphere. Further studies will have to be performed to clarify these observations.

The assumption of a rotational symmetry of the charge-excess emission is also studied. Already in [22] an asymmetry for one example event was reported. Further studies [112] showed a scatter of the charge-excess contribution for different locations in the same air shower rather than an asymmetry. The energy fluence of the charge excess contribution on the Cherenkov ring is determined for all arms of the star-shaped pattern, except of the $\vec{v} \times \vec{B}$ axis. For each event, the energy fluence of one arm is normalized to the average energy fluence of all arms. A deviation from rotational symmetry is found with a standard deviation of 9 %. No convincing proof of a preferred orientation of this asymmetry is found. In Fig. 5.10 (right) the ratio is shown for each analyzed arm of the star-shaped pattern individually. A potential difference between the two diagonal axes of the star-shaped pattern is found. The low number of events and the usage of the MC impact point in the calculation of the charge-excess energy fluence make it challenging to determine the significance of this result.

5.4.4 Displacement of particle and radio core in data

As the displacement of the radio symmetry center is only a small effect it is challenging to observe it in data. In the shower plane (not shown above) the displacement varies between 0 m and 175 m for 85° zenith angle (∼80 m for 80°). For inclined air showers an average distance between the reconstructed and true core position of 108 m is found, ranging from 80 m to 160 m as the zenith angle increases from 60° to 80°, for the 1500 m array of the SD [70]. Hence, the SD core bias is consistently stronger than the predicted radio core displacement.

No preferred direction of the SD bias is given in [70], whereas the radio core is displaced into the incoming direction of the air shower which corresponds to the positive $\vec{v} \times (\vec{v} \times \vec{B})$ axis in the shower plane. The position of the radio core, as reconstructed with the `RdHASLDFFitter`, in the shower plane given by the SD geometry is calculated for one year of reconstructed AERA data. From the refractive core displacement an increasing distance in the positive $\vec{v} \times (\vec{v} \times \vec{B})$ direction is expected for more inclined air showers. In contrast, it has no impact on the core displacement in the $\vec{v} \times \vec{B}$ direction. No difference of both directions is found. The obtained scatter of the radio core exceeds the predicted displacement by more than a factor of five. The refractive displacement is too small to be observed with the 1500 m array given the statistical and systematic uncertainties of the core estimation.

A more precise core estimation is expected with the 750 m array. However, this is a non-standard reconstruction in $\overline{\text{Off}}\underline{\text{line}}$ where a potential bias and the resolution are unknown. The `SdTopDownSelector` needs to be modified in a non-invasive way to not reject the stations of the 750 m array[1]. In addition, only contained radio events are used as the radio core estimation should be superior to uncontained events. Again, no indication of a systematic displacement of the radio core is observed.

5.5 Shape of the radio wavefront

Parts of this chapter have been published in:

M. Gottowik,
„Directional reconstruction of the radio signals with a spherical wavefront model“, Internal note of the Pierre Auger Collaboration (2020), GAP 2020-055

The wavefront of the radio emission can be described as a function of the *geometric delay* τ, i.e. the delay of the signal arrival time for different observers in the shower plane with distinct distances to the shower axis. For a plane wave all observers in the shower plane will observe the radio emission at the same time, i.e. $\tau = 0$ by definition. For

---

[1] The default behavior would only select SD stations on the 1500 m grid inside the boundaries of the 750 m array.

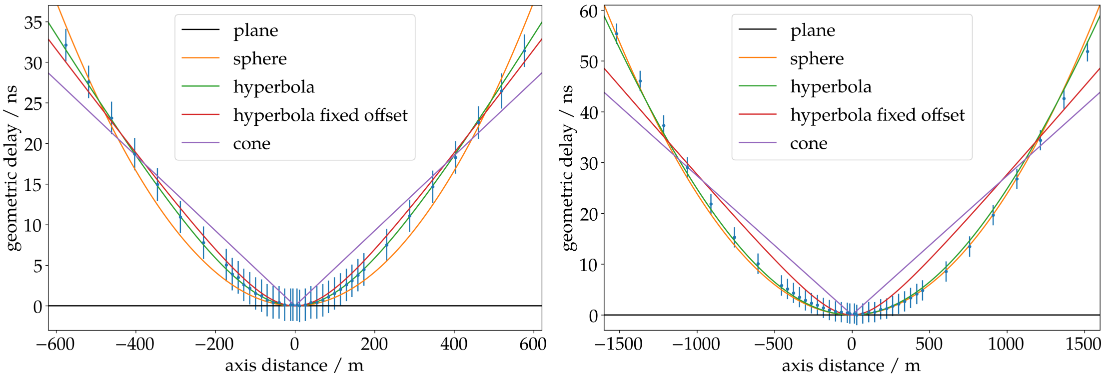

Figure 5.11: Comparison of the geometrical delay of the planar, spherical and two hyperbolic (with free and fixed offset parameter) wavefront models for air shower simulations with a zenith angle of 60° (left) and 80° (right).

all other models, a station that is further away from the shower axis will observe the radio emission at a later time than a station close to the shower axis. The analytical description of τ depends on the assumed wavefront model. For the typical models, i.e. conical, hyperbolic, and spherical, the equations are given in [82]. Compared to the plane wave the conical and spherical models involve one additional fit parameter, the cone angle and the sphere's radius respectively. The hyperbolic wavefront requires two additional parameters, the angle of the asymptotic cone and its offset with respect to the shower plane at the shower axis.

The accuracy of these wavefront models is evaluated on two CoREAS simulations of inclined air showers with zenith angles of 60° and 80°. For both simulations the observers are located on a star-shaped grid along the $\vec{v} \times \vec{B}$ and $\vec{v} \times (\vec{v} \times \vec{B})$ direction and their bisections in the shower plane. The simulations are reconstructed including noise with $\overline{\text{Off}}\underline{\text{line}}$ to calculate the signal arrival time of each observer. No time jitter is added and the traces are upsampled by a factor of 40 to retain the ideal wavefront. The reconstructed signal time uncertainties are dominated by a global station timing uncertainty that is arbitrarily set to 2 ns.

The resulting wavefront fits are shown in Fig. 5.11. Neither the plane wave nor the conical model describes the wavefront of inclined air showers correctly. The hyperbolic model is fitted once with an offset parameter fixed to −3 ns [82] and once as a free parameter. The results of both hyperbolic models and the spherical one are broadly similar for the 60° zenith angle shower. The wavefront is described best by the hyperbolic model with a free offset parameter which is determined as (-4.5 ± 0.9) ns. Fixing the offset parameter changes the shape only marginally. At an inclination of 60° the emission region is still close to the observer such that the spherical model differs slightly from the true wavefront. This changes completely for the 80° zenith angle shower. The spherical model is almost similar to the hyperbolic model with a free offset parameter which is determined as (-14 ± 5) ns whereas the hyperbolic model with fixed offset parameter clearly deviates.

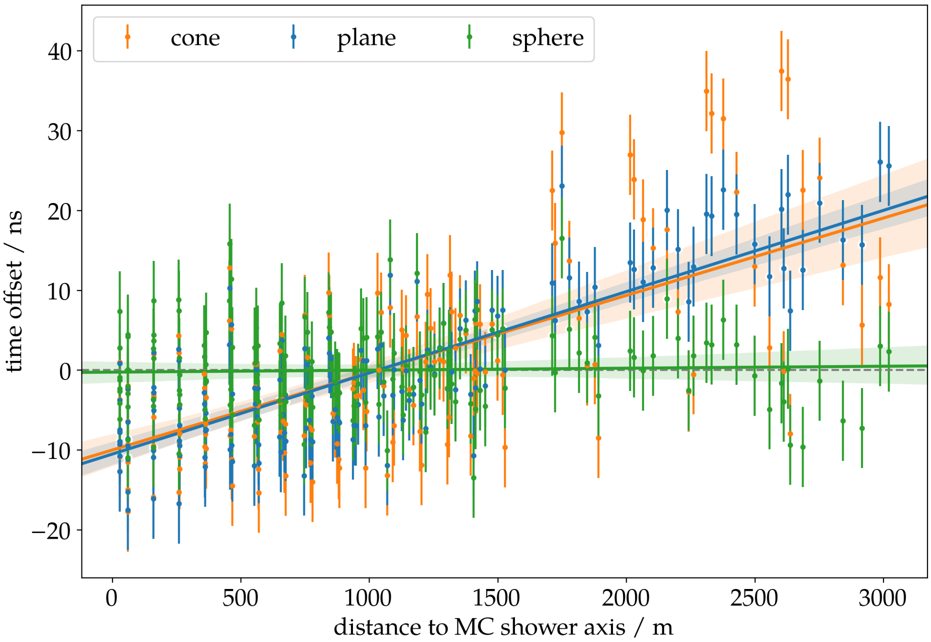

Figure 5.12: Residuals of planar, conical and spherical wavefront fit. For each model a linear regression model is fitted and the 95 % confidence interval is indicated by the colored band.

Over the whole zenith angle range the best description of the wavefront is given by the hyperbolic wavefront with a free offset parameter. However, this model requires one more fit parameter than the other models and two parameters more than a plane wave model. Hence, five signal stations are needed for such a wavefront fit. Especially with the AugerPrime Radio Detector the number of signal stations will be lower for inclinations up to 70° where the impact of the wavefront model is strongest. However, the spherical model still yields a reasonable description of the wavefront for inclined air showers.

This can also be seen by looking at the residuals of the signal arrival time. A fit of the spherical and conical wavefront model is already implemented in the $\overline{\text{Off}}\underline{\text{line}}$ module `RdWaveFit` [113], a hyperbolic wavefront is not implemented. Fig. 5.12 shows the signal time residuals assuming a planar, conical and spherical wavefront for an example shower with a zenith angle of 65° using the full star-shaped grid of observers. For a spherical wavefront the residuals are in agreement with zero even at a larger distance from the shower axis, whereas they clearly increase with axis distance for a plane and conical wavefront. Therefore, the spherical wavefront is analyzed further for inclined air showers.

The `RdWaveFit` performs a step-wise reconstruction of the shower direction. A plane wavefront is fitted which is then used as input for the spherical fit. This makes it challenging to include that module in the standard reconstruction as the wavefront model is also used to reject noise stations via the signal arrival time, cf. section 4.4.3. With this step-wise reconstruction the wavefront model can change when adding new stations to the fit, which may cause misclassification of stations.

Therefore, a fit of the spherical wavefront model is implemented in a new Offline module called `RdSphericalFit` without an implicit plane wave prefit. The predicted arrival times t_i at a station i are calculated via

$$t_i^{\text{sphere}}(R, \theta, \phi) = |\vec{R}(R, \theta, \phi) - \vec{d_i}|/c \tag{5.5}$$

where $\vec{R}$ denotes the source point of the spherical wave and $\vec{d_i}$ the station position relative to the shower core. It is assumed that the radio emission propagates with the speed of light c, i.e. the effective refractive index n in the line from the source point to the antenna is set to unity. In [113] it has been found that nonphysical situations can arise for air showers coming from close to the horizon. The signal time difference of nearby stations can be smaller than the time needed for a propagation with the speed of light which results in a reconstructed shower axis lying inside of the detector plane. An additional variation of the speed of light, c/γ, was introduced to resolve this issue. Typically $\gamma < 1$ was obtained by the fits, which goes towards the opposite direction than including a variation of the propagation time with the effective refractive index $n > 1$. No strong evidence for this artifact is found in the following analysis, hence a fit of the γ parameter is not performed by the current implementation. If proven necessary, it can easily be included.

Strictly speaking, the spherical wavefront does not depend on a core position but only on the distance to the point source. The shower axis is then given as the connection between the assumed core and the point source. A wrong core will therefore provide a precise description of the signal arrival times, but not of the shower direction with respect to the SD direction.

In the following the spherical and plane wave models are compared. The achievable directional resolution is analyzed based on simulations with a star-shaped grid of observers. In addition, both models are applied to AERA data and simulations as well as to simulations for the AugerPrime Radio Detector. The potential of using the spherical wavefront in the rejection of noise stations based on their signal time is analyzed.

5.5.1 Achievable resolution

The achievable resolution of the spherical wavefront model is evaluated with the 10 EeV energy bin of the *RdHasLib*. This results in 431 simulations as one simulation did not finish successfully due to technical reasons. The simulations are reconstructed with Offline including noise and a time jitter of 5 ns. Here, the radio barycenter is used as the core in the wavefront fit.

The reconstructed zenith angle is biased for both wavefront models as shown in Fig. 5.13 (left). The bias is consistently more prominent with the spherical model. For an inclination of 85° it amounts to ∼0.09° for the spherical model and ∼0.06° for a plane wave. The exact origin of this effect needs further investigation. As shown in section 5.4 the radio core, and therefore also the radio barycenter, is displaced from the MC core in the incoming direction of the air shower. This displacement leads to a lower inclination compared to the MC core and can therefore not explain the observed bias. The uncertainty of the zenith angle is significantly lower for the spherical wavefront compared

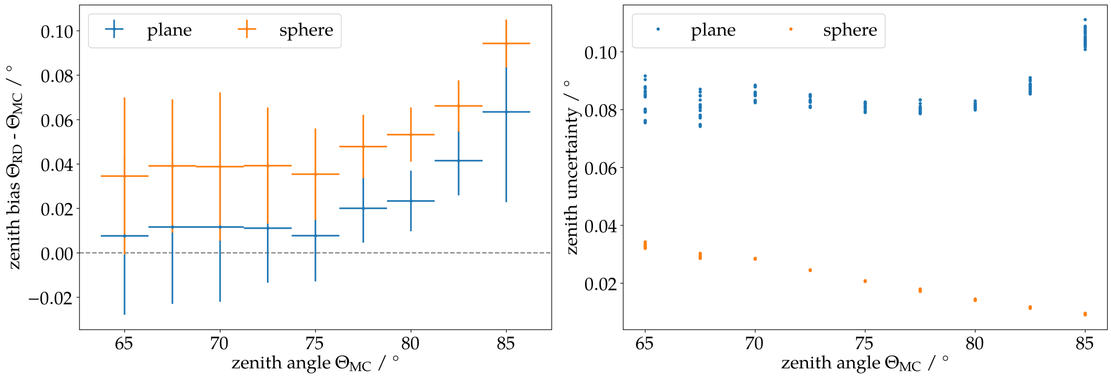

Figure 5.13: Comparison of the zenith angle reconstruction with a planar and spherical wavefront model showing a profile of the bias (left) and the individual uncertainties (right).

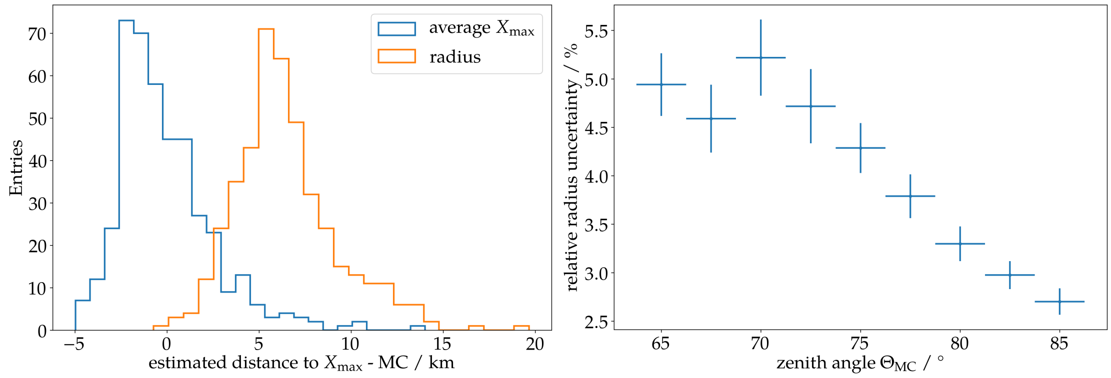

Figure 5.14: Bias of the estimated distance to X_{max} with respect to the particle X_{max} (left) and relative uncertainty of the radius (right).

to the plane wave, cf. Fig. 5.13 (right). For the plane wave model the uncertainty increases from 0.08° at 65° to 0.11° at 85°, for the spherical wave it decreases from 0.035° to 0.009°.

Within the spherical model also a radius, i.e. the distance to the source point located close to X_{max}, is reconstructed. The results are shown in Fig. 5.14. For inclinations below 70° the wavefront is not yet a sphere such that the radius shows a rather large relative uncertainty of ∼5 %. For higher inclinations the uncertainty drops continuously below ∼2.5 %. On average the radius over-estimates the distance to the particle X_{max} by 6 km with a spread of 3 km. This is in qualitative agreement with the results of [22] where it was found that the longitudinal profile of the dominating geomagnetic radio emission peaks earlier than the one of the deposited energy by particles. The geometric distance to X_{max} can also be calculated with the reconstructed zenith angle assuming an average value of X_{max}, e.g. following the FD measurements. Here, the average X_{max} of all air showers of the *RdHasLib* amounting to 757 g/cm^2 is used. Then, the bias is removed and the spread is determined as 3 km. Even in this best-case scenario of simulations on a

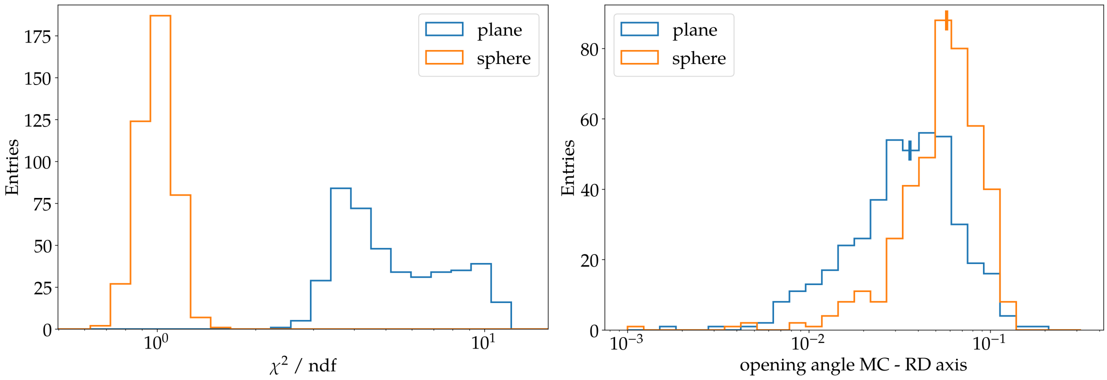

Figure 5.15: Comparison of the planar and spherical wavefront model showing the distribution of the reduced χ^2 (left) and the opening angle between the reconstructed radio and the MC axis (right) for star-shaped simulations. The vertical line indicates the position of the median opening angle.

star-shaped pattern the radius does not provide a better estimation of the distance to X_{max} than a calculation that uses an average X_{max}.

The geometric distance can be converted to a difference in the atmospheric slant depth. The calculation uses the zenith angle of the air shower as well as an atmospheric model and is therefore a more complicated quantity that involves additional uncertainties. For the US standard atmosphere after Linsley the bias in the radius translates to a bias of $(161 \pm 56)\,\text{g/cm}^2$.

A comparison of the goodness of the fit and the opening angle between the reconstructed radio and MC axis is given in Fig. 5.15. For the spherical model the reduced χ^2 is centered around one and systematically smaller than with the plane wave. The median opening angle increases from $(0.036 \pm 0.002)^\circ$ to $(0.057 \pm 0.001)^\circ$ by using the spherical model. The uncertainty of the median is estimated using bootstrapping. The larger opening angle of the spherical wavefront model has two reasons. First, with the star-shaped simulations the radio footprint is sampled symmetrically and with a dense coverage of the whole footprint. Even though the signal times are not described reasonably by a plane wave the reconstructed shower axis is still accurate. Second, the larger bias in the reconstructed zenith angle leads to a larger opening angle with the MC axis.

5.5.2 Application to AERA

CoREAS simulations with protons and iron as primary particle are performed for 160 measured AERA events [114], using the same event selection as in [108]. The air showers are reconstructed realistically with $\overline{\text{Off}}\underline{\text{line}}$ including the addition of measured noise from the time of the event and a time jitter. The reconstructed SD geometry is used as input for the spherical wavefront fit as, especially for uncontained events, the radio barycenter is not an accurate estimation of the radio core anymore. In rare cases an air shower is falsely reconstructed as coming from the horizon. These events are not used in the further analysis.

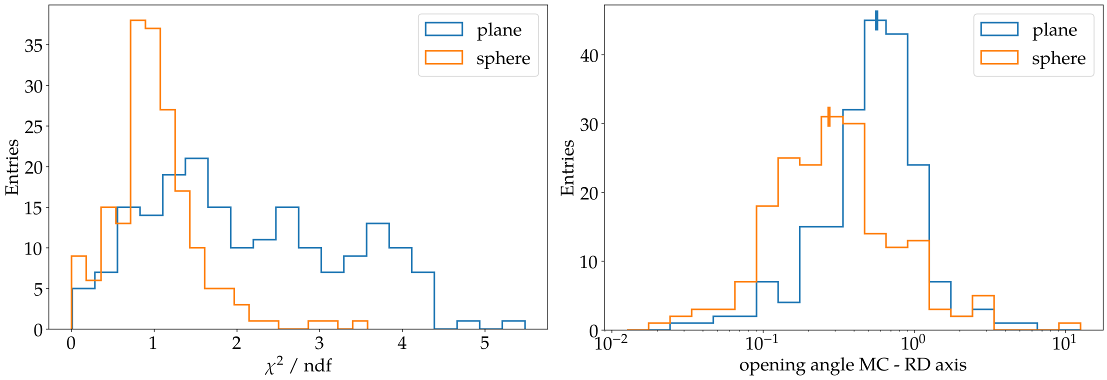

Figure 5.16: Comparison of the planar and spherical wavefront model showing the distribution of the reduced χ^2 (left) and the opening angle between the reconstructed radio and the MC axis (right) for AERA simulation. The vertical line indicates the position of the median opening angle.

In total, 205 simulated air showers are reconstructed with the plane wavefront and 194 with the spherical one. The distributions of the reduced χ^2 and the opening angle are shown in Fig. 5.16. The reduced χ^2 distribution peaks at ≈ 1 for the spherical wavefront and is systematically smaller than for the plane wavefront. With the plane wave the median opening angle is determined as $(0.56 \pm 0.04)^\circ$. As the spherical model requires one signal station more than the plane wave the direction reconstruction is naturally improved. For a fair comparison only events that are also reconstructed with a spherical wavefront are selected. For these events, the planar model yields a median opening angle of $(0.54 \pm 0.04)^\circ$. With the spherical wavefront the median opening angle reduces further to $(0.27 \pm 0.02)^\circ$. The median zenith angle uncertainty is estimated as 0.47° for the plane wave and 0.17° for the spherical one.

The estimated radius of the spheres rarely exhibits huge uncertainties of more than 100 % especially for low station multiplicity[2]. This may be due to remaining noise stations in the reconstructed event or an adverse sampling of the radio wavefront. The radius shows a bias of 10 km compared to the distance to the MC true X_{max} with a spread of 30 km. By using an average X_{max} and the reconstructed zenith angle the bias is reduced to 3 km with a spread of 6 km. Thus, the radius in general is only of limited use for a precise estimation of the distance to X_{max}, however, a very small radius could indicate an air shower that was induced by a neutrino.

The spherical wavefront model is applied to measured AERA events using the SD direction as reference. At the same time the improvement of the directional reconstruction due to the different wavefront and the beacon timing correction is evaluated. Note that the radio direction can be more accurate than the SD axis as the spacing between stations is smaller and the station multiplicity in general higher for AERA. The data recorded in 2018 is reconstructed with both wavefront models and with and without the beacon

---

[2] A strict cut on the relative uncertainty of the reconstructed radius of 30 % was used in [115]. This has a strong impact on the spread of the distribution.

Table 5.1: Comparison of the reconstruction of AERA data using the spherical and the planar model in combination with and without the beacon timing correction. The number of reconstructed events and the median opening angle between the radio and particle shower axis are given once for all successfully reconstructed events of each configuration individually and once for the subset of 404 common events that are reconstructed by all four configurations.

			opening angle	
wavefront model	beacon correction	events	all events	common events
planar	no	460	$(1.13 \pm 0.05)^\circ$	$(1.04 \pm 0.06)^\circ$
	yes	463	$(0.89 \pm 0.04)^\circ$	$(0.84 \pm 0.04)^\circ$
spherical	no	417	$(0.89 \pm 0.06)^\circ$	$(0.86 \pm 0.05)^\circ$
	yes	423	$(0.62 \pm 0.04)^\circ$	$(0.61 \pm 0.03)^\circ$

timing correction[3]. The results are interpreted once for all reconstructed events, 463 at most for the plane wave and with beacon timing correction, and for the subset of 404 coincident events of all four reconstructions. A summary of the number of events and the median opening angle is given in Tab. 5.1. The agreement of the radio and the particle axis improves by ~0.2° with the spherical wavefront model compared to a plane wave. With the beacon correction slightly more events are reconstructed and the opening angle of both axes improves by ~0.2° for both wavefront models. The best agreement is achieved for a spherical wavefront fit and the beacon correction with a median opening angle of $(0.61 \pm 0.03)^\circ$.

5.5.3 Application to the AugerPrime Radio Detector

The 10 EeV subset of the *RdHasLib* with protons as primary particle is also simulated with stations on the 1500 m grid of the AugerPrime Radio Detector [116]. Stations that are expected to have a measurable radio signal, cf. [91] for details, are included in the CoREAS simulation. With the current trigger design the radio trace will only be read out if the WCD station generated a local trigger. Especially for inclined air showers the read out radio footprint will be truncated. For an inclination of 85° only $\mathcal{O}(20)$ instead of more than 100 signal stations will be available in the reconstruction.

Given the large spacing of stations only air showers with inclinations above 70° have enough signal stations for a spherical wavefront fit. As the plane wave requires one station less than the spherical wavefront events with inclinations larger than 67.5° can be reconstructed. Again, events that are reconstructed as coming from the horizon are rejected from the analysis. Occasionally, air showers are reconstructed as going upwards instead of downwards, e.g. with a zenith angle of 95° instead of 85°. In this case the axis will be mirrored into the downward going shower axis. This is justified because

---

[3] Cf. section 3.3 for details on the beacon. The beacon timing correction can be disabled by removing the `RdChannelBeaconTimingCalibrator` from the `ModuleSequence.xml`.

all stations are on the same height of 1400 m above sea level and the wavefront fit can therefore not distinguish between an upward and a downward going event.

With this setup, the median opening angle is determined as $(0.17 \pm 0.01)^\circ$ for the planar wavefront and $(0.12 \pm 0.01)^\circ$ for the spherical one. The plane wave is fairly accurate again as the footprint is sampled symmetrically around the shower axis. The reduced χ^2 are again smaller for the spherical wavefront and centered around one. For the plane wave a median zenith angle uncertainty of 0.25° is found, this reduces to 0.05° for the spherical wavefront. Additional material, such as plots of the opening angle and χ^2 distribution, are given in [115].

5.5.4 Top-down station selection

The wavefront model is also used in combination with the `RdTopDownStationSelector` to reject stations if their signal arrival time does not agree with the prediction of the wavefront model. In an iterative procedure, a new signal station is included in the wavefront fit. In case a noise station is present, whose signal arrival time is likely incompatible with the wavefront model, the fit will most likely result in a high χ^2 value or fail. Thus, noise stations can be detected and excluded from the reconstruction.

So far, a plane wave model is used to predict the arrival times. It was found before [80] that at a larger axis distance the signal arrives significantly later than expected from a plane wave. An additional systematic uncertainty was added to compensate for the assumption of a plane wavefront. This approach has two disadvantages. First, by artificially increasing the arrival time uncertainty the probability to accept noise stations is increased as well. Second, the systematic signal time uncertainty should ideally be dependent on the axis distance. By using a constant value of 7 ns (vertical) or 10 ns (inclined), as found in [80], there can be signal stations with an axis distance large enough such that the arrival time is still not compatible with the prediction of the plane wave, cf. Fig. 5.12.

A better solution is given by using the spherical wavefront model to predict the signal arrival time. This was not feasible with the `RdWaveFit` as the assumed wavefront model could change during the iteration of signal stations due to the reconstruction in stages. A change of the internal wavefront model could result in a misclassification of noise and signal stations. The `RdSphericalFit` can be used in combination with the `RdTopDownStationSelector`. To study the impact of the wavefront model on the rejection of noise stations AERA data of 2018 is reconstructed once with arrival times predicted by the plane wavefront and once with the spherical one.

On average, the used wavefront model hardly affects the number of reconstructed events, more than 99 % of events are reconstructed with both wavefront models. Comparing the number of signal stations in both reconstructions shows no big difference for the majority of events, cf. Fig. 5.17, as mode and median of the distribution is determined as zero, the mean value amounts to 0.1 stations less with the spherical wavefront than with the plane wave. Hence, the increased signal time uncertainty performs well enough to keep most of the signal stations in the reconstruction.

The SD zenith angle and axis distance of all signal stations for the subset of events that are reconstructed with both wavefront models and that differ in the number of signal

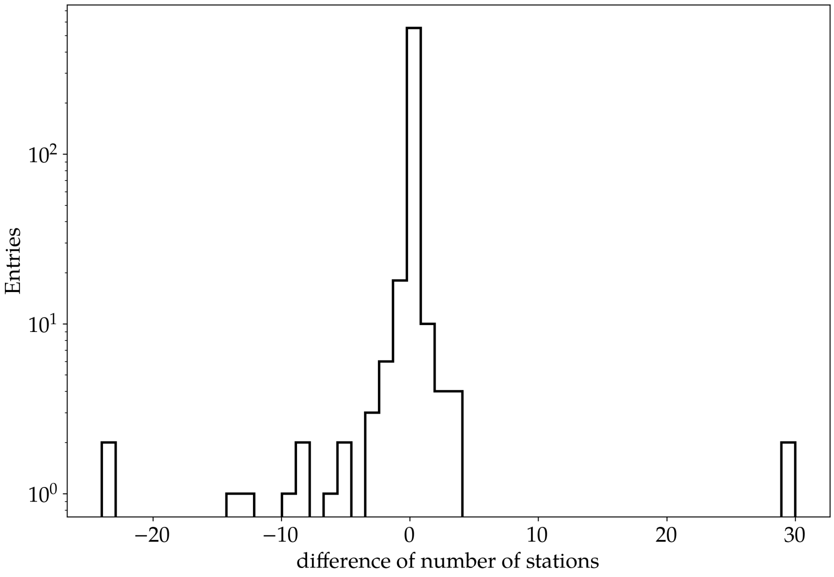

Figure 5.17: Difference of the number of signal stations reconstructed with a planar and a spherical wavefront. Positive values denote that the spherical wavefront reconstruction yields more signal stations than the plane wave one.

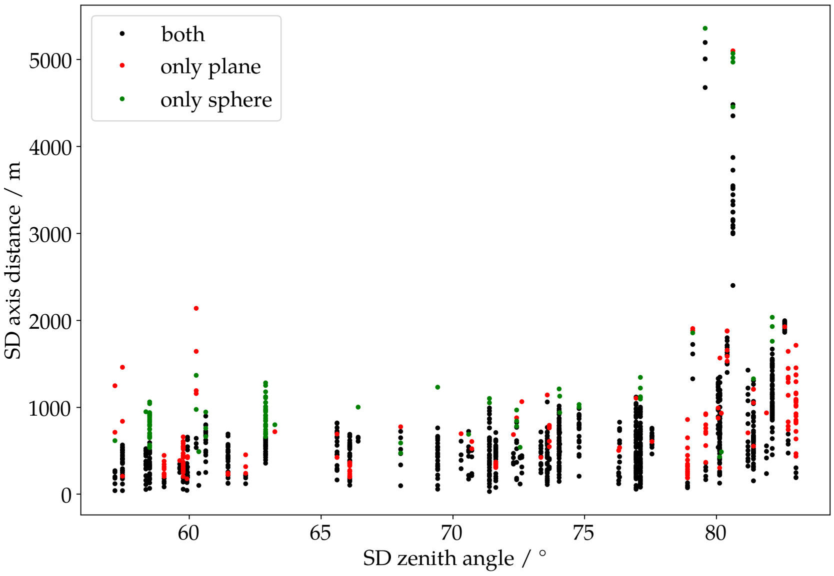

Figure 5.18: Visualization of signal stations in both reconstructions depending on the zenith angle and the distance from the shower axis. For both quantities the SD reconstruction is used. Only events reconstructed with both wavefront models and with a different number of signal stations in both reconstructions are shown. Black dots denote stations that are present in both reconstructions, red dots stations only present with the plane wave, and green dots stations only present with the spherical wavefront model.

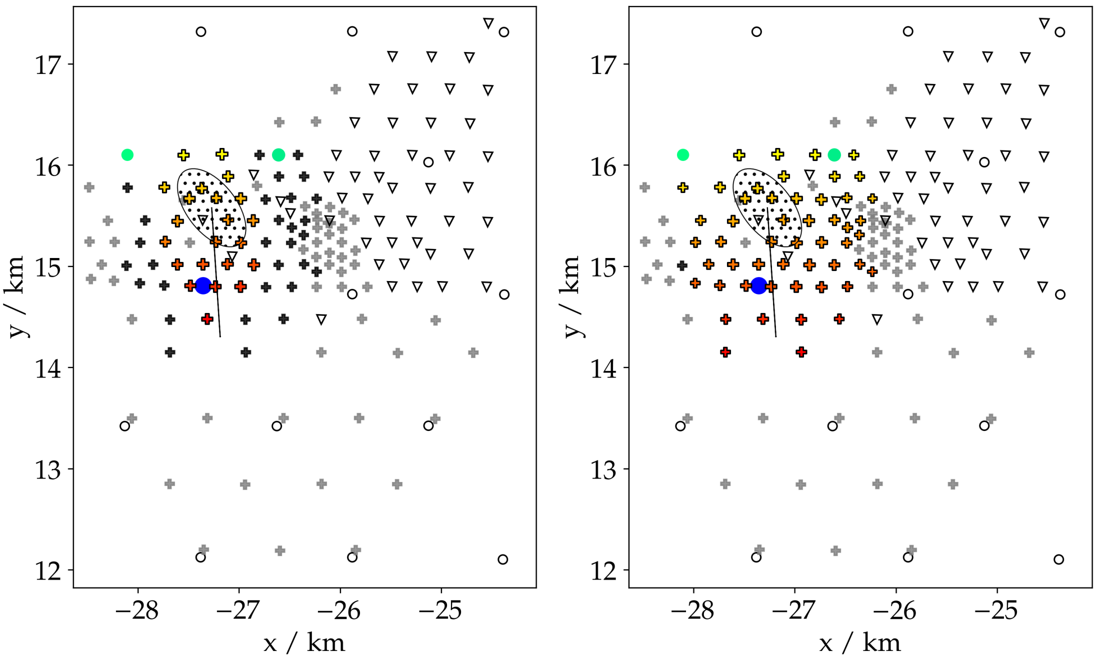

Figure 5.19: Example event reconstructed with the plane wave fit (left) and the spherical fit (right) in the top-down selection. The black plus markers denote rejected radio stations, cf. Fig. 4.9 for an explanation of all symbols. The remaining rejected station in the right figure is deselected based on the pulse shape.

stations are shown in Fig. 5.18. The spherical wavefront predominantly finds additional signal stations at larger axis distances where the plane wave predicts wrong signal times. The stations that are only included with the plane wave are distributed more evenly over the full axis distance range as the increased signal time uncertainty increases the chance of adding a noise station with a compatible signal time at all axis distances. For an estimation of the true and false rejection rate, similar to [80], a detailed MC study is needed that is beyond the scope of this thesis.

A closer look at the outliers of the distribution reveals that events where lots of stations are rejected typically contain a noise station in the starting set of stations for the iterative top-down selection. In this case the initial direction estimation is offset from the true direction. Adding true signal stations will change, in this case actually improve, the direction reconstruction by a lot. The new station will therefore be deselected. This issue only affects ∼1 % of the events and is challenging to resolve. An example event where the spherical wavefront yields 29 stations more than the plane wave is shown in Fig. 5.19. The signal arrival time of the rejected stations in the plane wave reconstruction matches the predicted arrival times of a spherical wavefront model. This event illustrates the improved performance of the top-down selection with a spherical wavefront in the case that stations at larger axis distances are available.

6 AERA Event Analysis

Parts of this chapter have been published in:

A. Aab et al. (Pierre Auger Collaboration),
„Observation of inclined EeV air showers with the radio detector of the Pierre Auger Observatory“, JCAP10(2018)026

M. Gottowik for the Pierre Auger Collaboration,
„Measurements of Inclined Air Showers with the Auger Engineering Radio Array at the Pierre Auger Observatory“, PoS(ICRC2019)274 Proceeding of 36th ICRC, 2019

In this chapter the analysis of the full AERA data set recorded between 26 June 2013 (start of AERA124) up to 16 November 2019 (latest data available in Europe[1]) is presented. Only radio stations that are able to provide data on an external trigger are used in the reconstruction. This amounts to 76 stations for AERA124, starting with 2 March 2015 onward the additional 29 radio stations of AERA153 were added to the central DAQ. The data samples of AERA124 and AERA153 were analyzed individually, no major discrepancy was found between both deployment phases.

The data is reconstructed using the `RdHASObserver` standard application of $\overline{\text{Off}}\underline{\text{line}}$, developed for this analysis. It is based on the standard SD reconstruction for inclined air showers using the 1500 m array. For the radio detection at least three antenna stations that detected a radio pulse with a signal-to-noise ratio above 10 are required. The signal-to-noise ratio is thereby defined as the squared maximum of the electric-field amplitude after projection onto the ground plane divided by the squared RMS of the background electric-field amplitudes. 3484 events are reconstructed in total, this corresponds to 1.5 events per day.

6.1 Event selection

The SD reconstruction of inclined air showers is constrained to zenith angles between 60° and 80°. Extending the reconstruction beyond zenith angles of 80° would require additional studies on the SD efficiency and maybe further optimizations of the SD

---

[1] The radio data is transferred via hard disk from Malargüe to Europe and then further processed. Due to the Covid-19 pandemic newer data is not available.

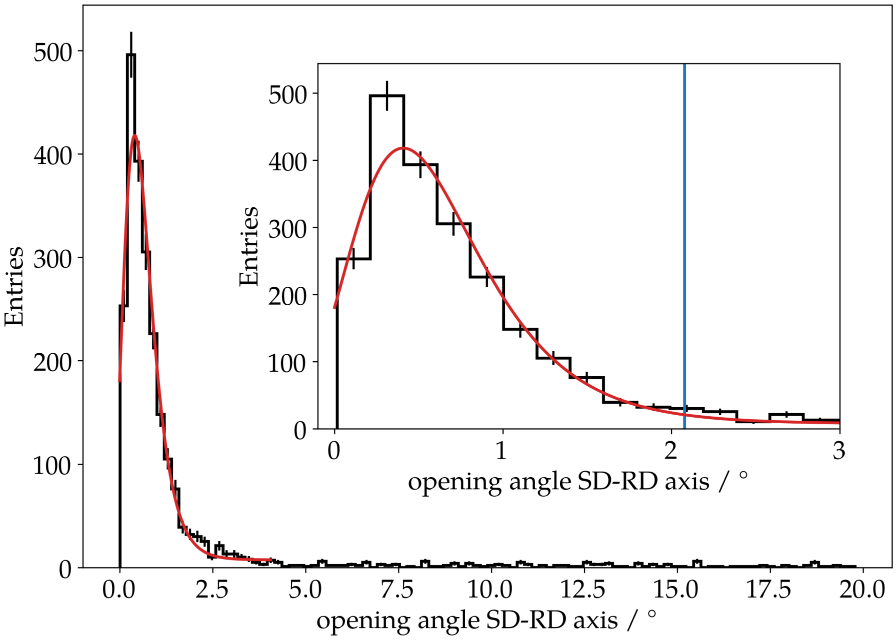

Figure 6.1: Distribution of the opening angle of the SD and RD shower axis. The Gumbel fit is shown in red. The inset figure shows a zoom onto the signal peak, the maximum opening angle of $(2.08 \pm 0.05)^\circ$ that is used in this analysis, corresponding to a 3σ-deviation from the mean of the distribution, is indicated by the vertical line.

reconstruction that are beyond the scope of this thesis. Furthermore, events during thunderstorm conditions are rejected. An event is called a thunderstorm event if at least one of the two field mills has reported thunderstorm conditions. Events where both field mills were not in operation are also rejected. The different strictness levels of the thunderstorm rejection, cf. section 4.6, have shown a negligible impact on the final results of this analysis.

The RD directional reconstruction is obtained with a spherical wavefront fit to the arrival times of the radio pulses. The distribution of the opening angle between the SD and the RD direction is shown in Fig. 6.1. The distribution is fitted with a Gumble function, i.e.

$$f(x;\mu,\beta) = \frac{1}{\beta} e^{-(z+e^{-z})}, \text{ where } z = \frac{x-\mu}{\beta}. \tag{6.1}$$

The data distribution exhibits large outliers with opening angles up to 20°, events with an even larger opening angle are already rejected by the `RdEventPostSelector` in $\overline{\text{Off}}\underline{\text{line}}$[2]. These outliers with a large opening angle are found to typically contain less than five radio signal stations. Inspecting a few outliers, they likely originate from radio events where strong noise pulses are still included in the event reconstruction or uncontained events that are only skimming AERA. Only events with an opening angle within a 3σ-interval

---

[2] This criterion was later disabled in the module and is now replaced by the corresponding ADST cut, cf. section 4.6.

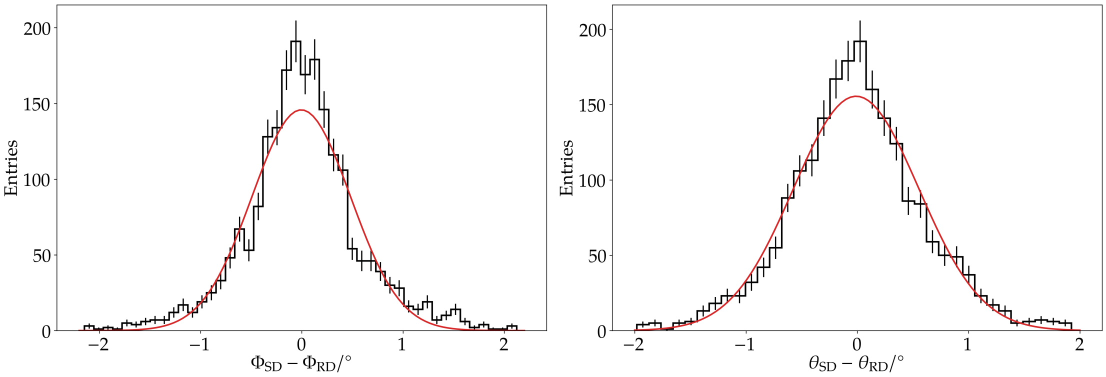

Figure 6.2: Distribution of the difference for the azimuth (left) and zenith (right) angle of the SD and RD reconstruction for the selected 2085 events with opening angles below 2.08°. A fit of a normal distribution is shown in red, the distribution is not described very well by a normal distribution.

around the mean of the Gumble fit are selected. This evaluates to a maximum opening angle of $(2.08 \pm 0.05)°$.

Even though one would expect the opening angle to follow a Rayleigh distribution, the overall shape is better described by a Gumbel distribution. To obtain a Rayleigh distribution the differences $\Delta\theta = \theta_{\mathrm{SD}} - \theta_{\mathrm{RD}}$ and $\Delta\Phi = \Phi_{\mathrm{SD}} - \Phi_{\mathrm{RD}}$ each have to be Gaussian distributed and uncorrelated. The distributions of $\Delta\theta$ and $\Delta\Phi$ are centered at zero as expected. However, both distributions have a narrower peak and fatter tails than a normal distribution, i.e. they are *leptokurtic*. This can be seen by calculating their *excess kurtosis* γ. For a normal distribution it holds $\gamma = 0$, a leptokurtic distribution has $\gamma > 0$ and a *platykurtic* distribution $\gamma < 0$. For all events that are shown in Fig. 6.1, $\gamma = 32$ is obtained for $\Delta\Phi$ and $\gamma = 24$ for $\Delta\theta$, the correlation coefficient is determined as only -0.07. Selecting only the events with opening angles below 2.08° (cf. Fig. 6.2) these number reduces to $\gamma = 1.4$ for $\Delta\Phi$, $\gamma = 0.6$ for $\Delta\theta$ and a correlation coefficient of -0.02. Hence, the distributions are still leptokurtic which leads to the opening angle not following a Rayleigh distribution.

Another coincidence check that was performed by the `RdEventPostSelector` was based on the axis distance of the RD core from the reconstructed SD shower axis. The maximal allowed axis distance was set to 2 km. In older $\overline{\text{Off}}\underline{\text{line}}$ revision the RD core could simply be the radio barycenter or the symmetry center of the radio emission. Especially for inclined and uncontained events the barycenter is not a good estimation of the radio core position, therefore this selection was deactivated. Also this selection is nowadays performed by an ADST cut. No event selection based on the axis distance of the RD core is used in this analysis, however, a maximum axis distance of ~750 m is found for those events where the radio core is determined by a fit of the lateral signal distribution. This number may be helpful for an event selection in future analyses.

The number of remaining events after each cut is summarized in Tab. 6.1, 2085 events are selected for the following analysis. The mean number of radio stations with a signal

Table 6.1: Number of events surviving the individual cuts, starting with a total number of 3484 events.

cut	number of events after cut
$\theta_{\mathrm{SD}} \geq 60°$	3017
$\theta_{\mathrm{SD}} \leq 80°$	2656
no thunderstorm	2336
SD-RD opening angle $< 2.08°$	2085

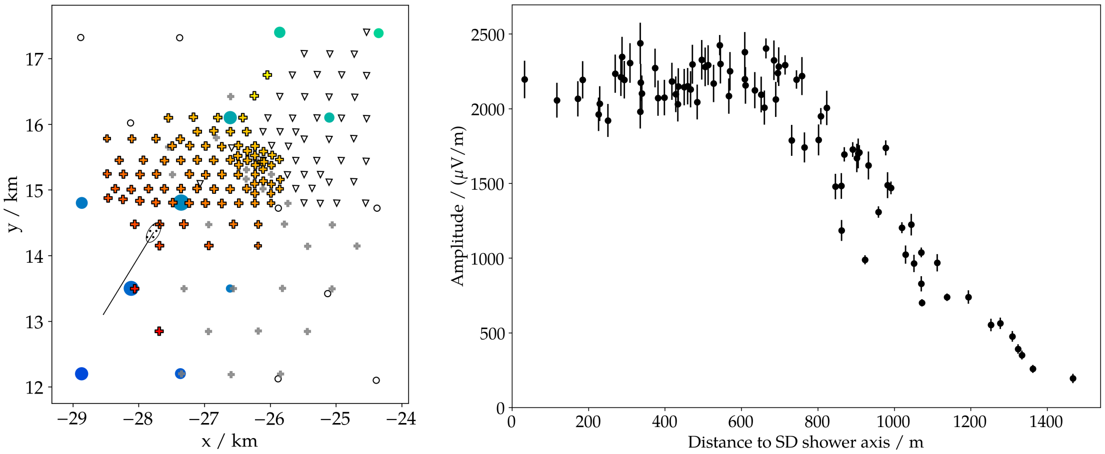

Figure 6.3: Example event with the radio ID 101420.13729 reconstructed with AERA at an inclination of 77°. Shown is an overview of the AERA stations (left, cf. Fig. 4.9 for an explanation of all symbols) and the raw lateral distribution of the radio signal (right).

amounts to 15 but goes up to 86 stations, close to the maximum possible. The event with the highest number of radio stations with a zenith angle of 77° and an azimuth angle of 238° is shown in Fig. 6.3. The measured signal amplitudes rise up to an axis distance of ~600 m, which corresponds to the expected Cherenkov radius for this zenith angle, and falls off to larger distances as expected for the radio emission of an air shower. The LDF shows the raw data and is not corrected for the known asymmetries. This example already illustrates that the footprint on ground can exceed the instrumented area of AERA.

6.2 Characterization of the total data set

The distribution of the arrival directions as determined by the SD is shown in Fig. 6.4. The azimuth distribution shows the expected North-South asymmetry. An air shower coming from North and thus close to the direction of the Earth's magnetic field produces hardly any geomagnetic radiation and has therefore a higher detection threshold on the

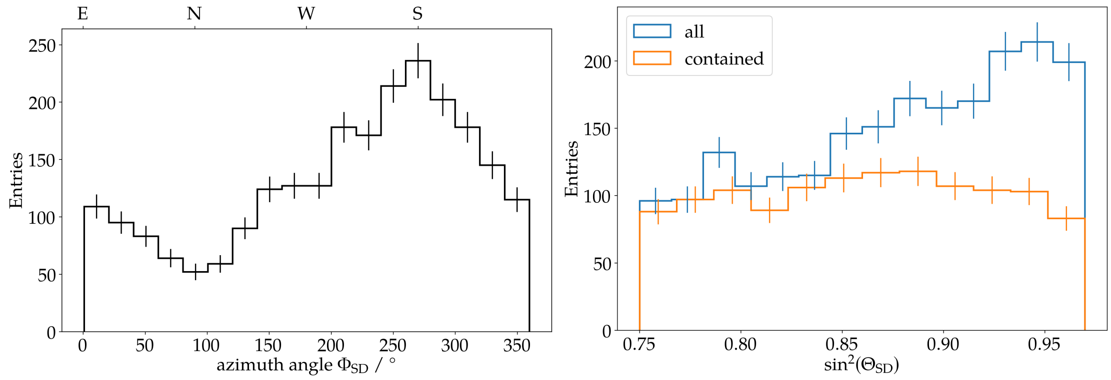

Figure 6.4: Distribution of the reconstructed SD arrival direction: azimuth angles (left) and $\sin^2\theta$ (right) for all events and the subset of contained events. Poissonian uncertainties are shown for each bin.

primary energy than an air shower coming from the South with a strong geomagnetic radio emission. The distribution of the zenith angle is shown with respect to $\sin^2\theta$. For a planar detector observing an isotropic flux with full efficiency the $\sin^2\theta$ distribution is expected to be flat. For the 1229 contained radio events, i.e. events where the SD core or a part of its uncertainty ellipse is inside the convex hull of all non-rejected signal stations, the distribution of $\sin^2\theta$ is indeed flat. Including the uncontained events the distribution of $\sin^2\theta$ increases with θ. The efficiency for a coincident observation of an air shower with SD and AERA increases with the zenith angle as the effective detection area of AERA is larger than the instrumented area due to the large radio footprint of inclined air showers.

The standard SD event selection of inclined air showers [70] is applied to ensure a proper energy reconstruction by the SD[3]. This selection requires a zenith angle between 60° and 80°, a full hexagon of signal stations around the station with the largest energy deposit, and a minimum reconstructed energy of $10^{18.6}$ eV. It yields a bias-free energy reconstruction with a resolution of 19.3 %. The energy distribution of the 117 events with a reconstructed SD energy is shown in Fig. 6.5. As AERA is rather small the event statistics at energies above $10^{18.6}$ eV is limited, however, events with energies up to $10^{19.6}$ eV have been detected. A power-law fit yields

$$N \propto E^{-\gamma} \text{ with } \gamma = 1.8 \pm 0.2, \tag{6.2}$$

a similar slope is obtained for the subset of contained events. The sloped deviates from $\gamma = 2.6$ as measured by the SD for these energies (cf. section 2.2). This may indicate a reduced efficiency in the hybrid SD-AERA event reconstruction at lower energies.

To check for hybrid FD-AERA events the standard FD ICRC2019 cuts are weakened (cf. appendix C.2) as no unbiased $X_{\max}$ distribution is required at this analysis stage.

---

[3] In previous publications, [75, 108], this selection was adapted by lowering the minimum energy to $10^{18.5}$ eV and extending the zenith angle range up to 84°. The modified selection increases the event statistics but also degrades the reconstruction performance. As there is now sufficient event statistics the standard selection is used.

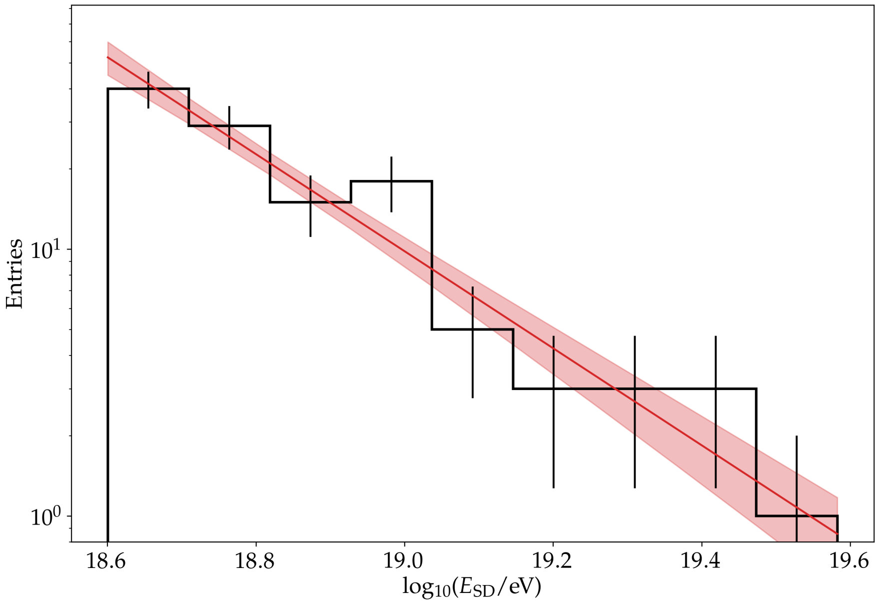

Figure 6.5: Distribution of the reconstructed SD energy. Poissonian uncertainties are shown for each bin. The fitted power law is shown in red, the colored band indicates the fit uncertainty.

Only two out of 2085 events are selected, one reconstructed by Loma Amarilla ($\theta = 72°$, $E = 2.29 \cdot 10^{19}$ eV) and one by Los Leones ($\theta = 67°$, $E = 7.43 \cdot 10^{18}$ eV). This shows that there is almost no overlap of the parameter space for the detection of inclined air showers with FD and AERA.

6.3 Size of the radio footprint on ground

As already shown in chapter 5 the radius of the radio footprint in the shower plane is expected to increase with the zenith angle as the source of the radio emission is more distant from the observer. Now, the radius is estimated from the fit of the lateral signal distribution of the `RdHASLDFFitter` for measured AERA events. As no fit parameter is a direct estimator for the size of the footprint its radius is calculated from the fit function. The distance where the radially symmetric geomagnetic LDF drops below an energy fluence of $2\,\mathrm{eV/m^2}$, which corresponds to the typical detection threshold of an AERA station regarding the total energy fluence, is defined as the radius of the radio footprint. Since there is only little charge-excess emission for inclined air showers the geomagnetic and the total radio emission are almost identical and the calculated radius should therefore match the detectable size of the radio footprint for AERA.

The resulting radius of the footprint increases with the zenith angle as shown in Fig. 6.6. The reconstructed events are separated into events with and without a reconstructed SD energy. The events with an SD energy typically have a radius larger than the mean

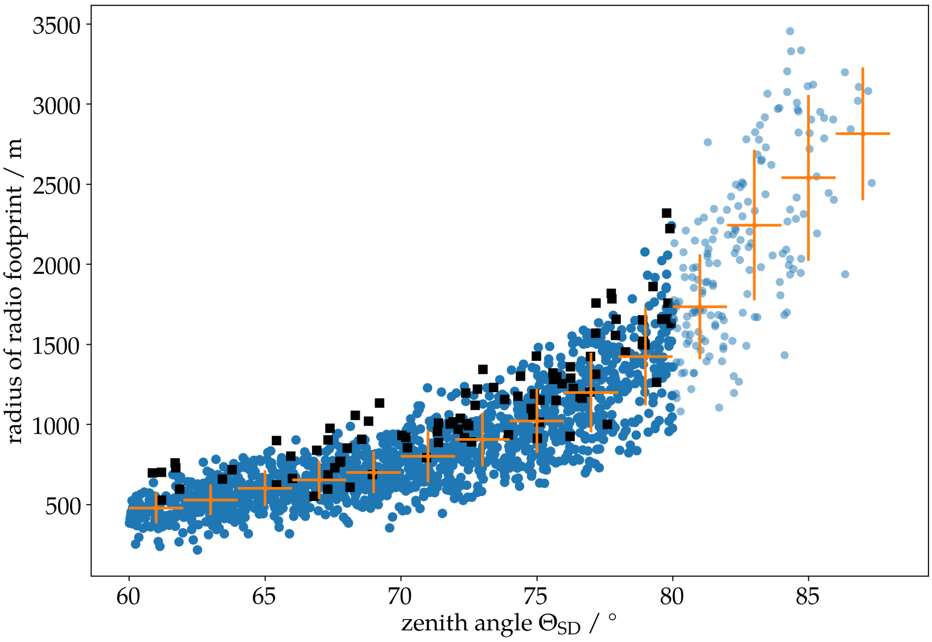

Figure 6.6: Estimated radius of the radio footprint in the shower plane as a function of the SD zenith angle. Black squares represent the events that have a reconstructed SD energy, the other events are shown as blue circles. Events with zenith angles above 80° are denoted by transparent dots. The profile of all events is shown in orange, binned in 2° zenith angle.

value of the corresponding zenith angle bin, the reason for this effect is unclear. As the LDF model is especially designed for inclined air showers 174 events with zenith angles above 80° are shown as well. The trend of an increasing footprint size continues up to the highest inclinations and confirms the theoretical expectation obtained from CoREAS simulations with measured data. Due to projection effects the illuminated area on the ground is much larger. A simple projection with a factor of $\sec(\theta)$ yields an area of $\sim 1.5\,\mathrm{km}^2$ at 60° and more than $200\,\mathrm{km}^2$ at 85°.

Due to the large footprint also events with a shower core outside of the instrumented area of AERA can be reconstructed by AERA. The distribution of the shower core on ground as reconstructed by the SD is shown in Fig. 6.7. Events with inclinations above 80° are included for this analysis again. The density of the reconstructed core positions is determined with a *kernel density estimation* (KDE) using a normal distribution as kernel and a spread as derived with *Scott's Rule* [117]. The majority of events have their shower core inside of the instrumented area of AERA, however, huge outliers occur. The event furthest away (red circle) has its shower core at a ground distance of $\sim 40\,\mathrm{km}$ from AERA. It is reconstructed with an SD energy of $(11.4 \pm 1.7)\,\mathrm{EeV}$ and an inclination of 86.8° by the SD and AERA. The radio emission was recorded by 29 antennas at an axis distance of $\sim 1500\,\mathrm{m}$ which is in agreement with the prediction of the footprint size as shown in Fig. 6.6.

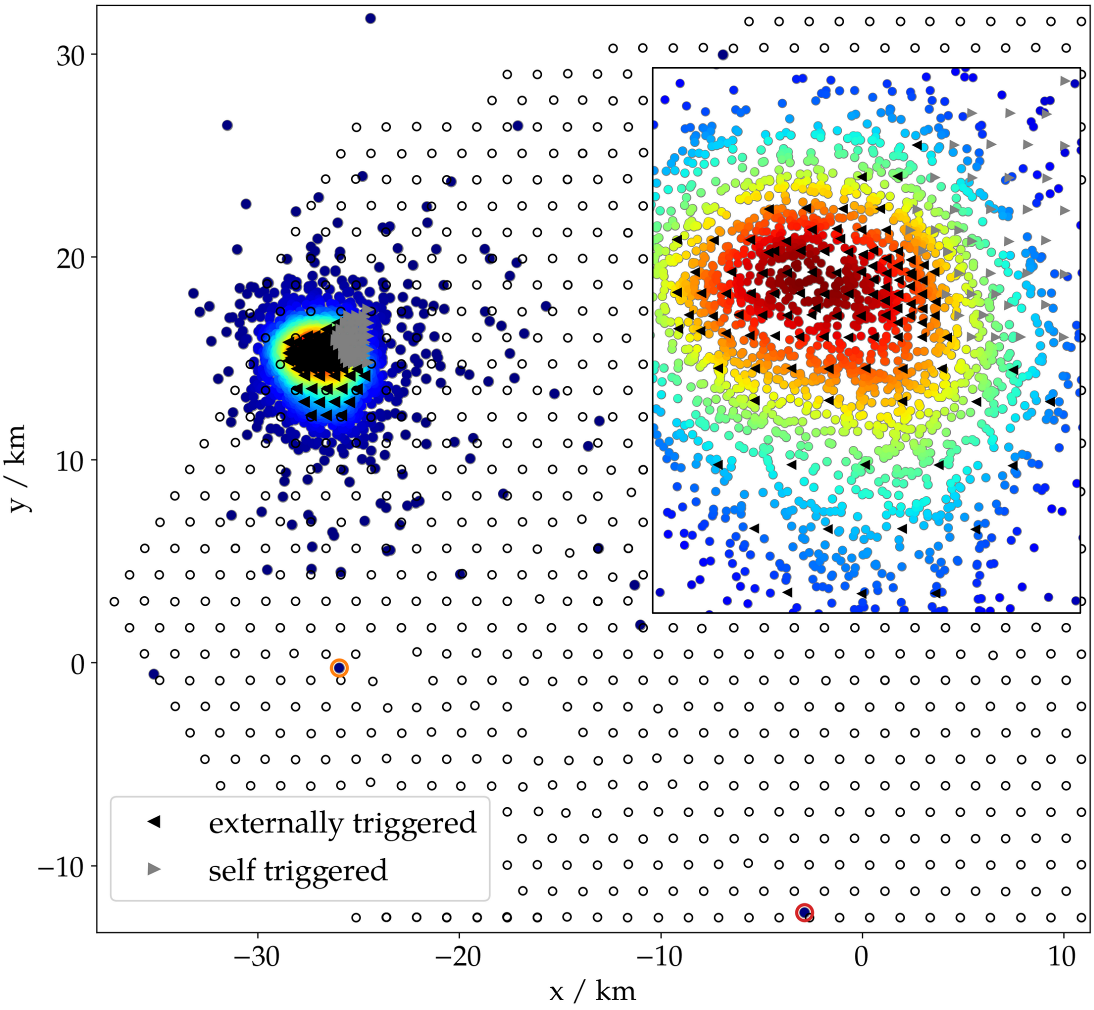

Figure 6.7: Position of the shower core as reconstructed with the SD. The color denotes the density determined with a KDE (blue: low, red: high). The red circle denotes the event where the shower core is furthest away from AERA (see text), the orange circle denotes the event shown in Fig. 4.3. The inset figure shows a zoom onto AERA.

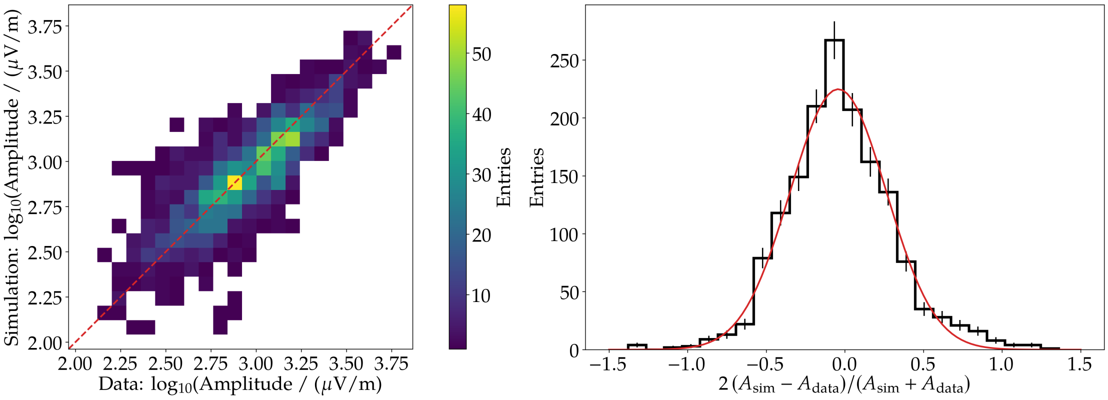

Figure 6.8: Correlation of the peak amplitudes of measured data and CoREAS simulations for the subset of events with a reconstructed SD energy. The left figure shows a two-dimensional histogram of the data with identity denoted by the red dashed line. In the right figure the one-dimensional projection normalized to the mean amplitude is shown. The red line shows a fit of a normal distribution.

The big radio footprints allow for a successful detection and reconstruction with a sparse grid of radio antennas. The potential of such a grid with a spacing of 1.5 km, similar to the spacing between the SD stations of the Pierre Auger Observatory, will be shown in section 6.6.

6.4 Comparison with CoREAS simulations

The 117 events with a reconstructed SD energy are simulated with CoREAS using the reconstruction of the Surface Detector as input. Only proton primaries are simulated to obtain maximal shower-to-shower fluctuations, the impact of heavier primary particles on the radio emission was found to be below 10 % and thus smaller than the uncertainty of the SD energy scale and the antenna calibration [75]. A detailed radio detector simulation is performed, including the addition of measured noise from the time of the event. Afterwards, data and simulations are analyzed similarly. For 80 of the simulated events the reconstruction with $\overline{\text{Off}}\underline{\text{line}}$ is successful. The simulated events without a successful $\overline{\text{Off}}\underline{\text{line}}$ reconstruction did likely not generate an SD event trigger, hence, no radio event reconstruction is performed.

For stations where the measured signal exceeds the signal-to-noise ratio of 10 in the data event and the simulation the amplitudes of the electric field are compared. For every simulated event the amplitudes are compared for at least 3 stations, the maximum number of stations amounts to 63. In total, this results in 1574 stations in the comparison that are shown in Fig. 6.8. There is a clear correlation, but also a significant scatter. On average, the simulations underpredict the measured amplitudes by 3 % with a spread of 34 %. The large spread is predominantly caused by the uncertainty of the reconstructed SD energy and the estimated shower core which are both important inputs in the CoREAS

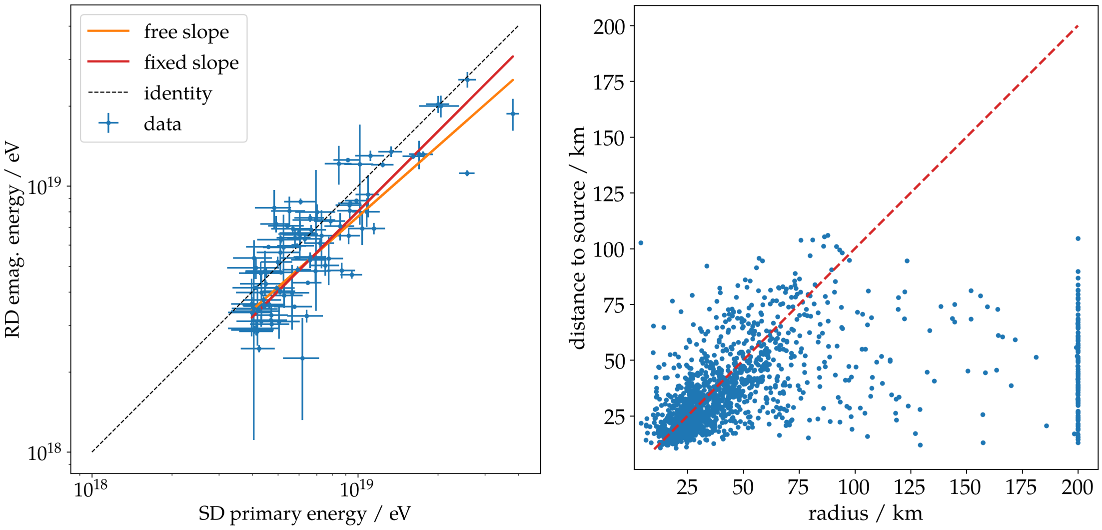

Figure 6.9: Comparison of reconstructed energy (left) and distance to the source of the radio emission (right). The electromagnetic energy of AERA is compared to the primary energy reconstructed by SD. A power law is fitted, once with a fixed slope of unity, and once with the slope as a fit parameter. The source distance is compared to the radius of the spherical wavefront fit, the red line denotes identity.

simulation. An optimized radio reconstruction of inclined air showers, i.e. with the `RdHASLDFFitter`, likely yields a more precise estimation of both quantities than the SD. Hence, using the radio reconstruction as MC input can improve the comparison further.

6.5 Quality of the LDF model for inclined air showers

The preliminary version of the `RdHASLDFFitter` has not yet been tested on actual AERA data. Before evaluating the composition sensitivity in the following chapter the overall quality of the radio reconstruction is analyzed first. For the selected dataset the `RdHASLDFFitter` shows a high reconstruction efficiency of 75 %, 1571 out of 2085 events are fitted successfully[4]. Without quality cuts on the radio reconstruction the average uncertainty of the reconstructed electromagnetic energy is estimated as 20 % with a spread of 18 %. The accuracy improves with the number of signal stations, e.g. for events with more than 50 signal stations the mean uncertainty amounts to only 5.8 %.

On the subset of events with a reconstructed SD energy 93 out of 117 events are fitted successfully. A clear correlation of both energy reconstructions is shown in Fig. 6.9. Fitting a power law yields a slope of 0.882 ± 0.007. As the statistics is small the uncertainty is also estimated using the bootstrapping technique. For 1000 random sub-samples of the full data sample, each containing 80 % of the data, the distribution of the slopes yields a mean

---

[4] The actual reconstruction efficiency is even higher. For technical reasons the fit is rejected if the relative uncertainty on the distance to $X_{\max}$ is bigger than 100 % as this can lead to an abnormal termination of the $\overline{\text{Off}}\underline{\text{line}}$ run when calculating uncertainties of derived quantities.

value of 0.91 and a standard deviation of 0.13. Thus, the results are in agreement with a slope of unity, fixing the slope to unity results in a fit that has an almost equal χ^2/ndf value.

With the `RdHASLDFFitter` the electromagnetic energy of the air shower is reconstructed whereas the SD estimates the primary energy. Therefore, an offset of the fit from the identity line is expected. A normal distribution is fitted to the distribution of the ratio of the reconstructed SD and RD energies. The fit yields a mean ratio of 1.10, which agrees with the prediction of the *RdHasLib* as shown in section 4.5, and a standard deviation of 0.32. The uncertainty of the radio energy scale can be estimated from the standard deviation of the distribution. Assuming that both energy estimators are uncorrelated and given the SD resolution of 19.3 % [70] an uncertainty of 25.5 % is found for radio. This value is likely to improve by adding quality cuts on the radio reconstruction.

Another interesting quantity that is reconstructed with the `RdHASLDFFitter` is the distance to the hypothetical point source that is located close to X_{max}. This distance is also estimated by the radius of the spherical wavefront fit. Both estimators are compared to each other in Fig. 6.9 for the subset of 1571 events that have a spherical wavefront and an LDF fit. The radius can exhibit large relative uncertainties up to a factor of 10. In contrast, the estimated distance of the LDF fit can have very low uncertainties on a sub-percent level. Within the wavefront fit the radius is limited to values below 200 km. Ignoring the 104 events where the fitted radius is at the allowed limit results in a correlation coefficient $\varrho = 0.54$ for both estimators. The correlation increases a lot by rejecting events with a large relative uncertainty of the radius δR, e.g. $\varrho = 0.72$ for $\delta R < 1$ and $\varrho = 0.83$ for $\delta R < 0.3$.

Despite still being in a development stage the `RdHASLDFFitter` is capable of reconstructing the energy as well as the distance to the hypothetical point source of the radio emission.

6.6 Prospects of a sparse radio grid

The radio detection of air showers has shown a potential to be feasible even with a sparse antenna array, similar to the spacing of the SD station, as the radio emission illuminates areas of dozens of km^2 on ground. Such an array is mimicked by thinning out AERA to a mere 5 (AERA124) or 10 (AERA153 after 2 March 2015) radio stations on an approximate 1.5 km grid as shown in Fig. 6.10. This can be interpreted as a small prototype array for the AugerPrime Radio Detector. Due to the small size of AERA the performance of sparse AERA will not be compatible as the radio footprints will be truncated. The previous analysis is partially repeated on the same data sample using only the 5 or 10 selected radio antennas.

313 events are reconstructed in total. As before, the opening angle between the SD and sparse AERA shower axis is calculated for all events within 60° and 80°, that are not inside a thunderstorm period. The maximum allowed opening angle is estimated as $(2.02 \pm 0.27)^\circ$. Since this is compatible with the opening angle that was determined for AERA the maximum opening angle of 2.08° is used for the sparse AERA as well. The number of events after each cut is given in Tab. 6.2. Finally, 157 events are selected.

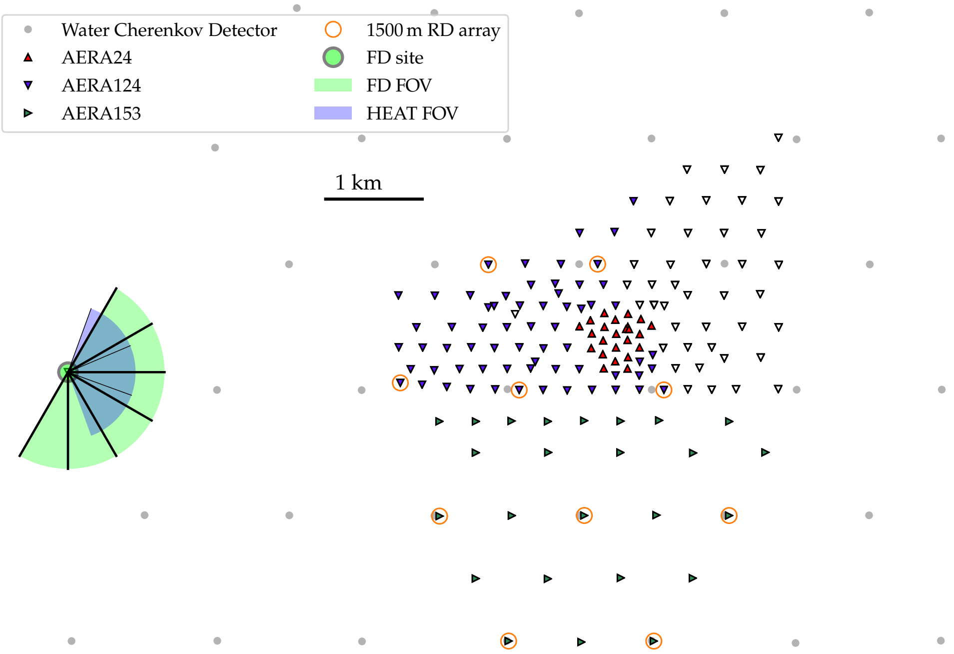

Figure 6.10: Schematic map of AERA similar to Fig. 3.4. The selected antennas on a 1.5 km grid are marked by orange circles.

Table 6.2: Number of events surviving the individual cuts, starting with a total number of 313 events.

cut	number of events after cut
$\theta_{\mathrm{SD}} \geq 60°$	312
$\theta_{\mathrm{SD}} \leq 80°$	218
no thunderstorm	191
SD-RD opening angle $< 2.08°$	157

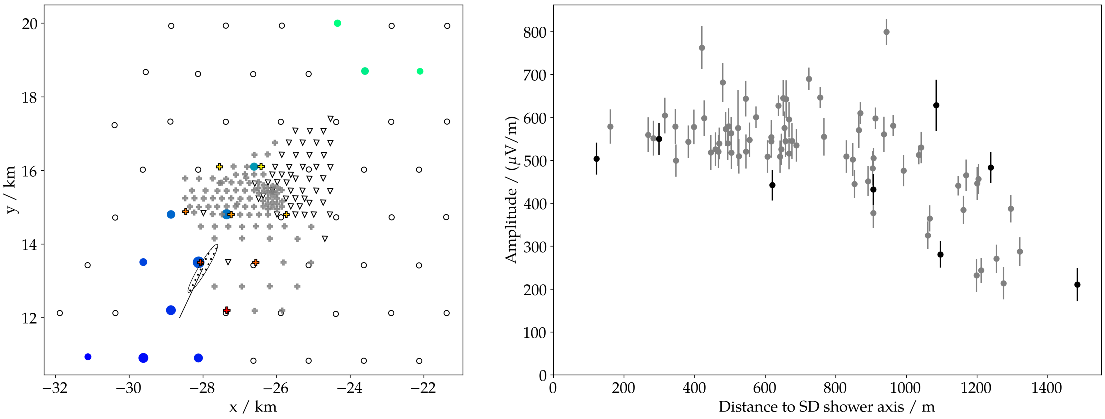

Figure 6.11: Example event with the radio ID 101302.148879 reconstructed with sparse AERA. Shown is an overview of the AERA stations (left, cf. Fig. 4.9 for an explanation of all symbols) and the raw lateral distribution of the radio signal (right). Black points denote sparse AERA, for comparison the AERA event is shown in gray. Note that the LDF is not corrected for known asymmetries.

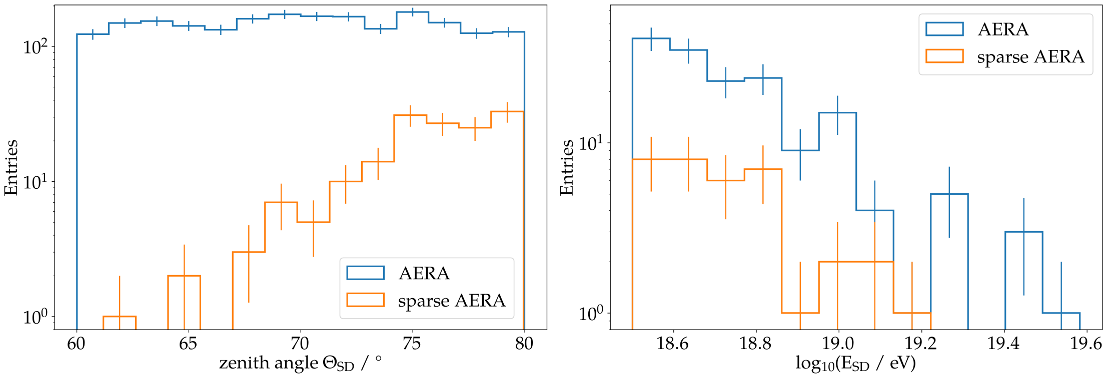

Figure 6.12: Distribution of the reconstructed zenith angle (left) and energy (right) for sparse AERA compared to AERA. Poissonian uncertainties are shown for each bin.

The event with the highest number of signal stations, i.e. 8 radio stations, is shown in Fig. 6.11. The SD zenith angle is reconstructed as $(79.6 \pm 0.2)°$ with an azimuth angle of $(244.7 \pm 0.2)°$. No energy is reconstructed by the SD, with sparse AERA an electromagnetic energy of ~3 EeV is reconstructed. The raw signal distribution is shown for the sparse AERA antennas and the full array. Even with the sparse AERA a reasonable sampling of the LDF is achieved. The reconstructed radiation energies, as determined by the `RdHASLDFFitter` for both arrays, differ only by 7 % and agree within their uncertainties.

The expected North-South asymmetry is visible also for the reconstructed sparse AERA events (not shown here). A comparison of the reconstructed zenith angles and energies of the SD is shown in Fig. 6.12. The zenith angle distribution shows a steep

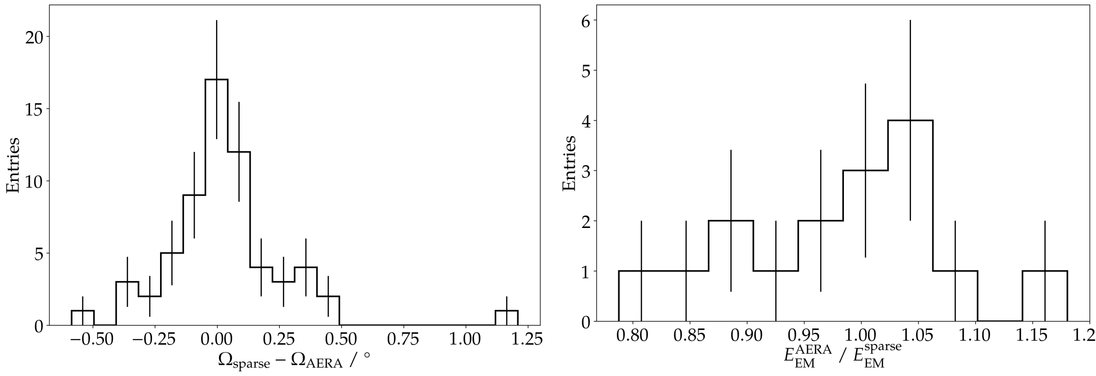

Figure 6.13: Comparison of the opening angle, Ω, (left) and energy reconstruction (right) using AERA and sparse AERA.

increase in event number for events above ~73°. At lower inclination the footprint is still too small to trigger enough stations of the sparse AERA. The threshold is expected to be around 70° for the AugerPrime Radio Detector due to the increased instrumented area [59]. For 27 events the SD has a reconstructed shower energy. As the energy only has a minor impact on the footprint size no significant difference is found for both antenna configurations.

The accuracy of the radio reconstruction of sparse AERA is compared to the results obtained with AERA. Selecting the subset of common events that are reconstructed with a spherical wavefront results in 63 events. For both radio reconstructions the opening angle with the (identical) SD shower axis is calculated, their difference is shown in Fig. 6.13 (left). On average, the opening angles increase by 0.03° for sparse AERA, which is only a minor loss in directional accuracy. Only four sparse AERA events have a reconstructed SD energy. Therefore, the reconstructed electromagnetic energy of sparse AERA is compared to the one reconstructed with AERA. This results in 16 common events as shown in Fig. 6.13 (right). The comparison shows no bias, the mean ratio is estimated as 0.98 with a spread of 0.10. As the radio reconstruction is designed for inclined air showers the comparison is extended to zenith angles beyond 80°. This results in 38 events confirming the results.

As noted before, the radio footprint of very inclined air showers exceeds the instrumented size of AERA by far. To illustrate the true footprint size in the case of the AugerPrime Radio Detector, a measured AERA event is simulated with CoREAS. The MC input – energy 2.9 EeV, zenith angle 82.6° and azimuth angle 277.4° (7° East of South) – is taken from the SD reconstruction and SD stations with an axis distance smaller than 3 km are used as antenna positions, cf. Fig. 6.6 for the typical size of the radio footprint. The radio reconstruction is designed to reconstruct air showers with zenith angles above 80° and the SD reconstruction can be extended up to 84° as used in [75, 108]. With further optimization of the SD reconstruction such an air shower will be reconstructed with Offline. The simulation is reconstructed with Offline without additional noise on the radio traces. In Fig. 6.14 the simulated radio event is plotted

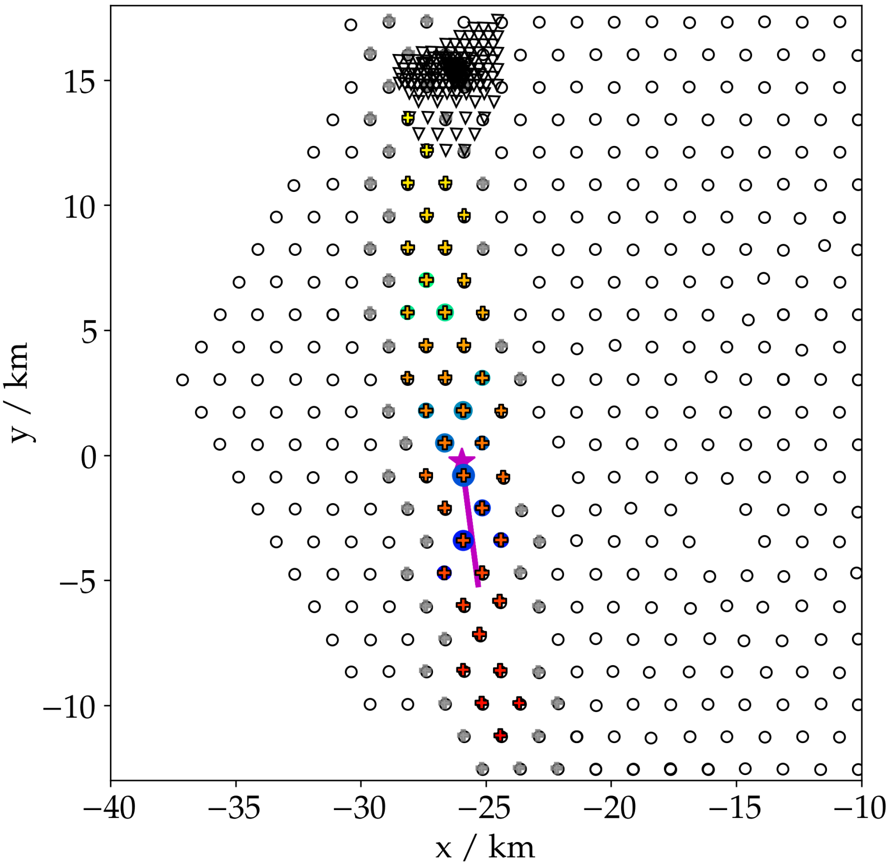

Figure 6.14: Example event for the AugerPrime Radio Detector. Colored circles indicate the real SD event, colored plus markers denote simulated antennas at each SD station. Gray plus markers denote antennas that were simulated but do not exceed the minimum signal for a reconstruction. The empty triangles show the position of the AERA antennas, they were not included in the simulation. The MC core and axis are denoted in magenta.

together with the measured particle event[5]. In total 40 antennas detected a signal above the standard minimal signal threshold with a peak amplitude above 100 μV/m. The size of the radio footprint exceeds the size of the particle footprint by far.

The current data acquisition of the stations requires a trigger from WCD to read out the recorded radio trace. Thus, the data of antennas far away from the shower axis, where there are not enough particles left to generate a local SD trigger, but still a detectable radio signal is present, will be lost. For this event, only 13 of 40 stations with a radio signal will be read out. In the future it can be worth to also include the radio signal in the triggering algorithm and e.g. lower the SD trigger conditions if a radio signal is present.

---

[5] Due to the muon deficit in simulations the simulated particle events will not match the measured event.

The found results are encouraging the proposition that an accurate radio reconstruction on a 1.5 km grid is feasible. The large radio footprint of inclined air showers on ground can be detected with such a sparse radio array and the existing reconstruction methods are able to yield a precise reconstruction of the shower direction and the primary energy. These results have been a key ingredient for the founding application of the AugerPrime Radio Detector.

7 Hadronic Shower Development and Composition Analysis

By a coincident detection of an air shower with the SD and AERA the muon deficit in simulations as well as the mass of the primary particle can be estimated. The potential of both analyses is shown in this chapter. As both analyses are important science cases for the AugerPrime Radio Detector this work is crucial to demonstrate their feasibility.

For the analysis of the muon deficit an energy estimation is needed that is independent of the muon number. In previous analyses this was realized by hybrid FD-SD events [71] and hybrid SD-MD events [118]. Here, the electromagnetic energy, E_{EM}, of the air shower is estimated with AERA using the recently developed `RdHASLDFFitter`, cf. section 4.4.5, and the muon number, R_μ, with the SD, cf. chapter 4 for details on both estimators.

An estimation of the mass of the primary particle is closely related to the analysis of the muon deficit. An air shower that is induced by a heavier particle (iron) contains more muons and fewer electrons than an air shower induced by a lighter particle (proton) [11]. This approach was already tested successfully for vertical air showers by combining the electromagnetic measurement of AERA and the muonic measurement of the MD [7, 119]. In this chapter the same approach will be used to estimate the composition of inclined air showers by combining measurements of AERA and the SD. The electromagnetic component is estimated by the corrected radiation energy S_{rad} (cf. section 4.4) and the muonic component by R_μ. Comparing the ratio of both observables to predictions obtained with the *RdHasLib* (after correction of the muon deficit) allows estimating the mass of the primary particle.

7.1 Sampling criteria for the radio LDF

The `RdHASLDFFitter` describes the lateral distribution of the energy fluence with an exponential function of a cubic polynomial, i.e.[1]

$$f(r) = A \exp\left(-b\,\frac{r}{r_0} + e^c \left(\frac{r}{r_0}\right)^2 - e^d \left(\frac{r}{r_0}\right)^3\right). \tag{7.1}$$

In this equation b, c, and d are parameterized based on the distance to X_{max}. The distance and A are fitted, r_0 is a fixed reference distance of 800 m. The LDF model exhibits two main features as shown in Fig. 7.1, the maximum energy fluence at the Cherenkov ring and the location of the two inflection points. These locations can be used to derive

---

[1] The terms e^c and e^d are used to enforce a positive coefficient for the quadratic and cubic term of the polynomial.

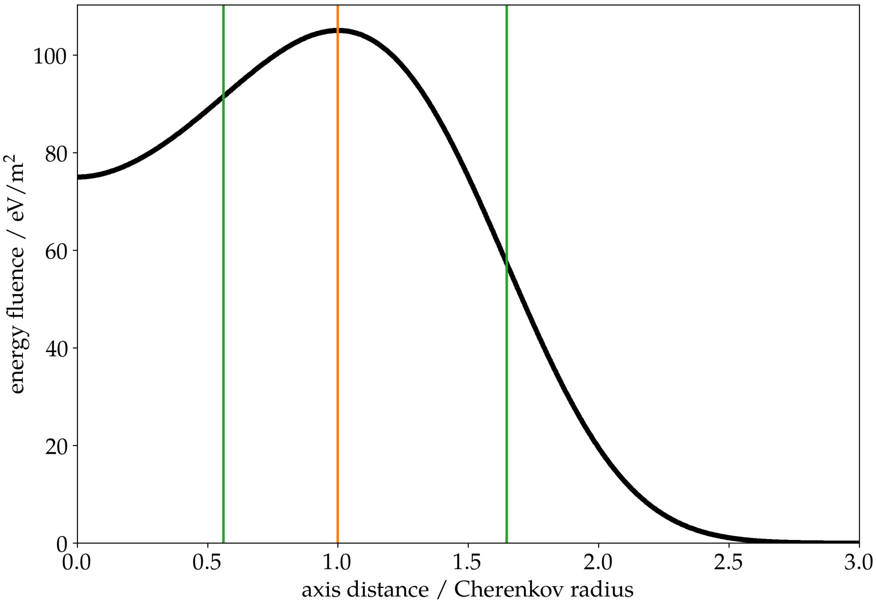

Figure 7.1: Sketch of the LDF model, Eq. (7.1), for inclined air showers. Beyond three Cherenkov radii no radio signal above the noise level is detectable. The orange line denotes the axis distance of the maximal energy fluence at the Cherenkov radius, the green lines indicate the locations of both inflection points.

conditions on the sampling of the LDF such that the fit yields a reliable reconstruction. The position of the maximum, i.e. the Cherenkov radius, can be calculated analytically and is given via

$$r = r_0 \frac{\sqrt{e^{2c} - 3b\, e^d} + e^c}{3e^d}. \tag{7.2}$$

For the inflection points the second-order derivative is calculated analytically:

$$\frac{d^2 f}{dr^2} = A \exp\left(-\frac{e^d\, r^3}{{r_0}^3} + \frac{e^c\, r^2}{{r_0}^2} - \frac{br}{r_0}\right)\left[\left(-\frac{3e^d\, r^2}{{r_0}^3} + \frac{2e^c r}{{r_0}^2} - \frac{b}{r_0}\right)^2 + \frac{2e^c}{{r_0}^2} - \frac{6e^d r}{{r_0}^3}\right], \tag{7.3}$$

its roots are estimated numerically. The first inflection point is typically located at ~0.56 Cherenkov radii, the second one at ~1.65 Cherenkov radii.

For a reliable reconstruction it is required to sample all features of the LDF precisely. Ideally there should be at least one signal station before the first inflection point, between the first inflection point and the maximum, between the maximum and the second inflection point, and beyond the second inflection point[2]. For AERA events this is a challenging criterion as the array is rather small and lots of events have their core outside the instrumented area such that there are no stations closer than the first inflection point. Furthermore, a station close to the shower axis is likely saturated for high-energy air

---

[2] Similar idea as in [120], just using the location of the inflection point rather than arbitrary fractions of 0.5 and 1.5 Cherenkov radii.

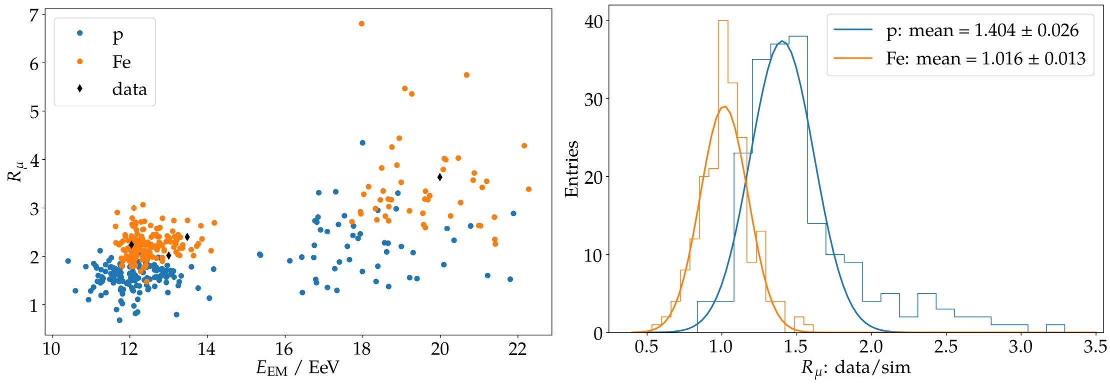

Figure 7.2: Muon deficit with dedicated simulations for four selected events. Scatter plot of R_μ and the electromagnetic energy (left) and histogram of the ratio of R_μ in data and simulations (right). The distributions are fitted with a Gaussian, the proton distribution has a long tail and is not ideally described by a Gaussian. Note the different binning of the histograms.

showers, cf. appendix B. Therefore, the condition is mitigated and only one signal station inside the Cherenkov ring is demanded.

7.2 Muon deficit in simulations

In a first step, the muon deficit is analyzed using dedicated CoREAS simulations of four selected high-quality measured AERA events with energies above 10 EeV (same events as in section 7.3, cf. Tab. 7.1). For each event, 50 proton and 50 iron showers are simulated. The SD geometry is used as input for the MC. The energy is chosen such that the proton and the iron simulation are expected to have a similar electromagnetic energy as the data event. For this, the E_{EM} as reconstructed with the `RdHASLDFFitter` is multiplied with the scaling factors determined with the *RdHasLib* in section 4.5, 1.11 for a proton primary and 1.17 for an iron primary, to obtain the primary energy.

The simulations are processed with the standard reconstruction in $\overline{\text{Off}}\underline{\text{line}}$. The reconstructed E_{EM} and R_μ are shown in Fig. 7.2 for all four events. Both observables show significant scatter originating from shower-to-shower fluctuations of the simulations and the reconstruction uncertainty. As desired, the reconstructed E_{EM} agrees for all three types of events, the data event is well surrounded by the corresponding event simulations. The muon number in data is in good agreement with the prediction of the iron simulations, for the proton simulations the predicted R_μ is typically lower than in data.

Since the data event and the corresponding simulations have roughly the same electromagnetic energy one can in first order simply calculate the ratio of R_μ in data and simulations for each event individually. The histogram (cf. Fig. 7.2) shows the concatenated ratio of all four events. On average, the R_μ of the iron simulations agrees to the data reconstruction, a fit of a Gaussian function yields a mean value of 1.016 ± 0.013. For the proton primary a mean value of 1.404 ± 0.026 is obtained. Hence, the simulations

Table 7.1: Number of events surviving the individual cuts, starting with a total number of 3484 events. Cuts denoted with a $^{(*)}$ are the standard SD selection of inclined events. Numbers in parentheses correspond to a minimal energy of 10 EeV.

cut	number of events after cut	
$\theta_{\mathrm{SD}} \geq 60^\circ$ $^{(*)}$	3017	
$\theta_{\mathrm{SD}} \leq 80^\circ$ $^{(*)}$	2656	
number of candidate stations ≥ 5 $^{(*)}$	1403	
rec level ≥ 3 $^{(*)}$	1403	
T4Trigger ≥ 2 $^{(*)}$	1402	
T5Trigger ≥ 3 $^{(*)}$	1219	
$E_{\mathrm{SD}} > 10^{18.6}$ $^{(*)}$ $(10^{19.0})$	141	(27)
no thunderstorm	127	(23)
SD-RD opening angle $< 2.08^\circ$	117	(19)
HAS LDF fit	93	(16)
station inside Cherenkov radius	58	(4)

would be consistent with measured data assuming that the primary particle is an iron nucleus. This is however not in agreement with independent composition estimation inferred from measurements of $X_{\max}$ with the FD. In this energy range the composition is expected to be dominated by primaries with an atomic mass number A between 2 and 22 [14] as shown in Fig. 2.4. The results are therefore interpreted as an indication of a muon deficit in simulations.

This rather simple approach can be further optimized by using CONEX [121]. With CONEX, the cascade equations that describe the shower development after the very first interactions are solved numerically. This can be used to prepare CORSIKA simulations that produce exactly the desired electromagnetic energy and hence remove the shower-to-shower fluctuation from the comparison. However, running these event-based simulations is a massive CPU effort that is unfeasible for a large data sample. In a second approach the muon number of data events is compared to the MC prediction obtained from event-independent simulations.

The data sample presented in the previous chapter is used to analyze the muon deficit. The standard SD event selection of inclined air showers is applied to ensure a proper reconstruction of the SD event. Events that are within thunderstorm periods and events with an opening angle between the SD and the RD shower axis greater than 2.08° are rejected, cf. section 6.1. This amounts to 117 events of which 93 events are fitted successfully with the `RdHASLDFFitter` and 58 events have a signal station inside the Cherenkov ring. The number of events after each cut is summarized in Tab. 7.1, the strongest cut is the minimum energy of 4 EeV.

The data reconstruction is compared to predictions obtained with the *RdHasLib*. For the simulations, the predicted R_μ is obtained by a bias-removing conversion from the N_{19} of the SD reconstruction, cf. section 4.2. Here, the MC true E_{EM} is used as it is a

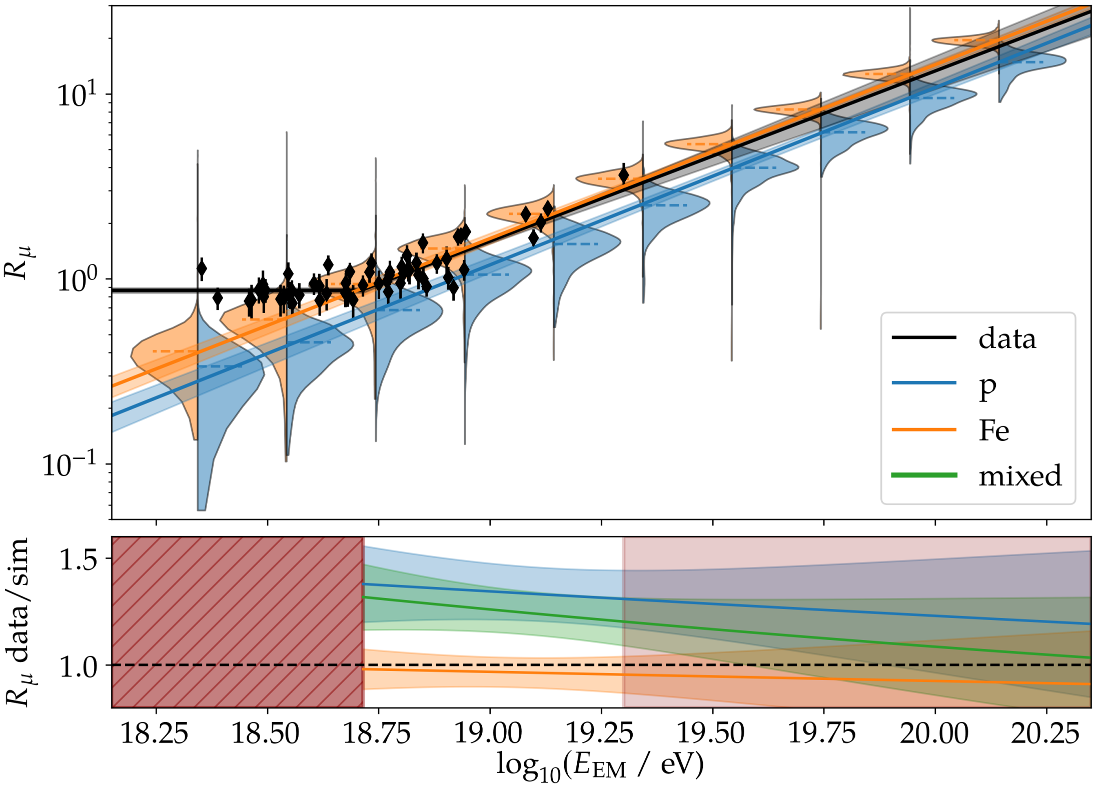

Figure 7.3: Muon content R_μ as a function of the electromagnetic energy E_{EM}. The violins denote the full distribution of the reconstructed R_μ for each of the discrete energy bins of the *RdHasLib*. The mean R_μ of each energy bin is indicated by the dashed line inside of the violin. The solid line shows the fit of a power law (MC) and a min(const, power law) (data), the colored bands denote the fit uncertainty. In the bottom frame, the ratios of the fits are shown. The hatched red area indicates the energy range before the data fit is in the power-law energy region, the light-red colored region indicates the energy range above the highest energy data event.

direct output of CORSIKA, hence no radio reconstruction is performed. The specific radio-related features of the *RdHasLib* are therefore not important in this study, any big library of MC simulations could be used. No event selection is applied for the MC.

The results are shown in Fig. 7.3. The mean value and standard derivation of each of the discrete energy bins of the *RdHasLib* is used to fit a power law for both primaries. The fits are then used to compare the R_μ of the data event to the MC prediction. The data R_μ is constant at lower energies and then follows a power-law function. Hence, the data is fitted with

$$R_\mu(E_{\mathrm{EM}}) = \min\left(c, a \cdot (E_{\mathrm{EM}}/10^{19}\,\mathrm{eV})^b\right), \tag{7.4}$$

where c describes the constant value at lower energies and a, b denote the scale factor and exponent of the power law. The fit results are summarized in Tab. 7.2. The data

Table 7.2: Results of the power law fit of Fig. 7.3 for each parameter p, the results of [71] (PRD) are stated for comparison.

			data		
p	proton	iron	fit	bootstrap	PRD
a	1.19 ± 0.11	1.65 ± 0.11	1.60 ± 0.05	1.59 ± 0.11	$1.841 \pm 0.029 \pm 0.324$ (sys.)
b	0.96 ± 0.05	0.94 ± 0.03	0.92 ± 0.08	1.01 ± 0.20	$1.029 \pm 0.024 \pm 0.030$ (sys.)
c	–	–	0.866 ± 0.027	0.88 ± 0.04	–

shows a constant value up to $E_{\text{EM}} = 10^{18.72}$ eV that is not present in the MC. This is an event selection effect, only the upward fluctuating events pass the energy threshold in the SD event selection. A similar behavior is found in MC when using the same event selection.

31 data events are within the power-law region of the fit. The fit result is compared to an independent analysis based on 171 hybrid SD-FD events [71]. There, R_μ was fitted as a function of the total energy $E = E_{\text{cal, FD}} + E_{\text{inv}}$ (cf. section 4.3) with a similar power-law function. The fit result is stated in Tab. 7.2 as well. As N_{19}, and hence also R_μ, is expected to increase linearly with energy the exponent b is in agreement with unity for both analyses. For the comparison of a, i.e. the relative number of muons at an (electromagnetic and total, respectively) energy of 10 EeV, the energies have to be converted.

For the conversion a mixed composition is used that matches the mean atomic mass number, $\langle \ln A \rangle$, as measured by the FD [13]. In this energy range, the iron fraction is described via [122]

$$f_{\text{Fe}} = 0.25 \cdot \log_{10}(E/\text{eV}) - 4.54, \tag{7.5}$$

the average value is calculated as 0.24. Consequently, the proton fraction is given by $1 - f_{\text{Fe}} = 0.76$. For the mixed composition the mean(standard deviation) of $E_{\text{CR}}/E_{\text{EM}}$ is determined as 1.12(0.02) by the weighted average of protons, 1.11(0.02), and iron primaries, 1.17(0.03), cf. section 4.5. Assuming that this number also holds for data[3], the conversion of a yields

$$a' = a \cdot 1.12^b = 1.78 \pm 0.06, \tag{7.6}$$

which is only a 4 % difference between this analysis and [71]. Furthermore, both results are compatible within their uncertainties.

In this analysis, the measured R_μ values are described by a power law for electromagnetic energies above $10^{18.72}$ eV, corresponding to primary energies above ~6 EeV, and a constant value for lower energies. No constant part of R_μ is found in [71], the data immediately follows a power law for primary energies above 4 EeV. The observed difference of the start of the power law may be related to a difference of the RD and FD energy scales. Here, the radio reconstruction is calibrated with MC, no cross-calibration

---

[3] The data driven correction for the missing invisible energy E_{inv}, i.e. [73], can not be used here as it is based on the calorimetric energy and not the electromagnetic energy of the air shower.

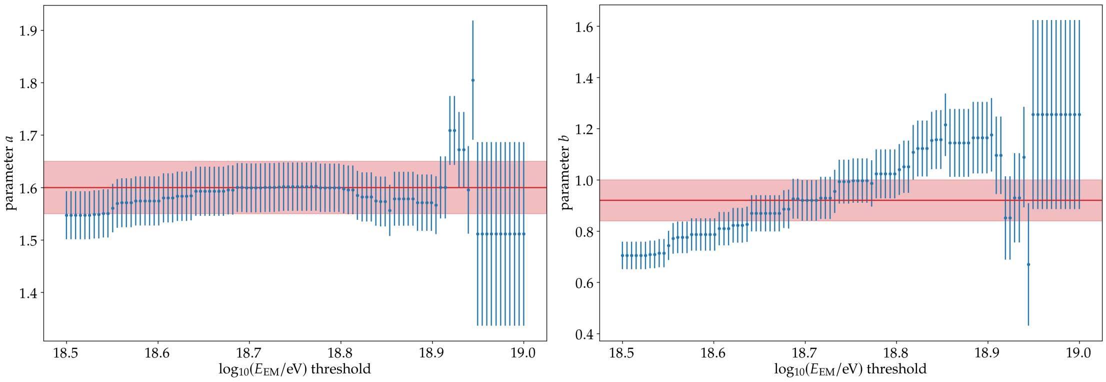

Figure 7.4: Results of a power-law fit of all data events with an electromagnetic energy above the selected threshold value. The results obtained from the fit of Eq. (7.4) that correspond to an energy threshold of $E_{\rm EM} = 10^{18.72}$ eV are shown in red.

with the FD energy scale is performed yet. An increase of the RD energy scale by ~19 % with respect to the FD energy scale was already found before [123], further investigations are needed to clarify this.

The ratios of the fits obtained for data and each of the two MC primaries (bottom frame in Fig. 7.3) reveal that the data R_μ is in agreement with the prediction of iron MC, as already found in Fig. 7.2. An average rescaling factor m is calculated for the energy range from the start of the power law at $E_{\rm EM} = 10^{18.72}$ eV up to the event with the highest energy of $E_{\rm EM} = 10^{19.30}$ eV. This yields $m = 0.97$ for iron primaries and $m = 1.34$ for protons. For a precise estimation of m the type of the primary particle in data has to be known. This can be estimated from the 4-component fit of the Auger data performed e.g in [14]. Here, the mixed composition of protons and iron primaries matching the measured $\langle \ln A \rangle$ is used as reference. This amounts to $m = 1.25$, i.e. an increase of R_μ by 25 % in MC for QGSJetII-04.

As the mixed composition is getting heavier with energy, an energy dependence of m is expected. A trend towards a more iron-like rescaling for higher energies is found, c.f. green line in the bottom frame of Fig. 7.3. However, due to the small energy region of interest in this analysis and the large fit uncertainty originating from the low number of events this trend is not significant.

The stability of the fit is analyzed using bootstrapping. The analysis is repeated with random subsets of 80 % of the data, an event can be selected multiple times in the same subset. The results of the bootstrapping for the direct fit parameters are also listed in Tab. 7.2. The minimum energy for the start of the power law is estimated as $\log_{10}(E_{\rm EM}/{\rm eV}) = 18.74 \pm 0.07$. The rescaling of R_μ with respect to the mixed composition is determined as (27 ± 7) %.

Furthermore, the impact of the energy threshold on the power-law fit is analyzed. Only events above an arbitrary minimal energy are fitted directly with a power law. This minimal energy is scanned within the range of $10^{18.5}$ eV to 10^{19} eV, the impact on the fit parameters is shown in Fig. 7.4. The parameter a is largely independent of the energy

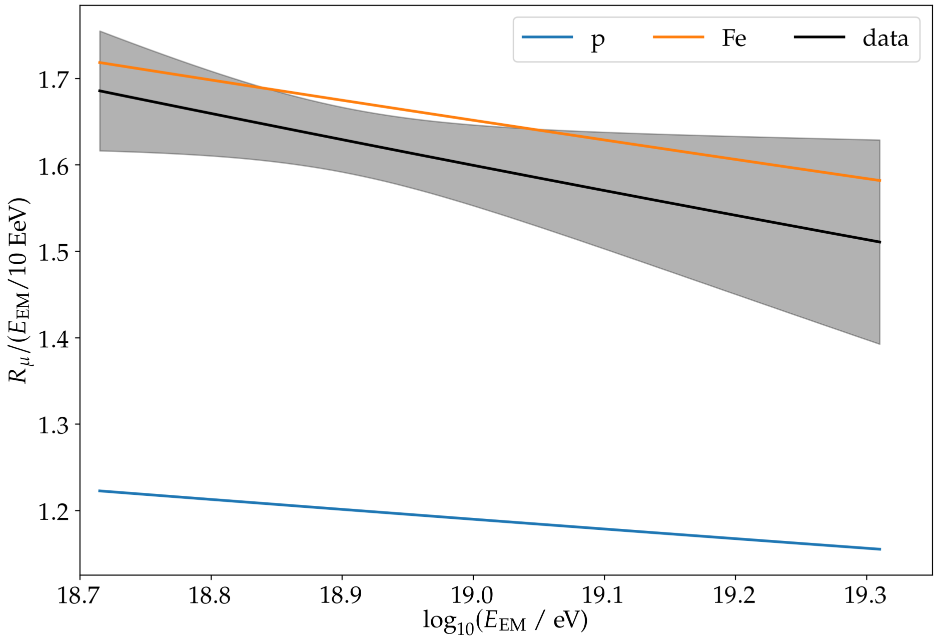

Figure 7.5: Relative number of muons R_μ normalized by the electromagnetic energy E_{EM} as a function of E_{EM} in data compared to the prediction of the *RdHasLib*, i.e. the fit results shown in Fig. 7.3.

threshold, whereas the parameter b shows a continuous steepening of the power law. Including the constant part of the R_μ distribution automatically results in a flattening of the power law. As soon as the threshold is in the power-law region, b is expected to be independent of the energy threshold and should scatter around a constant value. Due to the small event statistics this behavior is not observed here.

The muonic component normalized by E_{EM} is shown in Fig. 7.5 as a function of E_{EM}. The normalization removes the expected scaling of R_μ with energy and thus emphasizes the effect of the primary mass on the number of muons and the deficit of muons in MC. Similar to the bottom frame of Fig. 7.3 one can see that R_μ of the Auger data agrees with the prediction of the *RdHasLib* for iron primaries. A similar result was found in [118] for 1742 hybrid SD-MD events in the energy range from $10^{17.5}$ eV to 10^{18} eV.

7.3 Composition analysis

A first full study of the potential of a composition analysis by combining the particle and radio data was performed in the context of the AugerPrime Radio Detector [59]. For the simulations of the *RdHasLib* the ratio of N_{19} and S_{rad}, precisely:

$$\frac{N_{19}}{\sqrt{S_{\mathrm{rad}}}^{0.93}}, \tag{7.7}$$

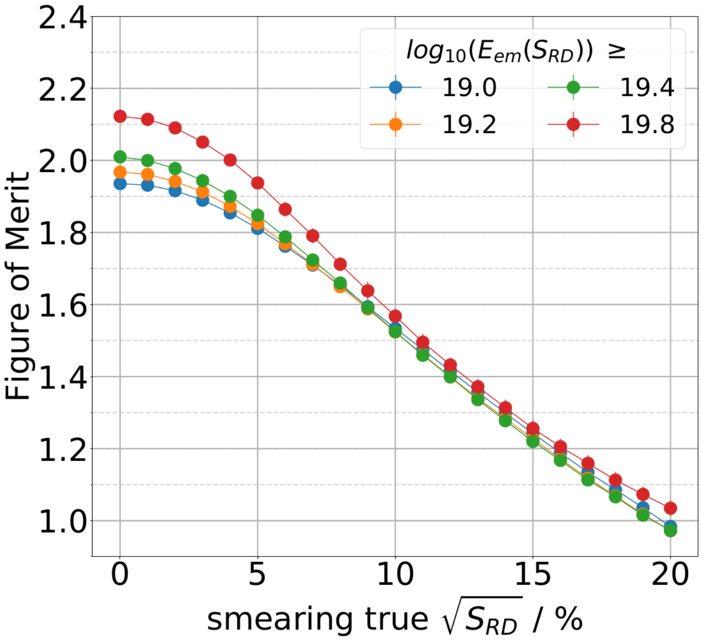

Figure 7.6: Figure of merit for the separation of protons and iron primaries using the ratio of N_{19} and S_{rad} (here: S_{RD}) as defined in Eq. (7.7). Different energy resolutions of the radio detector and energy cutoffs are shown. Figure from [59].

was calculated for proton and iron primaries[4]. The simulations were reconstructed with $\overline{\mathrm{Off}}\underline{\mathrm{line}}$ to obtain the muon content N_{19} of the air shower, as well as the shower direction. As an optimized radio reconstruction for inclined air showers was still under development the true MC radiation energy was calculated and smeared with a normal distribution to mimic the effect of a finite reconstruction resolution. For the calculation of the corrected radiation energy S_{rad} the true MC X_{max} was smeared with a Gaussian with a spread of $100\,\mathrm{g/cm^2}$.

The separation of proton and iron showers is quantified in terms of the *figure of merit*, i.e. the absolut difference of the mean value of both populations divided by their combined spread:

$$\mathrm{FOM} = \frac{|\mu_{\mathrm{p}} - \mu_{\mathrm{Fe}}|}{\sqrt{\sigma_{\mathrm{p}}^2 + \sigma_{\mathrm{Fe}}^2}}. \tag{7.8}$$

The results are summarized in Fig. 7.6 as a function of the assumed energy resolution. For an optimistic scenario of an E_{rad} resolution of 10 %, or the likely scenario of 15 % energy resolution, a figure of merit of ~1.5 or ~1.2 is obtained. For the likely scenario, the figure of merit matches the value predicted for the SSD [12].

The study is partially repeated using R_μ and the geomagnetic radiation energy, as reconstructed with the `RdHASLDFFitter`. To correct for the muon deficit in simulations

---

[4] The exponent 0.93 removes a remaining energy dependence. It depends on the used interaction model and needs to be determined from data for actual data analysis.

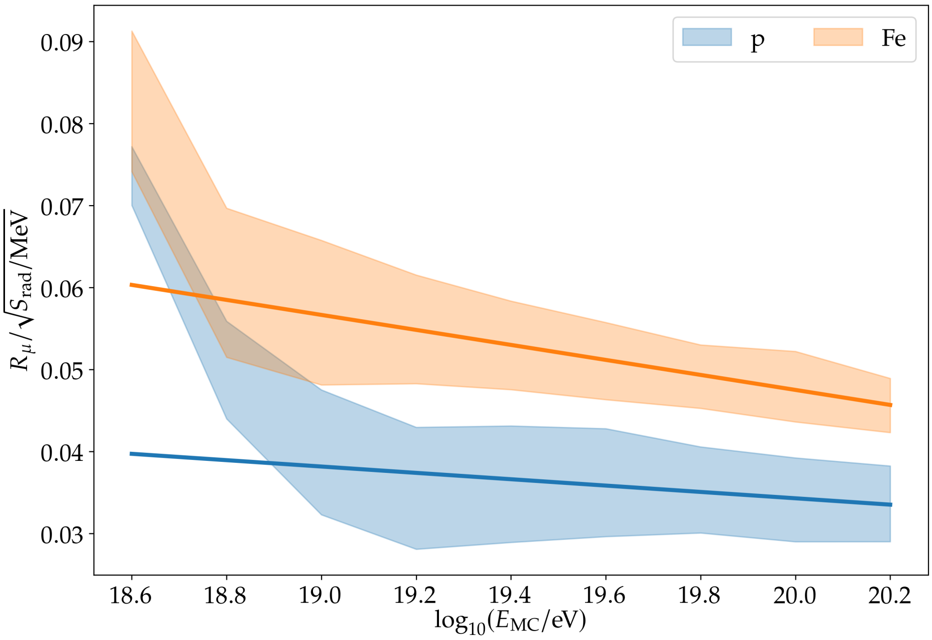

Figure 7.7: Predicted values for the ratio of R_μ and $\sqrt{S_\mathrm{rad}}$ for protons and iron primaries. The width of the band denotes the spread of the distribution for each energy bin. For energies above 10 EeV a power law function is fitted to the predictions.

R_μ is increased by 25 % as derived in section 7.2. The geomagnetic energy fluence is extracted from the total energy fluence as described in Eq. (5.2) and integrated over the full radio footprint. No smearing of the final radiation energy is applied, i.e. an ideal radio detector is assumed. The predicted values of $R_\mu/\sqrt{S_\mathrm{rad}}$ as a function of the MC primary energy, E_MC, are shown in Fig. 7.7, the colored bands denote the 1σ-interval around the mean value. For energies above 10 EeV the proton and iron distributions are well separated. This is in agreement with the results shown before [59].

For air showers with a primary energy below 10 EeV the prediction shows a strong increase of the ratio that is related to the SD reconstruction. At low energies the distribution of R_μ is truncated as only the upward fluctuating events are selected by the SD event selection. Therefore, the mean is shifted to an artificially high value. The effect is emphasized in simulations as the number of muons is underestimated by current hadronic interaction models. Hence, the prediction bands are only valid for air showers above 10 EeV. A linear function is fitted to the proton and iron predictions for these higher energy simulations. In principle, these fits can be used to extrapolate the prediction also to energies below 10 EeV. By comparing the value of $R_\mu/\sqrt{S_\mathrm{rad}}$ for measured events to the fits, the probability of that event being a proton or an iron primary can be inferred.

The previous event selection is tightened to select only events above 10 EeV instead of 4 EeV, the other selection criteria are unchanged. The number of events after each cut is stated in Tab. 7.1. Only 4 events remain after the event selection. For each event 50

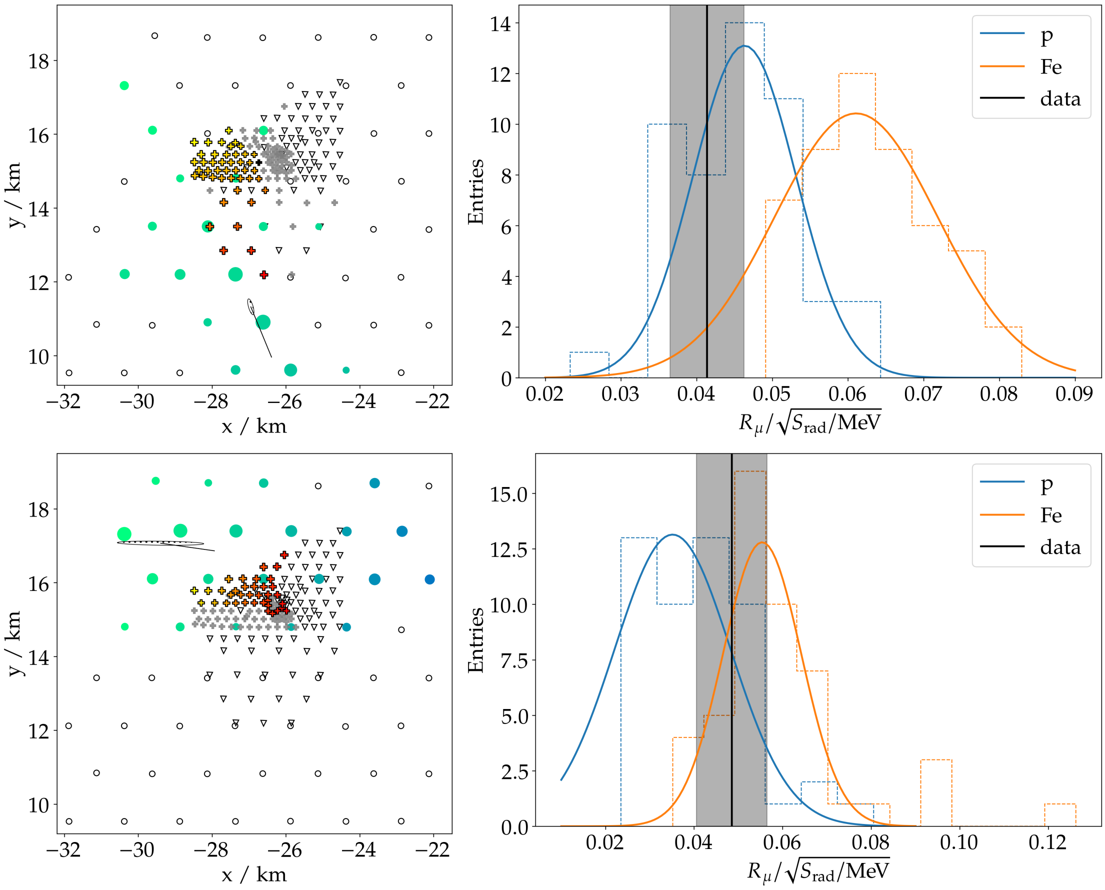

Figure 7.8: Visualization of the hybrid SD-AERA event (left, cf. Fig. 4.9 for an explanation of all symbols) and estimation of the primary mass (right) for the event with the lowest (top) and highest (bottom) SD energy. Further SD stations with a signal are present outside the shown area. A normal distribution is fitted to the MC histograms. The black vertical line indicates the $R_\mu/\sqrt{S_\mathrm{rad}}$ value of the data event, the gray box indicates its uncertainty.

proton and 50 iron primaries are simulated. The primary energies are chosen such that the simulated distributions of the proton and iron primaries describe the measured S_rad value best, cf. section 7.2 for details. The shower direction and core position are taken from the SD reconstruction.

The value of $R_\mu/\sqrt{S_\mathrm{rad}}$ of each event is compared to the prediction of MC, corrected for the muon deficit. For two events, the one with the lowest ($E_\mathrm{SD} = (11.1 \pm 1.4)$ EeV) and highest ($E_\mathrm{SD} = (20.5 \pm 3.5)$ EeV) SD energy, the results are presented in detail. The reconstructed R_μ and E_EM (which is proportional to S_rad) have been shown in Fig. 7.2 already. After the increase of R_μ in MC the data points fall in between the predictions of proton and iron. An overview of both events and the distribution of $R_\mu/\sqrt{S_\mathrm{rad}}$ in MC and the reconstructed value is shown in Fig. 7.8. Both events show a separation of $R_\mu/\sqrt{S_\mathrm{rad}}$

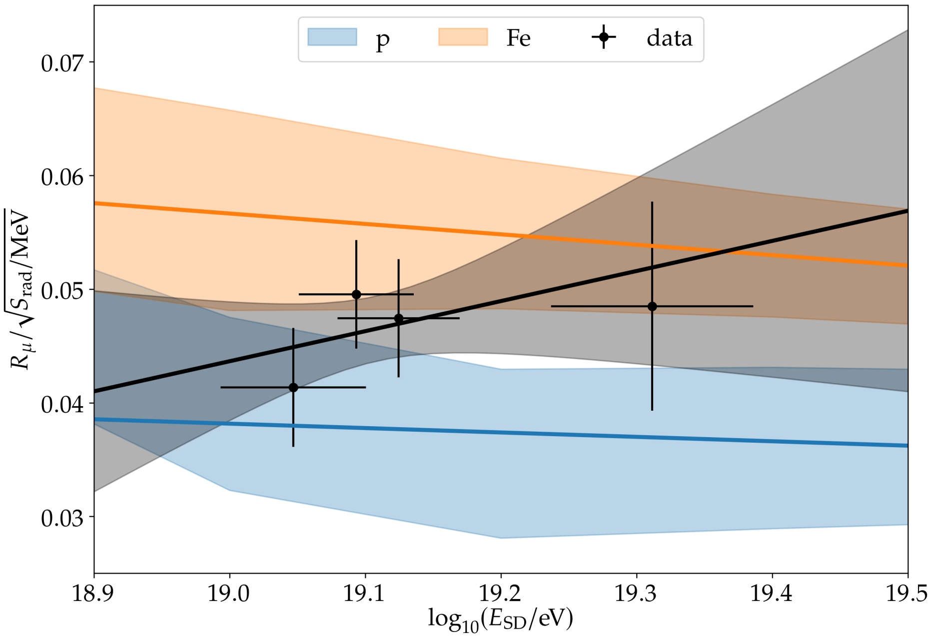

Figure 7.9: Comparison of the predicted value of $R_\mu/\sqrt{S_\mathrm{rad}}$ in MC and the reconstructed ones obtained from measured events. The black line shows a linear fit, the gray band denotes the uncertainty of the fitted line.

for proton and iron primaries. More simulations would improve the description using a Gaussian distribution, they could be realized using CONEX as discussed in section 7.2.

The probability p_Fe to obtain the measured or a smaller value of $R_\mu/\sqrt{S_\mathrm{rad}}$ assuming that the primary particle is iron can be calculated by integrating the *probability density function* (PDF). For the event with the lowest energy p_Fe is determined as $3.4^{+5.1}_{-2.3}\,\%$ and $21.9^{+33.1}_{-17.2}\,\%$ for the event with the highest energy. The asymmetric uncertainties are calculated by integrating the PDF up to the limits of the uncertainty interval of the measured value. The increase of p_Fe with energy shows the expected heavier composition at the highest energies, however, the uncertainties are quite large. For the two other events the following results are obtained: $p_\mathrm{Fe} = 2.0^{+14.0}_{-1.9}\,\%$ at $E_\mathrm{SD} = (12.4 \pm 1.2)\,\mathrm{EeV}$ and $p_\mathrm{Fe} = 10.3^{+15.7}_{-7.3}\,\%$ at $E_\mathrm{SD} = (13.3 \pm 1.4)\,\mathrm{EeV}$.

Instead of running dedicated simulations, the reconstructed $R_\mu/\sqrt{S_\mathrm{rad}}$ can be compared directly to the predictions of the *RdHasLib*. The mean values of the simulated events are always inside the expectation bands that are shown in Fig. 7.7. The data is enclosed by the prediction of proton and iron, bracketing the lightest and heaviest cosmic-ray primaries, as shown in Fig. 7.9. The data points are fitted with a linear function using an *orthogonal distance regression* model that takes uncertainties on the x- and y-values into account. A strong trend towards a heavier composition is found. In general, this trend is in agreement with the expectation from FD measurements of X_max but it is much stronger than expected. A pure iron (or heavier) composition is predicted for energies above $10^{19.3}$ eV. The fit uncertainties are massive as only 4 events are used in the analysis such that a less steep and more reasonable increase of the primary mass is completely consistent with the results of this analysis. The results should therefore be interpreted as a general proof that the method is suited to estimate the mass of the primary particle rather than as an accurate estimation of the average mass as a function of energy.

7.4 Discussion

The results show that a hybrid SD-RD detection and reconstruction is capable to measure the muon deficit in simulation as well as the mass composition of cosmic rays. Currently, the main limitation is the small area of AERA which leads to a small number of events at energies above $10^{18.6}$ eV which is required for an accurate SD reconstruction of inclined air showers with the 1500 m array. The event statistics can be increased a lot by having a reconstruction of inclined air showers using the 750 m array which will likely have a lower energy threshold. The results of this analysis have started the progress of developing such a reconstruction. In an optimistic scenario that could increase the event number for the muon deficit analysis from 58 to more than 1000 utilizing the full potential of the hybrid design of the Pierre Auger Observatory. As the overlap of SD and FD for a coincident detection of inclined air showers with the 750 m array is low the AERA reconstruction could be used for the calibration of this new reconstruction.

During the envisaged 10 years lifetime of the AugerPrime Radio Detector more than 3000 events will be measured at energies above 10^{19} eV, and approximately 300 events will exceed an energy of $10^{19.5}$ eV [59]. This expected event statistic, an order of magnitude more than hybrid FD-SD events, will significantly improve the presented measurement. As the `RdHASLDFFitter` is explicitly developed for the 1500 m array of the AugerPrime Radio Detector and has shown a good reconstruction performance on MC at the current stage of its development one can expect outstanding results with great statistics at the highest energies with the AugerPrime Radio Detector.

Both analyses can be further improved by comparing the data reconstruction with the MC true R_μ value instead of the converted R_μ originating from the reconstructed N_{19}. This yields a more accurate and independent prediction of R_μ and $R_\mu/\sqrt{S_\mathrm{rad}}$ as a function of energy. As no SD event selection has to be performed for MC anymore the high energy threshold of 10 EeV in the composition analysis could potentially be reduced. This approach requires knowledge about the total muon number with the reference hadronic interaction model QGSjetII-03 which was not available for this thesis.

8 | Conclusion

Ultra-high-energy cosmic rays can be detected by the radio signal in the MHz regime emitted by extensive air showers. All main observables, such as energy, arrival direction, and mass, can be reconstructed using the radio emission. In this thesis, a new standard reconstruction of the radio emission of inclined air showers has been developed. The emission region of inclined air showers is far away from the observer, which has an impact on the measured radio emission. Two new features have been investigated in detail: an analytical description of the signal arrival times based on a spherical wavefront model and a refractive displacement of the radio core with respect to the MC axis. The first hybrid analysis of the particles and the radio emission of an inclined air shower revealed a sensitivity on the hadronic shower development and the cosmic-ray mass. These are important prototype analyses as both are major science cases for the AugerPrime Radio Detector.

The changing refractive index in the Earth's atmosphere following its density gradient yields a displacement of the radio emission footprint on ground with respect to the MC axis. The displacement is explained by continuous refraction of the radio waves following Snell's law. It is always oriented into the incoming direction of the air shower and increases with zenith angle. For an inclination of 85° a displacement on ground of more than 1500 m is found. In the shower plane this corresponds to a displacement of 15 % of the Cherenkov radius, which illustrates the relevance of this effect for practical applications. The effect has to be taken into account when combing the results of different detection techniques in a hybrid detector such as the Pierre Auger Observatory. However, given the current experimental resolution and bias of the Surface Detector on the core position, no displacement of the radio and particle core is found in data.

The reconstruction of the arrival direction relies on an assumed wavefront model that predicts the arrival times for individual detector stations. For AERA, only a plane wavefront model has been used so far. As the emission region of inclined air showers is far away from the observer a better description is obtained with a spherical model. Applied to AERA data and simulations the spherical model results in reduced χ^2 values of about unity. The reconstructed shower axis yields a smaller opening angle with the MC axis in simulations as well as with the SD axis in data. In addition, especially the uncertainty of the reconstructed zenith angle reduces by more than a factor of two with the spherical wavefront. The improved shower direction impacts the whole event reconstruction as it is also used in the fit of the lateral distribution. The radius of the spherical wavefront yields an estimate of the distance to the shower maximum. The accuracy is found to be rather low, however, a very small radius can potentially be used to identify candidates for a neutrino-induced air shower. Lastly, the wavefront model is used to identify noise stations based on their signal arrival time. Here, the spherical wavefront improves the purity and efficiency of the selection of signal stations in the event reconstruction.

About 2000 events with zenith angles between 60° and 80° have been reconstructed from more than 6 years of AERA data. The long-standing prediction that the size of the radio footprint in the shower plane increases with the zenith angle could be verified by measured data. As the area on ground that is illuminated by the radio emission increases from $\sim$10 km^2 to more than 100 km^2 a detection of the radio emission with a sparse antenna grid is feasible. This is demonstrated by thinning out AERA to a grid with an approximate spacing of 1500 m. The reconstruction of 157 events confirms the capability of the used reconstruction methods. On average, only a minor loss in accuracy of the shower direction reconstruction with respect to the SD is found. A comparison of the reconstructed energy for 16 events shows no bias between the AERA reconstruction and the reconstruction on a 1500 m antenna grid.

The hybrid detection of particles and radio emission allows determining the muon deficit in simulations. The muonic content of the air shower R_μ as determined by the SD is described as a function of the electromagnetic energy E_EM as reconstructed by AERA. Comparing the results of 31 high-quality events with energies above $E_\text{EM} = 10^{18.72}\,\text{eV}$ to the prediction of a large set of simulations reveals a deficit of muons in simulations. The number of muons in data is in agreement with the prediction obtained for an iron primary and underpredicts the muon number in proton simulations by $\sim$35 %. For a mixed composition of protons and iron primaries that matches the mean mass number measured with the FD an increase of R_μ by 25 % is obtained. The results are in agreement with two independent analyses of the Pierre Auger Observatory performed by different combinations of detectors.

After a correction for the muon deficit the mass of the cosmic ray can be determined in a very similar way by combing R_μ and the corrected radiation energy S_rad, the energy contained in the radio emission. The ratio $R_\mu/\sqrt{S_\text{rad}}$ is used as a mass estimator. Right now, the method is limited to energies above 10 EeV resulting in only four high-quality events. The data events are enclosed by the prediction of proton and iron which bracket the lightest and heaviest possible cosmic-ray primaries. Due to the small statistics the method does not provide an accurate estimation of the average mass as a function of energy. Instead, it is demonstrated that the method in general is suited to estimate the composition.

Both analyses prove that a hybrid detection of particle and radio emission can measure the hadronic shower development and the composition of inclined air showers, paving the way for the AugerPrime Radio Detector. The current results are limited by the low statistics due to the small area of AERA. With the AugerPrime Radio Detector more than 3000 events above 10 EeV will be detected during its envisaged lifetime of 10 years, an order of magnitude more than hybrid FD-SD event. Hence, it will be able to fulfill the planned science cases and will provide outstanding results that are going to advance this field of research significantly.

A Shower Simulation Input Files

Example of a CORSIKA steering file, as used in the *RdHasLib*, for a 10^{19} eV proton primary coming from South with an inclination of 75°. Each shower has a different run number (`RUNNR`) and initial seeds (`SEED`) for the random number generator. The primary energy (`ERANGE`) and shower direction (`THETAP` and `PHIP` for zenith and azimuth angle, respectively) are set to discrete values. Air showers induced by protons (`PRMPAR` = 14) and iron primaries (`PRMPAR` = 5626) were simulated.

```
RUNNR   034600
EVTNR   1
SEED    34600 0 0
SEED    34601 0 0
SEED    34602 0 0
NSHOW   1
PRMPAR  14
ERANGE  1.000e+10 1.000e+10
THETAP  75.000000 75.000000
PHIP    0.0 0.0
ECUTS   3.0000e-01 1.0000e-02 2.5000e-04 2.5000e-04
ELMFLG  T   T
THIN    0.000005 50000.000000 5.000000e+03
THINH   1.000E+00 1.000E+02
STEPFC  1.0
OBSLEV  140000
ECTMAP  1.E5
MUADDI  T
MUMULT  T
MAXPRT  1
MAGNET  19.482300 -14.124100
PAROUT  T F
LONGI   T  5.  T  T
RADNKG  5.e5
ATMOD   27
DIRECT  ./
DATDIR  ./
DATBAS  F
USER    gottowik
EXIT
```

Corresponding CoREAS steering file setting especially the value of the refractive index at ground.

```
# CoREAS V1.4 parameter file
# parameters setting up the spatial observer configuration:
CoreCoordinateNorth = 0
CoreCoordinateWest = 0
CoreCoordinateVertical = 140000.00
# parameters setting up the temporal observer configuration:
TimeResolution = 2e-10
AutomaticTimeBoundaries = 4e-07
TimeLowerBoundary = -1
TimeUpperBoundary = 1
ResolutionReductionScale = 0
# parameters setting up the simulation functionality:
GroundLevelRefractiveIndex = 1.00031200
# event information for Offline simulations:
EventNumber = 1
RunNumber = 34600
GPSSecs = 0
GPSNanoSecs = 0
CoreEastingOffline = 0.0000
CoreNorthingOffline = 0.0000
CoreVerticalOffline = 0.0000
OfflineCoordinateSystem = Reference
RotationAngleForMagfieldDeclination = 2.087000
Comment =
CorsikaFilePath = ./
CorsikaParameterFile = RUN034600.inp
```

All input file of the *RdHasLib* are generated with a python script `generateHasLib.py` which is available in the *coreasutilities* [124]

B Saturation of Radio Stations

An AERA station will saturate if the received energy fluence is too high. Two different kinds of saturation, a saturation of the digital electronics or the analog signal chain, can occur. By design, the digital electronics saturate earlier than the analog signal chain. For too high analog signals the ADC (*analog-to-digital converter*) can not digitize the analog input signal anymore, the exact value of this data point is not converted correctly. For even higher energy fluences already the *low noise amplifier* (LNA) can enter a non-linear region which will distort the whole trace.

An example event with a reconstructed SD energy of 26 EeV and a zenith angle of 67° is shown in Fig. B.1. The energy fluence close to the shower axis is so high that all radio stations with an axis distance below 560 m are saturated. Only the tail of the lateral distribution of the radio emission can be reconstructed without saturation. As an example, the reconstructed and raw signal traces of station AERA-37 at an axis distance of 163 m are shown in Fig. B.2.

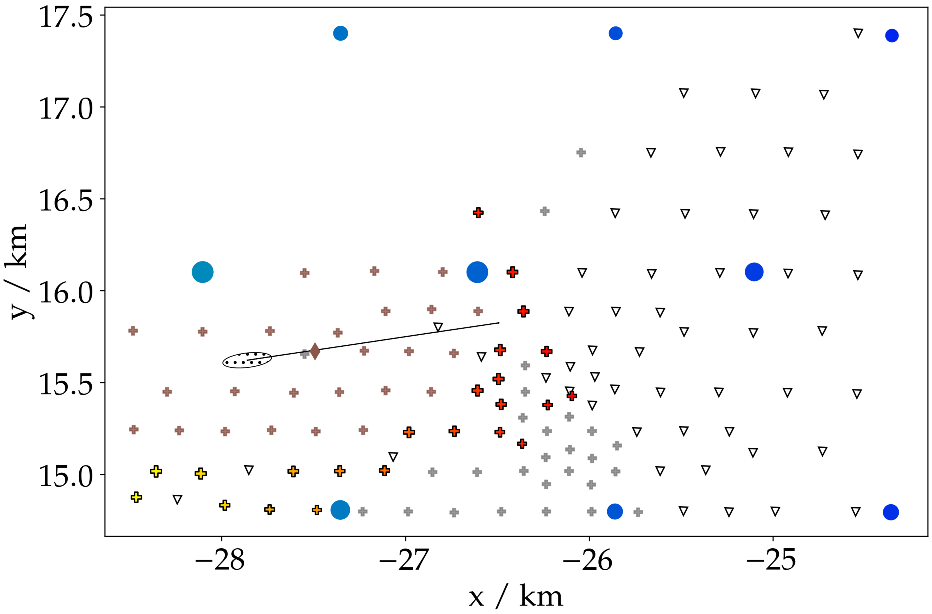

Figure B.1: Example of a saturated event with the radio ID 100936.128800 measured by AERA124. Brown markers denote saturated AERA stations, cf. Fig. 4.9 for an explanation of all symbols. The brown diamond marks the station AERA-37, which will be analyzed further.

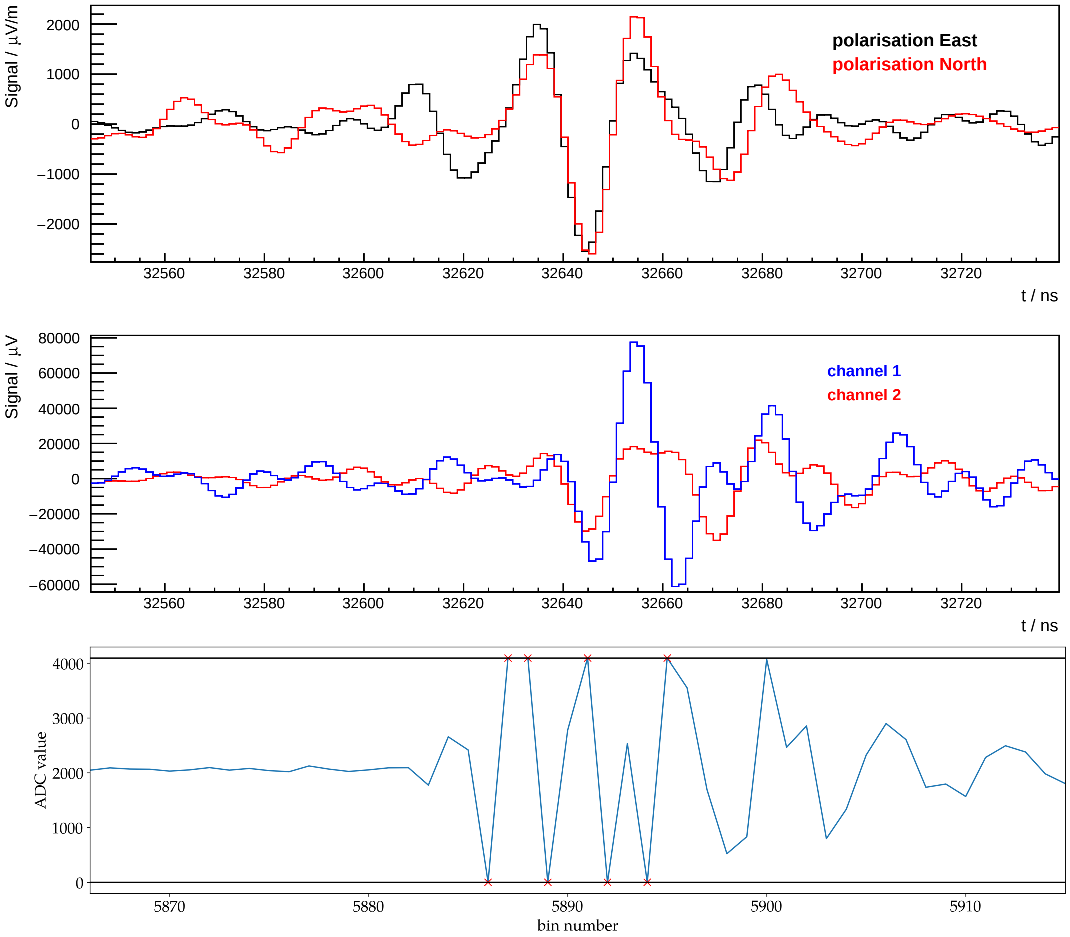

Figure B.2: Trace of the saturated station AERA-37 of the event shown in Fig. B.1. Shown are the reconstructed polarization traces (top), the measured channel traces (center) and the raw ADC trace of the saturated channel 1 (bottom). The horizontal black lines indicate the maximum allowed ADC values, red crosses highlight saturated bins. Top and center plot are extracted from the `EventBrowser`. Note that the bottom plot has a different scale on the x-axis than the other plots.

No indications of saturation are visible in the reconstructed channel and polarization traces. The unfolding of the antenna response requires multiplication in the frequency-space, cf. Eq. (4.5), which suppresses any artifact of (digital) saturation. Saturation can only be observed in the raw trace. However, $\overline{\text{Off}}\underline{\text{line}}$ correctly identifies saturated stations and sets a corresponding flag.

C | Event Selection

C.1 Used cut files for the final analysis

Example of cut files for the SD and RD event selection as used for the analysis in chapter 6 and chapter 7.

```
minZenithSD 60              # minimum zenith angle [deg]
maxZenithSD 80              # maximum zenith angle [deg]
minCandidateStations 5      # minCandidateStations 5
minRecLevel 3               # see SdRecLevel.h
T4Trigger 2                 # required T4 flag
T5Trigger 3                 # required T5 flag
minLgEnergySD 18.6          # minimum reconstructed lg(energy/[eV])

!thunderstorm 0 0           # reject TS events
maxAngleSDRD 2.08           # max opening angle in degree
hasParameter 150            # eGeomagneticRadiationEnergy
ldfSampling 1 0             # signal station inside Cherenkov ring
contained                   # SD core in convex hull of signal stations
```

C.2 FD event selection

Cut file for the FD event selection as used in [77] and summary of the event number after each cut. After the SD and RD selection 262 out of 2085 events have a reconstructed FD event. The strongest cuts are the `hybridTankTrigger` and `minViewAngle`, only 2 events are eventually selected.

```
#----------------------------------------
#  selects standard subset of Xmax events
#  from Bjarni, used in AERA Xmax analysis
#  changed wrt ICRC 2019 discussed with Michael Unger
#----------------------------------------

#==== reject laser events
!isCLF
!isXLF

#==== keep either CO/HEAT or HECO
```

```
#keepHECOorCoihuecoHEAT 18.1 { nMinusOne: 21  -10.5 10.5 }
#eyeCut 1111
eyeCut 111111

#==== hardware status
badFDPeriodRejection
#minMeanPixelRMSMergedEyes { params: 17 6 110000 nMinusOne: 100 0 100 }
#minMeanPixelRMSSimpleEyes { params: 17 11111 nMinusOne: 100 0 100 }
!badPixels                 1
good10MHzCorrection

#==== atmosphere
hasMieDatabase
maxVAOD 0.1
# relaxed version of PRD14 cut:
cloudCutXmaxPRD14 { params: 1 nMinusOne: 21 -10.5 10.5 }

#==== full hybrid geometry
hybridTankTrigger        2
maxCoreTankDist 1500
maxZenithFD              90
minLgEnergyFD            1e-20
skipSaturated
minPBrass          0.9
maxPBrassProtonIronDiff  0.05

### This was just the lower limit of the PRD 2014 analysis.
# There are also good events below that energy, especially
# (but not exclusively) with HEAT.
# minLgEnergyFD            17.8

#==== FOV cuts
# if you do not need an unbiased Xmax distribution
#FidFOVICRC13 40 20
#xMaxObsInExpectedFOV { params: 40 20 }

#==== quality cuts
xMaxInFOV       -100
minViewAngle   20
xMaxError      100.0
maxDepthHole         100.
profileChi2Sigma   { params: 3 -1.1 nMinusOne: 400 -20 20 }
depthTrackLength    200
```

```
----- FD cuts ----------------------------
                    nTot        262       -- 
                   isCLF        262     100.0
                   isXLF        262     100.0
                  eyeCut        262     100.0
    badFDPeriodRejection        262     100.0
               badPixels        256      97.7
     good10MHzCorrection        254      99.2
          hasMieDatabase        198      78.0
                 maxVAOD        193      97.5
       cloudCutXmaxPRD14        140      72.5
       hybridTankTrigger         63      45.0
         maxCoreTankDist         62      98.4
             maxZenithFD         62     100.0
           minLgEnergyFD         47      75.8
           skipSaturated         42      89.4
               minPBrass         40      95.2
  maxPBrassProtonIronDiff        40     100.0
               xMaxInFOV         38      95.0
            minViewAngle          3       7.9
               xMaxError          2      66.7
            maxDepthHole          2     100.0
        profileChi2Sigma          2     100.0
        depthTrackLength          2     100.0
------------------------------------------
```

List of Figures

List of Tables

References

[1] V. F. Hess. *Über Beobachtungen der durchdringenden Strahlung bei sieben Freiballonfahrten*. Phys. Z. 13 (1912), pp. 1084–1091.

[2] J. Clay. *Penetrating Radiation*. Proceedings of the Section of Sciences, Koninklijke Akademie van Wetenschappen Te Amsterdam 30 (1927).

[3] F. G. Schröder. *Radio detection of Cosmic-Ray Air Showers and High-Energy Neutrinos*. Prog. Part. Nucl. Phys. 93 (2017), pp. 1–68. DOI: `10.1016/j.ppnp.2016.12.002`.

[4] W. Heitler. *The Quantum Theory of Radiation: Third Edition*. Oxford University Press (1954). ISBN: 0486645584, 368ff.

[5] J. Matthews. *A Heitler model of extensive air showers*. Astropart. Phys. 22 (2005), pp. 387–397. DOI: `10.1016/j.astropartphys.2004.09.003`.

[6] J. V. Jelley et al. *Radio Pulses from Extensive Cosmic-Ray Air Showers*. Nature 205.4969 (Jan. 1965), pp. 327–328. DOI: `10.1038/205327a0`.

[7] E. M. Holt. *Combined Detection of Muons and Radio Emission of Cosmic-Ray Air Showers*. 51.03.04; LK 01. PhD thesis. Karlsruher Institut für Technologie (KIT), 2018. DOI: `10.5445/IR/1000083318`.

[8] R. Engel, D. Heck, and T. Pierog. *Extensive air showers and hadronic interactions at high energy*. Ann. Rev. Nucl. Part. Sci. 61 (2011), pp. 467–489. DOI: `10.1146/annurev.nucl.012809.104544`.

[9] A. Aab et al. *Measurement of the cosmic-ray energy spectrum above* $2.5 \cdot 10^{18}$ eV *using the Pierre Auger Observatory*. Phys. Rev. D 102 (6 Sept. 2020), p. 062005. DOI: `10.1103/PhysRevD.102.062005`.

[10] M. Aguilar et al. *First Result from the Alpha Magnetic Spectrometer on the International Space Station: Precision Measurement of the Positron Fraction in Primary Cosmic Rays of 0.5–350 GeV*. Phys. Rev. Lett. 110 (14 Apr. 2013), p. 141102. DOI: `10.1103/PhysRevLett.110.141102`.

[11] K.-H. Kampert and M. Unger. *Measurements of the cosmic ray composition with air shower experiments*. Astroparticle Physics 35.10 (May 2012), pp. 660–678. DOI: `10.1016/j.astropartphys.2012.02.004`.

[12] A. Aab et al. *The Pierre Auger Observatory Upgrade - Preliminary Design Report* (2016). arXiv: `1604.03637`.

[13] A. Yushkov on behalf of the Pierre Auger Collaboration. *Mass Composition of Cosmic Rays with Energies above $10^{17.2}$ eV from the Hybrid Data of the Pierre Auger Observatory.* In *36th International Cosmic Ray Conference (ICRC2019).* PoS(ICRC2019)482. July 2019.

[14] A. Aab et al. *Features of the Energy Spectrum of Cosmic Rays above* $2.5 \cdot 10^{18}$ eV *using the Pierre Auger Observatory.* Phys. Rev. Lett. 125 (12 Sept. 2020), p. 121106. DOI: `10.1103/PhysRevLett.125.121106`.

[15] A. Aab et al. *Combined fit of spectrum and composition data as measured by the Pierre Auger Observatory.* JCAP 2017.04 (Apr. 2017), pp. 038–038. DOI: `10.1088/1475-7516/2017/04/038`.

[16] F. D. Kahn and I. Lerche. *Radiation of cosmic ray air showers.* In *Proceedings of the Royal Society of London Series A-Mathematical and Physical Sciences.* Vol. 289. 1417. 1966. DOI: `10.1098/rspa.1966.0007`.

[17] G. A. Askaryan. *Excess negative charge of an electron-photon shower and its coherent radio emission.* Sov. Phys. JETP 14.2 (1962), pp. 441–443.

[18] D. Ardouin et al. *Geomagnetic origin of the radio emission from cosmic ray induced air showers observed by CODALEMA.* Astroparticle Physics 31.3 (Apr. 2009), pp. 192–200. DOI: `10.1016/j.astropartphys.2009.01.001`.

[19] P. Schellart et al. *Detecting cosmic rays with the LOFAR radio telescope.* Astron. & Astrophys. 560 (2013), A98. DOI: `10.1051/0004-6361/201322683`.

[20] A. Aab et al. *Probing the radio emission from air showers with polarization measurements.* Phys. Rev. D89.5, 052002 (Mar. 2014), p. 052002. DOI: `10.1103/PhysRevD.89.052002`.

[21] P. Schellart et al. *Polarized radio emission from extensive air showers measured with LOFAR.* JCAP 10 (2014), p. 014. DOI: `10.1088/1475-7516/2014/10/014`.

[22] C. Glaser et al. *Simulation of Radiation Energy Release in Air Showers.* JCAP 1609.09 (2016), p. 024. DOI: `10.1088/1475-7516/2016/09/024`.

[23] T. Huege. *Radio detection of cosmic ray air showers in the digital era.* Phys. Rept. 620 (2016), pp. 1–52. DOI: `10.1016/j.physrep.2016.02.001`.

[24] A. Bellétoile et al. *Evidence for the charge-excess contribution in air shower radio emission observed by the CODALEMA experiment.* Astropart. Phys. 69 (2015), pp. 50–60. DOI: `10.1016/j.astropartphys.2015.03.007`.

[25] L. Evans and P. Bryant. *LHC Machine.* Journal of Instrumentation 3.08 (Aug. 2008), S08001–S08001. DOI: `10.1088/1748-0221/3/08/s08001`.

[26] S. Ostapchenko. *Monte Carlo treatment of hadronic interactions in enhanced Pomeron scheme: QGSJET-II model.* Phys. Rev. D 83 (1 Jan. 2011), p. 014018. DOI: `10.1103/PhysRevD.83.014018`.

[27] T. Pierog et al. *EPOS LHC: Test of collective hadronization with data measured at the CERN Large Hadron Collider.* Phys. Rev. C 92 (3 Sept. 2015), p. 034906. DOI: `10.1103/PhysRevC.92.034906`.

[28] A. Fedynitch et al. *Hadronic interaction model sibyll 2.3c and inclusive lepton fluxes*. Phys. Rev. D100.10 (2019), p. 103018. DOI: `10.1103/PhysRevD.100.103018`.

[29] G. Battistoni et al. *The FLUKA code: description and benchmarking*. AIP Conference Proceedings 896.1 (2007), pp. 31–49. DOI: `10.1063/1.2720455`. eprint: `https://aip.scitation.org/doi/pdf/10.1063/1.2720455`.

[30] M. Bleicher et al. *Relativistic hadron-hadron collisions in the ultra-relativistic quantum molecular dynamics model*. Journal of Physics G: Nuclear and Particle Physics 25.9 (Sept. 1999), pp. 1859–1896. DOI: `10.1088/0954-3899/25/9/308`.

[31] D. Heck et al. *CORSIKA: A Monte Carlo Code to Simulate Extensive Air Showers*. FZKA Report 6019, Forschungszentrum Karlsruhe (1998). URL: `http://digbib.ubka.uni-karlsruhe.de/volltexte/fzk/6019/6019.pdf`.

[32] S. J. Sciutto. *AIRES, a system for air shower simulation and analysis*. 2002. URL: `http://www2.fisica.unlp.edu.ar/aires`.

[33] M. Kobal, The Pierre Auger Collaboration. *A thinning method using weight limitation for air-shower simulations*. Astropart. Phys. 15 (June 2001), pp. 259–273. DOI: `10.1016/S0927-6505(00)00158-4`.

[34] T. Huege, M. Ludwig, and C. W. James. *Simulating radio emission from air showers with CoREAS*. AIP Conf. Proc. 1535.1 (2013), p. 128. DOI: `10.1063/1.4807534`.

[35] C. W. James et al. *General description of electromagnetic radiation processes based on instantaneous charge acceleration in "endpoints"*. Physical Review E 84.5, 056602 (Nov. 2011), p. 056602. DOI: `10.1103/PhysRevE.84.056602`.

[36] J. Alvarez-Muñiz, W. R. Carvalho Jr., and E. Zas. *Monte Carlo simulations of radio pulses in atmospheric showers using ZHAireS*. Astroparticle Physics 35.6 (2012), pp. 325–341. ISSN: 0927-6505. DOI: `10.1016/j.astropartphys.2011.10.005`.

[37] E. Zas, F. Halzen, and T. Stanev. *Electromagnetic pulses from high-energy showers: Implications for neutrino detection*. Phys. Rev. D 45 (1 Jan. 1992), pp. 362–376. DOI: `10.1103/PhysRevD.45.362`.

[38] N. Kalmykov, A. Konstantinov, and R. Engel. *Radio Emission from Extensive Air Showers as a Method for Cosmic-Ray Detection*. Physics of Atomic Nuclei 73 (July 2010), pp. 1191–1202. DOI: `10.1134/S1063778810070136`.

[39] K. Belov. *Radio emission from Air Showers. Comparison of theoretical approaches*. AIP Conf. Proc. 1535.1 (2013), p. 157. DOI: `10.1063/1.4807540`.

[40] M. Gottowik et al. *Determination of the absolute energy scale of extensive air showers via radio emission: systematic uncertainty of underlying first-principle calculations*. Astropart. Phys. 103 (2018). DOI: `10.1016/j.astropartphys.2018.07.004`.

[41] M. Gottowik. *Systematic Studies on Radio Emission of Extensive Air Showers with CoREAS and ZHAireS Simulations.* MA thesis. Bergischen Universität Wuppertal, 2016. URL: https://astro.uni-wuppertal.de/fileadmin/physik/astro/mainpage/publications/theses/Master/Gottowik-MSc.pdf.

[42] *The Pierre Auger Cosmic Ray Observatory.* Nuclear Instruments and Methods in Physics Research Section A: Accelerators, Spectrometers, Detectors and Associated Equipment 798 (2015), pp. 172–213. ISSN: 0168-9002. DOI: https://doi.org/10.1016/j.nima.2015.06.058.

[43] I. Allekotte et al. *The surface detector system of the Pierre Auger Observatory.* Nuclear Instruments and Methods in Physics Research Section A: Accelerators, Spectrometers, Detectors and Associated Equipment 586.3 (2008), pp. 409–420. ISSN: 0168-9002. DOI: https://doi.org/10.1016/j.nima.2007.12.016.

[44] J. Abraham et al. *The fluorescence detector of the Pierre Auger Observatory.* Nuclear Instruments and Methods in Physics Research Section A: Accelerators, Spectrometers, Detectors and Associated Equipment 620.2 (2010), pp. 227–251. ISSN: 0168-9002. DOI: https://doi.org/10.1016/j.nima.2010.04.023.

[45] A. Aab et al. *Prototype muon detectors for the AMIGA component of the Pierre Auger Observatory.* Journal of Instrumentation 11.02 (Feb. 2016). DOI: 10.1088/1748-0221/11/02/p02012.

[46] C. Meurer and N. Scharf on behalf of the Pierre Auger Collaboration. *HEAT – a low energy enhancement of the Pierre Auger Observatory.* Astrophysics and Space Sciences Transactions 7.2 (2011), pp. 183–186. DOI: 10.5194/astra-7-183-2011.

[47] The AERA Group. *AERA proposal for the construction of the 20 km2 Auger Engineering Radio Array at the Southern Auger Observatory.* Internal note of the Pierre Auger Collaboration, GAP 2009-172. 2009.

[48] A. Aab et al. *The Auger Engineering Radio Array AERA.* (in preparation).

[49] D. Veberic. URL: https://web.ikp.kit.edu/darko/auger/auger-array/.

[50] T. Abu-Zayyad et al. *The surface detector array of the Telescope Array experiment.* Nuclear Instruments and Methods in Physics Research A 689 (Oct. 2012), pp. 87–97. DOI: 10.1016/j.nima.2012.05.079.

[51] E. M. Holt. *Combined Detection of Muons and Radio Emission of Cosmic-Ray Air Showers.* PhD thesis. Karlsruher Institut für Technologie (KIT), 2018. DOI: 10.5445/IR/1000083318.

[52] A. Letessier-Selvon. *The Pierre Auger Project Central Data Acquisition System.* Internal note of the Pierre Auger Collaboration, GAP 1999-003. 1999.

[53] B. Fick et al. *The Central Laser Facility at the Pierre Auger Observatory.* Journal of Instrumentation 1.11 (Nov. 2006). DOI: 10.1088/1748-0221/1/11/p11003.

[54] The Pierre Auger Collaboration. *Techniques for measuring aerosol attenuation using the Central Laser Facility at the Pierre Auger Observatory.* Journal of Instrumentation 8.04 (Apr. 2013). DOI: 10.1088/1748-0221/8/04/p04009.

[55] P. Abreu et al. *Antennas for the detection of radio emission pulses from cosmic-ray induced air showers at the Pierre Auger Observatory.* Journal of Instrumentation 7.10 (Oct. 2012). DOI: `10.1088/1748-0221/7/10/p10011`.

[56] A. M. van den Berg, D. M. Varnav, and G. Zarza. *Fiber Communication System for the Auger Engineering Radio Array at the Southern Auger Observatory.* Internal note of the Pierre Auger Collaboration, GAP 2011-035. 2011.

[57] A. Aab et al. *Calibration of the logarithmic-periodic dipole antenna (LPDA) radio stations at the Pierre Auger Observatory using an octocopter.* JINST 12.10 (2017), T10005. DOI: `10.1088/1748-0221/12/10/T10005`.

[58] A. Aab et al. *Nanosecond-level time synchronization of autonomous radio detector stations for extensive air showers.* JINST 11.01 (2016), P01018. DOI: `10.1088/1748-0221/11/01/P01018`.

[59] The Radio Group of the Pierre Auger Observatory. *The science case for the Radio Upgrade of the Pierre Auger Observatory.* Internal note of the Pierre Auger Collaboration, GAP 2020-004. 2020.

[60] B. Pont on behalf of the Pierre Auger Collaboration. *A Large Radio Detector at the Pierre Auger Observatory - Measuring the Properties of Cosmic Rays up to the Highest Energies.* In *36th International Cosmic Ray Conference (ICRC2019).* PoS(ICRC2019)395. July 2019.

[61] S. Argiro et al. *The Offline Software Framework of the Pierre Auger Observatory.* Nucl. Instrum. Meth. A580 (2007), pp. 1485–1496. DOI: `10.1016/j.nima.2007.07.010`.

[62] P. Abreu et al. *Advanced functionality for radio analysis in the Offline software framework of the Pierre Auger Observatory.* Nuclear Instruments and Methods in Physics Research Section A: Accelerators, Spectrometers, Detectors and Associated Equipment 635.1 (2011), pp. 92–102. DOI: `https://doi.org/10.1016/j.nima.2011.01.049`.

[63] O. Kambeitz. *Radio Detection of Horizontal Extensive Air Showers.* PhD thesis. Karlsruher Institut für Technologie (KIT), 2016. DOI: `10.5445/IR/1000055758`.

[64] I. Antcheva et al. *ROOT: A C++ framework for petabyte data storage, statistical analysis and visualization.* Comput. Phys. Commun. 180 (2009), pp. 2499–2512. DOI: `10.1016/j.cpc.2009.08.005`.

[65] K. Kamata and J. Nishimura. *The Lateral and the Angular Structure Functions of Electron Showers.* Progress of Theoretical Physics Supplement 6 (Feb. 1958), pp. 93–155. ISSN: 0375-9687. DOI: `10.1143/PTPS.6.93`.

[66] D. Newton, J. Knapp, and A. A. Watson. *The Optimum Distance at which to Determine the Size of a Giant Air Shower.* Astropart. Phys. 26 (2007), pp. 414–419. DOI: `10.1016/j.astropartphys.2006.08.003`.

[67] J. Hersil et al. *Observations of Extensive Air Showers near the Maximum of Their Longitudinal Development*. Phys. Rev. Lett. 6 (1 Jan. 1961), pp. 22–23. DOI: `10.1103/PhysRevLett.6.22`.

[68] A. Schulz. *Measurement of the energy spectrum and mass composition of ultra-high energy cosmic rays*. PhD thesis. Karlsruher Institut für Technologie (KIT), 2016. DOI: `10.5445/IR/1000053434`.

[69] S. Ostapchenko. *QGSJET-II: Towards reliable description of very high energy hadronic interactions*. Nucl. Phys. B Proc. Suppl. 151 (2006), pp. 143–146. DOI: `10.1016/j.nuclphysbps.2005.07.026`.

[70] A. Aab et al. *Reconstruction of Inclined Air Showers Detected with the Pierre Auger Observatory*. JCAP 1408 (2014), p. 019. DOI: `10.1088/1475-7516/2014/08/019`.

[71] A. Aab et al. *Muons in air showers at the Pierre Auger Observatory: Mean number in highly inclined events*. Phys. Rev. D91.3, 032003 (Feb. 2015), p. 032003. DOI: `10.1103/PhysRevD.91.032003`.

[72] A. Aab et al. *Depth of Maximum of Air-Shower Profiles at the Pierre Auger Observatory: Measurements at Energies above* $10^{17.8}$ *eV*. Phys. Rev. D90.12 (2014), p. 122005. DOI: `10.1103/PhysRevD.90.122005`.

[73] M. Tueros on behalf of the Pierre Auger Collaboration. *Estimate of the non-calorimetric energy of showers observed with the fluorescence and surface detectors of the Pierre Auger Observatory*. In *Proceedings, 33rd International Cosmic Ray Conference (ICRC2013): Rio de Janeiro, Brazil, July 2-9, 2013*, p. 0705.

[74] S. Acounis et al. *Results of a self-triggered prototype system for radio-detection of extensive air showers at the Pierre Auger Observatory*. Journal of Instrumentation 7.11 (Nov. 2012), P11023–P11023. ISSN: 1748-0221. DOI: `10.1088/1748-0221/7/11/p11023`.

[75] A. Aab et al. *Observation of inclined EeV air showers with the radio detector of the Pierre Auger Observatory*. JCAP 1810.10 (2018), p. 026. DOI: `10.1088/1475-7516/2018/10/026`.

[76] R. Uzeiroska. *Verbesserung des externen Triggers von AERA für ausgedehnte Luftschauer am Pierre-Auger-Observatorium*. BA Thesis. Bergischen Universität Wuppertal, 2021.

[77] B. Pont. PhD thesis (in preparation), Radboud University.

[78] A. Aab et al. *Energy Estimation of Cosmic Rays with the Engineering Radio Array of the Pierre Auger Observatory*. Phys. Rev. D93.12 (2016), p. 122005. DOI: `10.1103/PhysRevD.93.122005`.

[79] T. Huege and C. B. Welling. *Reconstruction of air-shower measurements with AERA in the presence of pulsed radio-frequency interference*. EPJ Web Conf. 216 (2019), p. 03007. DOI: `10.1051/epjconf/201921603007`.

[80] C. Welling. *Identification of radio signals from cosmic ray induced air showers with the Auger engineering radio array.* MA thesis. RWTH Aachen University, 2017. URL: `https://www.institut3a.physik.rwth-aachen.de/global/show_document.asp?id=aaaaaaaaarbkltf`.

[81] A. Corstanje et al. *The shape of the radio wavefront of extensive air showers as measured with LOFAR.* Astropart. Phys. 61 (2015), pp. 22–31. DOI: `10.1016/j.astropartphys.2014.06.001`.

[82] W. Apel et al. *The wavefront of the radio signal emitted by cosmic ray air showers.* JCAP 2014.09 (Sept. 2014), pp. 025–025. DOI: `10.1088/1475-7516/2014/09/025`.

[83] A. Aab et al. *Measurement of the Radiation Energy in the Radio Signal of Extensive Air Showers as a Universal Estimator of Cosmic-Ray Energy.* Phys. Rev. Lett. 116.24 (2016), p. 241101. DOI: `10.1103/PhysRevLett.116.241101`.

[84] A. Nelles et al. *A parameterization for the radio emission of air showers as predicted by CoREAS simulations and applied to LOFAR measurements.* Astropart. Phys. 60 (2015), pp. 13–24. DOI: `10.1016/j.astropartphys.2014.05.001`.

[85] C. Glaser et al. *An analytic description of the radio emission of air showers based on its emission mechanisms.* Astropart. Phys. 104 (2019), pp. 64–77. DOI: `10.1016/j.astropartphys.2018.08.004`.

[86] A. Aab et al. *Absolute Energy Calibration of the Pierre Auger Observatory using Radio Emission of Extensive Air Showers.* (in preparation).

[87] F. Briechle. PhD thesis (in preparation), RWTH Aachen University.

[88] T. Huege, F. Schlüter, and L. Brenk. *Symmetrizing the signal distribution of radio emission from inclined air showers.* In *36th International Cosmic Ray Conference (ICRC2019)*. PoS(ICRC2019)294. July 2019.

[89] F. Schlüter and T. Huege. *Reconstructing inclined extensive air showers from radio measurements.* (in preparation).

[90] S. Buitink et al. *Method for high precision reconstruction of air shower X_{max} using two-dimensional radio intensity profiles.* Phys. Rev. D90.8, 082003 (Oct. 2014), p. 082003. DOI: `10.1103/PhysRevD.90.082003`.

[91] T. Wiegert. *A Simulation Study on the Performance of the Auger Radio Upgrade.* MA thesis. Karlsruher Institut für Technologie (KIT), 2020. URL: `https://web.ikp.kit.edu/huege/downloads/theses/2020-Wiegert.pdf`.

[92] available on iRODS: `/pauger/Radio/Simulations/library/RdHas`.

[93] I. C. Maris et al. *Utilities for ADST-Analysis.* Internal note of the Pierre Auger Collaboration, GAP 2009-012. 2009.

[94] M. Gottowik. *Extension of the ADST event selection tool for radio.* Internal note of the Pierre Auger Collaboration, GAP 2020-033. 2020.

[95] F. Szeibert. *Radiomessung von ausgedehnten Luftschauern am Pierre Auger Observatorium - Optimierte Ereignisselektion und Hardware-Monitoring.* Diploma thesis. Bergischen Universität Wuppertal, 2013.

[96] *Analysis archiving policy for the Pierre Auger Collaboration.* 2017. URL: `https://pc.auger.unam.mx/sites/default/files/auger-analysis-archiving-policy-2017-06-02.pdf`.

[97] Wikipedia contributors. *Convex hull.* `https://en.wikipedia.org/w/index.php?title=Convex_hull&oldid=963109032`. [Online; accessed 9-July-2020].

[98] B. Pont. *AERA Data Quality Monitoring with RdMonitoring.* Internal note of the Pierre Auger Collaboration, GAP 2019-006. 2019.

[99] Wikipedia contributors. *Graham scan.* `https://en.wikipedia.org/w/index.php?title=Graham_scan&oldid=966708692`. [Online; accessed 9-July-2020].

[100] Wikipedia contributors. *Point in polygon.* `https://en.wikipedia.org/w/index.php?title=Point_in_polygon&oldid=955611839`. [Online; accessed 9-July-2020].

[101] J. Neuser. *Cosmic Rays and the Atmospheric Electric Field - Reconstruction and Data Analysis of Radio Emission from Air Showers at the Auger Engineering Radio Array.* PhD thesis. Bergische Universität Wuppertal, 2015. URL: `http://elpub.bib.uni-wuppertal.de/servlets/DocumentServlet?id=5560`.

[102] S. Nehls. *Calibrated Measurements of the Radio Emission of Cosmic Ray Air Showers.* PhD thesis. Universität Karlsruhe, 2008. URL: `http://bibliothek.fzk.de/zb/abstracts/7440.htm`.

[103] *AERAutilities.* https://gitlab.ikp.kit.edu/Radio/AERAutilities.

[104] L. Niemietz. *Lightning Detection at the Pierre-Auger-Observatory.* PhD thesis. Bergische Universität Wuppertal, 2017. URL: `http://elpub.bib.uni-wuppertal.de/servlets/DocumentServlet?id=7340`.

[105] A. Aab et al. *Impact of Atmospheric Effects on the Energy Reconstruction of Air Showers Observed by the Surface Detectors of the Pierre Auger Observatory.* JINST 12.02 (2017), P02006. DOI: `10.1088/1748-0221/12/02/P02006`.

[106] T. Huege, L. Brenk, and F. Schlüter. *A Rotationally Symmetric Lateral Distribution Function for Radio Emission from Inclined Air Showers.* EPJ Web of Conferences 216 (Jan. 2019), p. 03009. DOI: `10.1051/epjconf/201921603009`.

[107] A. Aab et al. *Improved limit to the diffuse flux of ultrahigh energy neutrinos from the Pierre Auger Observatory.* Phys. Rev. D91.9 (2015), p. 092008. DOI: `10.1103/PhysRevD.91.092008`.

[108] M. Gottowik on behalf of the Pierre Auger Collaboration. *Measurements of Inclined Air Showers with the Auger Engineering Radio Array at the Pierre Auger Observatory.* In *36th International Cosmic Ray Conference (ICRC2019).* PoS(ICRC2019)274. July 2019.

[109] L. Brenk. *Die Lateralverteilung der Radiosignale geneiger Luftschauer.* BA Thesis. Karlsruher Institut für Technologie (KIT), 2017. URL: `https://web.ikp.kit.edu/huege/downloads/theses/2017-Brenk.pdf`.

[110] F. Schlüter et al. *Refractive displacement of the radio-emission footprint of inclined air showers simulated with CoREAS*. Eur. Phys. J. C 80.7 (2020), p. 643. DOI: `10.1140/epjc/s10052-020-8216-z`.

[111] O. Scholten et al. *Measurement of the circular polarization in radio emission from extensive air showers confirms emission mechanisms*. Phys. Rev. D 94 (10 Nov. 2016), p. 103010. DOI: `10.1103/PhysRevD.94.103010`.

[112] F. Briechle. private communication.

[113] M. Erdmann, S. Fliescher, and L. Mohrmann. *Reconstruction of the Wave Front of Radio Signals at AERA*. Internal note of the Pierre Auger Collaboration, GAP 2011-092. 2011.

[114] available on iRODS: `/pauger/Papers/ICRC2019_AERA_HAS/CoREAS`.

[115] M. Gottowik. *Directional reconstruction of the radio signals with a spherical wavefront model*. Internal note of the Pierre Auger Collaboration, GAP 2020-055. 2020.

[116] available on iRODS: `/pauger/Radio/Simulations/library/RdHas_hybrid`.

[117] D. Scott. *Multivariate Density Estimation: Theory, Practice, and Visualization*. John Wiley & Sons (1992).

[118] A. Aab et al. *Direct measurement of the muonic content of extensive air showers between 2×10^{17} and 2×10^{18} eV at the Pierre Auger Observatory*. Eur. Phys. J. C 80.8 (2020), p. 751. DOI: `10.1140/epjc/s10052-020-8055-y`.

[119] E. M. Holt, F. G. Schröder, and A. Haungs. *Enhancing the cosmic-ray mass sensitivity of air-shower arrays by combining radio and muon detectors*. Eur. Phys. J. C 79.5 (2019), p. 371. DOI: `10.1140/epjc/s10052-019-6859-4`.

[120] F. Schlüter and T. Huege. *Evaluating the Potential of radio-interferometric measurements with the Auger Radio Detectors*. Internal note of the Pierre Auger Collaboration, GAP 2020-054. 2020.

[121] T. Bergmann et al. *One-dimensional Hybrid Approach to Extensive Air Shower Simulation*. Astropart. Phys. 26 (2007). DOI: `10.1016/j.astropartphys.2006.08.005`.

[122] F. Riehn. private communication.

[123] C. Glaser. *Absolute energy calibration of the Pierre Auger observatory using radio emission of extensive air showers*. PhD thesis. RWTH Aachen University, 2017. DOI: `10.18154/RWTH-2017-02960`.

[124] CoREASutilities: Collection of scripts and application for the generation of CoREAS radio simulations for AERA. `https://gitlab.ikp.kit.edu/Radio/coreasutilities`.

Eidesstattliche Erklärung

Hiermit versichere ich, die vorliegende Arbeit selbstständig und unter ausschließlicher Verwendung der angegebenen Literatur und Hilfsmittel erstellt zu haben. Die Arbeit wurde bisher in gleicher oder ähnlicher Form keiner anderen Prüfungsbehörde vorgelegt und auch nicht veröffentlicht.

Wuppertal, den: ____________________ ____________________

Unterschrift